(12)

AD A 112445

AFWAL-TR-81-4040

SPALL CRITERIA FOR SEVERAL METALS

STEPHAN J. BLESS

UNIVERSITY OF DAYTON
RESEARCH INSTITUTE
DAYTON, OHIO 45469

JUNE 1981
FINAL REPORT FOR PERIOD COVERING
FEBRUARY 1979 - DECEMBER 1980

Approved for public release; distribution unlimited.

DTIC FILE COPY

MATERIALS LABORATORY
AIR FORCE WRIGHT AERONAUTICAL LABORATORIES
AIR FORCE SYSTEMS COMMAND
WRIGHT-PATTERSON AIR FORCE BASE, OHIO 45433

DTIC
ELECTE
MAR 25 1982
S D
B

82 03 24 096

NOTICE

When Government drawings, specifications, or other data are used for any purpose other than in connection with a definitely related Government procurement operation, the United States Government thereby incurs no responsibility nor any obligation whatsoever; and the fact that the government may have formulated, furnished, or in any way supplied the said drawings, specifications, or other data, is not to be regarded by implication or otherwise as in any manner licensing the holder or any other person or corporation, or conveying any rights or permission to manufacture use, or sell any patented invention that may in any way be related thereto.

This report has been reviewed by the Office of Public Affairs (ASD/PA) and is releasable to the National Technical Information Service (NTIS). At NTIS, it will be available to the general public, including foreign nations.

This technical report has been reviewed and is approved for publication.

THEODORE NICHOLAS
Project Engineer
Metals Behavior Branch

FOR THE COMMANDER

JOHN P. HENDERSON, Chief
Metals Behavior Branch
Metals and Ceramics Division

"If your address has changed, if you wish to be removed from our mailing list, or if the addressee is no longer employed by your organization please notify AFWAL/MLLN, Wright-Patterson Air Force Base, OH 45433 to help us maintain a current mailing list".

Copies of this report should not be returned unless return is required by security considerations, contractual obligations, or notice on a specific document.

AIR FORCE/56780/11 February 1982 — 350

UNCLASSIFIED

SECURITY CLASSIFICATION OF THIS PAGE (When Data Entered)

REPORT DOCUMENTATION PAGE

READ INSTRUCTIONS BEFORE COMPLETING FORM

1. REPORT NUMBER AFWAL-TR-81-4040	2. GOVT ACCESSION NO. / 3. RECIPIENT'S CATALOG NUMBER
4. TITLE (and Subtitle) SPALL CRITERIA FOR SEVERAL METALS	5. TYPE OF REPORT & PERIOD COVERED Final Report Feb. 1979 - Dec. 1980
	6. PERFORMING ORG. REPORT NUMBER UDR-TR-81-07
7. AUTHOR(s) S. J. Bless	8. CONTRACT OR GRANT NUMBER(s) F33615-79-C-5124
9. PERFORMING ORGANIZATION NAME AND ADDRESS University of Dayton Research Institute 300 College Park Ave. Dayton, Ohio 45469	10. PROGRAM ELEMENT, PROJECT, TASK AREA & WORK UNIT NUMBERS Program Ele. 7351 06 B5
11. CONTROLLING OFFICE NAME AND ADDRESS Air Force Wright Aeronautical Laboratories Materials Laboratory (AFWAL/MLLN) Wright Patterson AFB, Dayton, Ohio 45433	12. REPORT DATE June 1981 13. NUMBER OF PAGES 114
14. MONITORING AGENCY NAME & ADDRESS (if different from Controlling Office)	15. SECURITY CLASS. (of this report) Unclassified 15a. DECLASSIFICATION DOWNGRADING SCHEDULE

16. DISTRIBUTION STATEMENT (of this Report)

Approved for public release, distribution unlimited

17. DISTRIBUTION STATEMENT (of the abstract entered in Block 20, if different from Report)

18. SUPPLEMENTARY NOTES

19. KEY WORDS (Continue on reverse side if necessary and identify by block number)

Impact damage, spall, nickel properties, aluminum properties, steel properties, tensile fracture.

20. ABSTRACT (Continue on reverse side if necessary and identify by block number)

Existing dynamic data are reviewed and new data are reported for spall type fracture in several metals. Fracture in OFHC copper was observed to be time dependent. A Tuler-Butcher description was adequate, with K_{2c} = 75 kbar^2-μs and σ_0 = -5 kbar, where $K_{2c} = \int (\sigma-\sigma_0)^2\, dt$. The plastic strain at fracture was about 0.015. Threshold fracture in 1020 steel is described by K_{2c} = 34 kbar^2-μs and σ_0 = -29 kbar. Over driven spall in 1020

DD FORM 1 JAN 73 1473 EDITION OF 1 NOV 65 IS OBSOLETE

UNCLASSIFIED

SECURITY CLASSIFICATION OF THIS PAGE (When Data Entered)

steel is better described by a c. ·independent spall stress of -45 kbar, and plastic strain of 0.03. However, experiments with conical targets indicated that this model is not entirely adequate for non 1-D strain states. Spall failure is 4340 RC30 steel did not appear to be rate dependent. The spall stress was -55 kbar. Spall is armor plate occurred at -60 kbar. In nickel 200, void formation in 1-D impacts occurred at about -20 kbar. Void coalescence was very gradual. Spall plate separation was virtually impossible in 1100 aluminum. The threshold stress for void formation was about -7 kbar.

*Stress is taken as negative in tension

PREFACE

The work reported in this document, entitled "Spall Criteria for Several Metals" was carried out for the Materials Laboratories, Air Force Wright Aeronautical Laboratories, under Contract F33615-76-C-5124. The work was supported by funds provided by the Air Force Armament Technology Laboratory (AFATL/DLJW), Eglin Air Force Base, Florida, under Project 2307E2. The contract monitor was Dr. Ted Nicholas. Technical guidance was provided by personnel at the Air Force Armament Technology Laboratory (AFATL). Specifically, the assistance of Major Dan Matuska and Capt. Raymond Bell is gratefully acknowledged. The experiments were performed at the Impact Physics Facilities of the University of Dayton Research Institute. The Principal Investigator was Dr. Stephan J. Bless. The Project Sueprvisor was George J. Roth. The Chief Range Technician was James E. Green.

Av... ...ty Codes
and/or
Dist ...cial
A

TABLE OF CONTENTS

SECTION		PAGE
I	INTRODUCTION	1
	1. IMPACT-INDUCED TENSILE FRACTURE	1
	2. CONCEPTUAL FRAMEWORK	4
	3. OBJECTIVES	9
	4. APPROACH	9
II	SPALL IN 1-D IMPACT EXPERIMENTS	13
	1. WAVE INTERACTIONS IN TARGET	13
	2. SIMPLIFIED INTERPRETATION OF FREE SURFACE VELOCITIES	16
	3. THRESHOLD CRITERIA	22
	4. VISAR DATA PRESENTATION	24
III	RESULTS FOR COPPER	26
	1. PREVIOUS WORK	26
	a. Intermediate Strain Rate Results	26
	b. Spall Data	28
	c. Other Properties of Copper	35
	2. EXPERIMENTAL DETERMINATION OF SPALL THRESHOLD	35
	3. VISAR DATA FOR COPPER	41
	4. THRESHOLD CRITERIA	41
	5. OVERDRIVEN SPALL	44
	6. STRAIN AT FAILURE	46
IV	RESULTS FOR SAE 1020 STEEL	47
	1. PREVIOUS WORK	47
	2. EXPERIMENTAL DETERMINATION OF SPALL THRESHOLD	49
	3. FREE SURFACE VELOCITY	53
	4. SWAP MODEL	53
	5. SPALL THRESHOLD CRITERIA	60
	6. OVERDRIVEN SPALL	64
	7. TWO-DIMENSIONAL TARGETS	66
	a. Fracture of Concical Targets	66
	b. Surface Velocity	66
	c. Shock Arrival Velcoity	74
	d. Code Simulation	74

TABLE OF CONTENTS (CONTINUED)

SECTION		PAGE
V	RESULTS FOR 4340 STEEL	77
	1. LITERATURE REVIEW	77
	2. DATA FOR SPALL THRESHOLD	79
	3. FREE SURFACE VELOCITY MEASUREMENTS	80
	4. SPALL CRITERIA	80
VI	FRACTURE OF ARMOR PLATE	86
	1. PREVIOUS WORK ON RHA	86
	2. SPALL THRESHOLDS FOR RHA	86
	3. VISAR DATA FOR RHA	88
	4. SPALL CRITERIA FOR RHA	88
VII	RESULTS FOR NICKEL	91
VIII	RESULTS FOR 1100 ALUMINUM	95
	1. PAST WORK	95
	2. PRESENT RESULTS	95
	APPENDIX A - EXPERIMENTAL TECHNIQUES	101
	1. LAUNCHER	101
	2. TARGET MOUNTING	101
	APPENDIX B - RELEASE WAVE SPEEDS IN FERRITE	105
	APPENDIX C - REDUCTION OF VISAR DATA	107
	REFERENCES	112

LIST OF ILLUSTRATIONS

FIGURE		PAGE
1	Examples of Fracture in Steel Targets Struck by 11 mm Diameter Balls at 3 km/s.	2
2	Examples of Spall from Present Program. Steel Targets Struck by 3 mm Flyer Plates at 300 to 400 m/s.	3
3	Examples of Spall Associated with Penetration. (a) Cross Section Through a Titanium Plate Struck at 45° by a 1.4 mm Glass Bead at 6.8 km/s. (b) Rear Surface of 25 mm Aluminum Plate Struck by a 4 mm Steel Rod.	5
4	Fracture of Steel in Terms of $\bar{\sigma}/Y$ vs ε_p. (a) Fracture Criteria. Curve is After (b) Stress Paths for Steel	8
5	Flow Chart Showing Approach for Spall Characterization of Materials.	11
6	Geometry of One-Dimensional Impact Experiments.	14
7	(x,t) Diagram for a One-Dimensional Impact.	15
8	Free Surface Velocity History Corresponding to Figure 7.	17
9	Free Surface Velocity History Modified by Spall Shock Overtake.	21
10	Free Surface Velocity History Modified by Residual Stress on Spall Plane.	21
11	Spall Threshold Criterion Predicted by Equation (24) (a) General; (b) Representation of Steel.	23
12	Representative VISAR Trace, Showing Parameter Definitions.	
13	Yielding of Half-Hard and Annealed OFHC Copper in One-Dimensional Compressive Stress.	27
14	Maximum Average Values of Strain (Squares) and Local Values of Strain (Circles) as a Function of Strain Rate for Fully Annealed ETP Copper.	31
15	Section through Target from Shot 109, Showing Void Layer.	38

LIST OF ILLUSTRATIONS (CONTINUED)

FIGURE		PAGE
16	Photomicrograph from Shot 109, Taken in Incipient Spall Plane	39
17	Photomicrograph from Shot 109, Near Separation Plane	39
18	Comparison of Copper Targets from Shots 109, 221, and 220.	40
19	VISAR Record for Copper Shot 222. Fringe Constant was 322 m/s.	42
20	Most Tensile Stress vs Flyer Plate Thickness for Spall in Copper.	42
21	Damage Parameter K_2 for Spall in Copper	45
22	Comparison of Measured and Calculated Stress Delay in Impacted 1020 Steel Targets.	48
23	Agreement to Observation of Figure 1 Obtained With Hull Code Calculation.	50
24	Sample Microstructure of 1020 Steel.	51
25	Void Structure in 1020 Steel on Incipient Spall Plane. Shot 107 300x.	54
26	Observations of Elastic Precursor Signals. Shot 14 (Closed Circles) 63 (Open Circles), and Shot 223 (Squares)	55
27	VISAR Data from Shots 24 and 63	56
28	Release Waves from Flyer Free Surface Crossing the Impact Plane in Calculation for Shot 24.	61
29	SWAP Result for Shot 24.	61
30	Comparison of SWAP Result and VISAR Data for Shot 223.	62
31	Data for Spall Threshold in 1020 Steel.	63
32	Variation of K_{2c} with σ_{min} for 1020 Steel	65
33	Preimpact Photograph of Conical Target from Shot 276.	67

LIST OF ILLUSTRATIONS (CONTINUED)

FIGURE		PAGE
34	Cross Section of Recovered Cone in Shot 273, u_o = 383 m/s.	67
35	Top View of Cone Recovered from Shot 277.	68
36	Base View of Cone Recovered from Shot 277.	68
37	Flyoff Plates in Motion from Shot 277.	69
38	Superimposition of Preimpact and Postimpact Frames from Shot 278. (Separated by 42 μs)	69
39	VISAR Record of Normal Surface Velocity from Shot 274.	72
40	VISAR Record of Shear Surface Velocity from Shot 275.	72
41	Velocity Data from Shot 274.	73
42	Density Contours 3.548 μs After Impact, from a HULL Calculation, Showing Regions Where $\rho < \rho_o$.	75
43	Variation of HEL with Sample Hardness for 4340 Steel (Various Sources).	78
44	Average Cross Sectional Area of Voids Versus Strain.	81
45	Free Surface Velocity from Shot 15.	81
46	Free Surface Velocity from Shot 17.	84
47	Free Surface Velocity from Shot 219.	84
48	Free Surface Velocity of Measured in Shot 25.	88
49	Free Surface Velocity from Shot 267.	93
50	Microstructure of Nickel, Before Impact and in Void Region.	94
51	Sample Preshot Microstructure in Aluminum.	96
52	Microstructure on Spall Plane in Shot 51.	96
53	Microstructure in Spall Plane in Shot 272.	99

LIST OF ILLUSTRATIONS (CONTINUED)

FIGURE		PAGE
54	σ_{min} as a Function of Tensile Stress Duration for Aluminum Targets.	99
55	Free Surface Velocity from Shot 272.	100
A-1	Projectile Design	102
A-2	Target Mounting Arrangement	104
C-1	Sample VISAR Data Trace	107
C-2	Two Quadrature Channels from Shot 219. (Timing Marks are 1 MHz)	111

LIST OF TABLES

TABLE		PAGE
1	SPALL THRESHOLDS FROM CHRISTMAN & ISBELL	32
2	SPALL RECOVERY DATA, FROM DAVID et al.	34
3	PROPERTIES OF OFHC COPPER	37
4	COPPER DATA SHOTS	36
5	SUMMARY OF VISAR DATA FOR COPPER	43
6	SUMMARY OF SPALL OBSERVATIONS FOR 1020 STEEL	52
7	VISAR DATA AVAILABLE FOR 1020 TARGETS	57
8	FREE SURFACE VELOCITY PARAMETERS FOR 1020 STEEL	58
9	VALUES OF YIELD PARAMETERS FOR VARIOUS SWAP MODELS	59
10	SHOTS WITH 1020 STEEL CONES	70
11	SUMMARY OF SPALL OVSERVATIONS FOR 4340 STEEL	82
12	FREE SURFACE VELOCITY PARAMETERS FOR 4340 STEEL	83
13	SPALL THRESHOLD DATA FOR RHA	87
14	FREE SURFACE VELOCITY PARAMETERS FOR RHA	89
15	SPALL THRESHOLD DATA FOR NICKEL	92
16	SPALL THRESHOLD DATA FOR 1100 ALUMINUM	97

SYMBOLS

C_b	bulk sound speed
C_L	longitudinal sound speed
J	Riemann invariant
K_s	bulk modules
K_λ	damage parameter
$K_{\lambda c}$	critical value of damage parameter
K_{Ic}	fracture toughness
M	longitudinal elastic modules
u	particle velocity
u_c	impact velocity just causing spall
U	shock velocity (in laboratory coordinates)
v	free surface velocity
V	volume
Y	deviatoric stress (second stress invariant)
Y_o	initial yield stress in uniaxial stress
Y_1	yield stress of strained material
ε	strain
ε_p	plastic strain
γ	Gruneisen constant
μ	shear modulus
ρ	density
$\bar{\sigma}$	mean stress
σ_o	critical spall threshold stress
σ_{HEL}	Hugoniot elastic limit stress
σ_{max}	Maximum compressive stress
σ_{min}	most tensile stress

SYMBOLS (CONTINUED)

σ_x	principal stress
σ_1	residual stress on spall plane
σ_s	stress at which spall occurs

SECTION I
INTRODUCTION

The response of materials to impulsive loading is a critical area of research in this country. A recent overview of this subject prepared by the National Materials Advisory Board (NMAB) has identified the limitations of materials models as the "principal limitation in the use of numerical methods that are essential in the design of many ballistic systems". ZUKAS states that "the description of dynamic material behavior, especially material failure under high loading rate, remains the greatest single obstacle to the accuracy and utility of computer codes for solid-solid impacts." The NMAB study also recognized that the characterization of fracture and dynamic plasticity are the areas most in need of investigation.

The work reported here concerns dynamic fracture in metals. The fractures occur under impact and are of a type commonly referred to as spall. In this introduction, we present the basic phenomenology and provide a theoretical framework for analysis. The experiment design is discussed in Section II. The subsequent sections present results for the individual metals investigated -- copper, mild steel, 4340 steel, armor steel, nickel, and aluminum.

1. IMPACT-INDUCED TENSILE FRACTURE

High-velocity impact events generate intense compressive shock waves that propagate away from the impact site. Wherever the shock waves encounter free surfaces, release waves are generated. Release waves communicate the free-surface zero-stress boundary condition to the shock-compressed material. Interaction of release waves results in tensile stresses that can cause fracture.

The nature of shock-induced fractures is often surprising and counter-intuitive. Some examples are shown in Figures 1 and 2.

Figure 1. Examples of Fracture in Steel Targets Struck by 11 mm Diameter Balls at 3 km/s (from BLESS and BARBER, 1979).

(a)

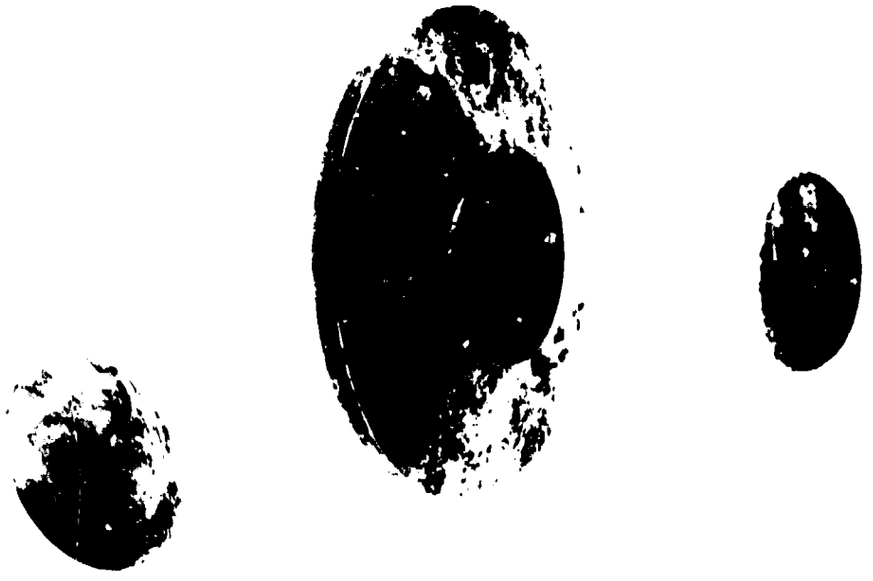

(b)

Figure 2. Examples of Spall from Present Program. Steel Targets Struck by 2 mm Flyer Plates at 300 to 400 m/s. (Spall from a flat plate (a); and spall in a cone struck on its base (b), from shot 276.)

Figure 1, taken from BLESS and BARBER, 1979, shows cross sections through mild steel targets struck by ball bearings at 3 km/s. It can be seen that the shape of the target free surface apparently had a very dramatic effect on the geometry of the fracture pattern. Radial cracks occurred in the hemisphere, but a crack parallel to the impact surface occurred in the cylinder.

Figure 2 shows examples taken from the present work. Part (a) shows fracture patterns in a cone struck by a flat flyer plate. At slightly higher velocities, the fractures coalesced, so that material separation occurred on four separate fracture systems -- two axially symmetric and two radial. Part (b) shows 1-D spall in steel; a flat flyer was launched against a flat target, resulting in a plane fracture surface.

Spall plays an important role in many processes of practical importance. Two examples from different fields are shown in Figure 3. Part (a) shows a cross section through a piece of titanium struck by a glass bead at 7 km/s. If not for the spall, penetration would have been incomplete. This particular specimen and projectile represented a model of a meteoroid impact on a spacecraft (from BLESS and GREEN, 1980). Part (b) shows a small scale model of naval ship armor. A projectile has almost penetrated the armor, and can be seen protruding through the rear surface. A spall plate has been detached that, in a full scale impact, would measure about 10 cm across. Such a plate would be quite a hazard to interior components of a ship.

2. CONCEPTUAL FRAMEWORK

Ultimate fracture in metals has been a distinct field of specialization for many years, and a great many results have accumulated. However, very little of the literature on this subject is applicable to the dynamic bulk tensile fractures associated with spall formation.

(a)

(b)

Figure 3. Examples of Spall Associated with Penetration. (a) Cross Section Through a Titanium Plate Struck at 45° by a 1.4 mm Glass Bead at 6.8 km/s (from BLESS and GREEN, 1980). (b) Rear Surface of 25 mm Aluminum Plate Struck by a 4 mm Steel Rod.

It has been established that spall fracture is influenced by (1) maximum tensile stress, (2) deviatoric stress, and (3) stress history. The only current model that takes all of those factors into account is the NAG theory. This model has been described in a series of reports from SRI International (see, for example, SEAMAN et al.). There are several disadvantages of the NAG theory that have discouraged its use in the present work. First, being micromechanical, it contains a very large number of parameters which are evaluated from relatively tedious experiments near the spall threshold. Second, since the model is "calibrated" near the spall threshold, it may be less accurate where threshold criteria are greatly exceeded (the usual case in ballistic impact.) Third, the NAG model is only incorporated into a few finite difference codes. In particular, at this time, it is not an option to the sponsors of the present program.

The approach here is based on separate time-dependent and stress-dependent criteria. Time dependence is assumed to be described by the TULER-BUTCHER criterion.

$$K_\lambda = \int (|\sigma - \sigma_0|)^\lambda dt \qquad (1)$$
$$K_\lambda \geq K_{\lambda c} \text{ for spall}$$

According to this model, there is a minimum normal stress, σ_0, at which spall can occur*. At $\sigma_{min} = \sigma_0$, the tensile stress must be applied for an infinitely long time for a spall plane to form. When $\sigma_{min} < \sigma_0$, spall takes place at shorter times. For very negative values of σ_{min}, spall takes place very rapidly, and the time dependence is less manifest.

BLESS and BARBER, 1979, discuss the fact that $\lambda = 2$ appears to be appropriate for steel. Equation (1) also has an attractive physical interpretation for $\lambda = 2$. Therefore, the value of $\lambda = 2$ has been favored for analysis of data in the work reported here.

---

*The nomenclature used here is that stress is taken as positive in compression. However, comparative terms describing tensile stresses always refer to absolute values.

In practice, it often turns out that spall can be described by a single spall stress value, σ_s. Spall occurs when σ_s is exceeded. ZUKAS (1979) and BERTOLF, et al., discuss the utility of this approximation. The success of this model may result from the fact that, in many impact situations, $\partial\sigma/\partial t$ is very high on the spall plane so target behavior is not very sensitive to the exact value of σ_s.

Most research on fracture initiation has been motivated by structural applications. Rate effects are seldom considered. The concepts that have evolved, however, can be very helpful in characterizing dynamic fracture. It is widely accepted that fracture criteria can be expressed in terms of the plastic strain, ε_p, and the ratio of mean stress to flow stress, $\bar{\sigma}/Y$, See, for example, HANCOCK, et al. Figure 4a shows a graph of failure data for steel plotted with these parameters.

The stress trajectory in $\bar{\sigma}$ and ε_p coordinates is a function of test geometry. In a conventional uniaxial stress test,

$$\bar{\sigma} = \sigma_x/3 \tag{2}$$

$$Y = \sigma_x \tag{3}$$

$$\bar{\sigma}/Y = 1/3 \tag{4}$$

For a hydrostatic stress state, $\varepsilon_p = 0$. On a uniaxial strain path, using the approximation K_s = constant, μ = constant, and Y = constant,

$$\varepsilon_x = \bar{\sigma}/M \tag{5}$$

$$\varepsilon_p = 2\varepsilon_x/3 \tag{6}$$

$$\bar{\sigma}/Y = 3K\varepsilon_p/2Y + K/2\mu \tag{7}$$

Below the elastic limit, $\sigma_{max} = \sigma_{HEL}$, and

$$\bar{\sigma}/Y = K/2\mu \tag{8}$$

Figure 4b shows graphs of $\bar{\sigma}/Y$ vs ε_p trajectories for values representative of steel. OERA is the case of uniaxial strain:

(a)

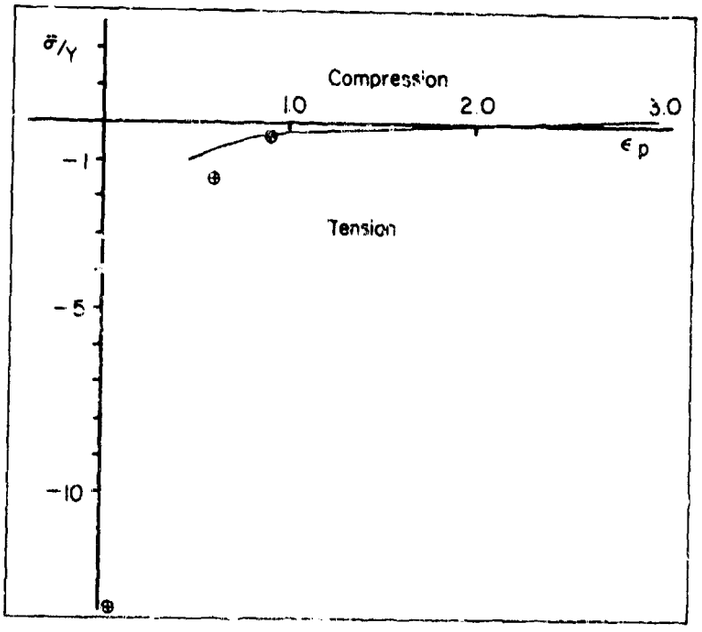

(b)

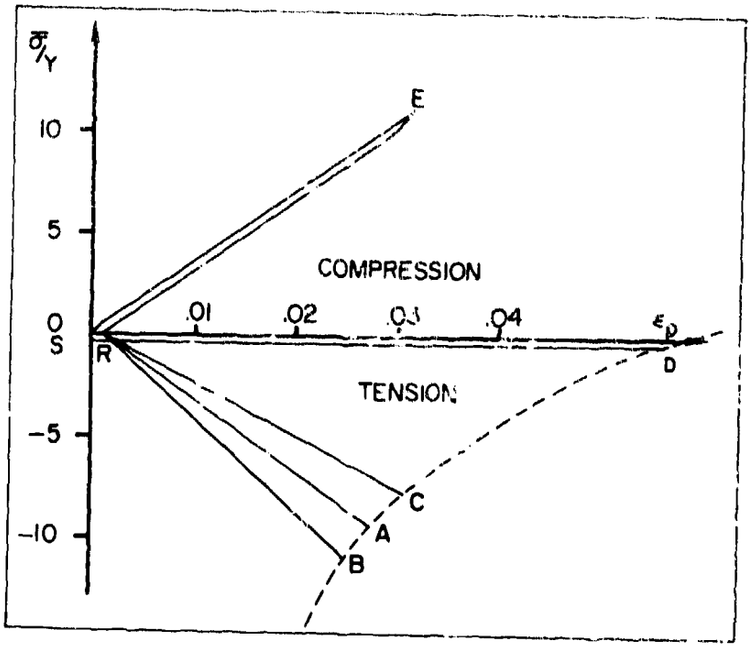

Figure 4. Fracture of Steel in Terms of $\bar{\sigma}/Y$ vs ε_p. (a) Fracture Criteria. Curve is After OSBORN, 1978. Other data are from BLESS, et al, 1979. (b) Stress Paths for Steel.

compression followed by release. RB shows a tensile path more hydrostatic than 1-D strain, namely, $\varepsilon_2 = \varepsilon_3 = 0.1\varepsilon_1$. RC is a path more compressive, namely $\varepsilon_2 = \varepsilon_3 = 0.1\varepsilon_1$. SD is the path for a uniaxial stress test. DCAB is the hypothetical fracture surface. Uniaxial strain and uniaxial stress tests give points A and D on the fracture surface, which are rather far apart (in reality, much further than shown in Figure 4b). The stress states most representative of impact events have not been well specified. It is unlikely that they will be straight lines on Figure 4. Actual impacts usually represent diverging stress waves. Hence, compression is less hydrostatic than equation (7). However, release states may be either more or less hydrostatic than RA, depending on the curvatures of the release wavefronts.

3. OBJECTIVES

The objectives of the proposed program are to quantitatively characterize spall behavior in a number of materials. The materials investigated were

- OFHC copper
- 1020 steel
- 4340 steel
- armor steel (RHA)
- nickel 200
- 1100 aluminum

4. APPROACH

The experiments performed in this program were mainly 1-D impacts. Some 2-D experiments were performed on steel targets. The principal diagnostic technique was a velocity interferometer (VISAR). This device provides a record of target free surface velocity history. The principles of VISAR operation are described by BARKER and HOLLENBACH. VISAR analysis techniques used here are described in Appendix C. Impacts were also analyzed by the SWAP method of characteristics computer code. This code was developed at Sandia Corporation and is described by BARKER and YOUNG.

The general approach employed in the program is presented in Figure 5. The steps in this approach are explained below.

1. Review all pertinent results available in the literature. Data should include spall, uniaxial tensile strength, strain rate effects, and fracture mechanics.

2. The spall threshold, u_c, is defined as the minimum impact velocity that results in partial separation of a spall plate in a 1-D test. Spall thresholds should be determined for at least two geometries, comprising differences in flyer or target thicknesses. These data will permit assessment of stress duration effects.

3. Check that there is indeed a well-defined spall threshold. In some ductile materials, considerable damage may accumulate without separation of a spall plate. In some others, only partial spall plate separation may occur. If a material is mainly considered for armor applications, probably spall plate detachment is the most relevant criterion. However, in a charge liner, extensive void formation is probably a useful criterion.

4. In the event that a spall criterion is not self-evident or if complete separation is deemed to be an inadequate measure of spall damage, an alternate approach must be developed. Usually the most useful approach is to estimate the void content of the spall plane. Void formation and growth may turn out to be a threshold phenomenon that could be used. The effect of voids on strength and elastic properties may also suggest a critical void concentration that cannot be tolerated.

5. The one-dimensional SWAP method of characteristics code must be calibrated to reproduce the observed VISAR records. The best literature estimates for constitutive properties should be used. Of particular importance are yield and release properties. If these are not available, are not adequate, or

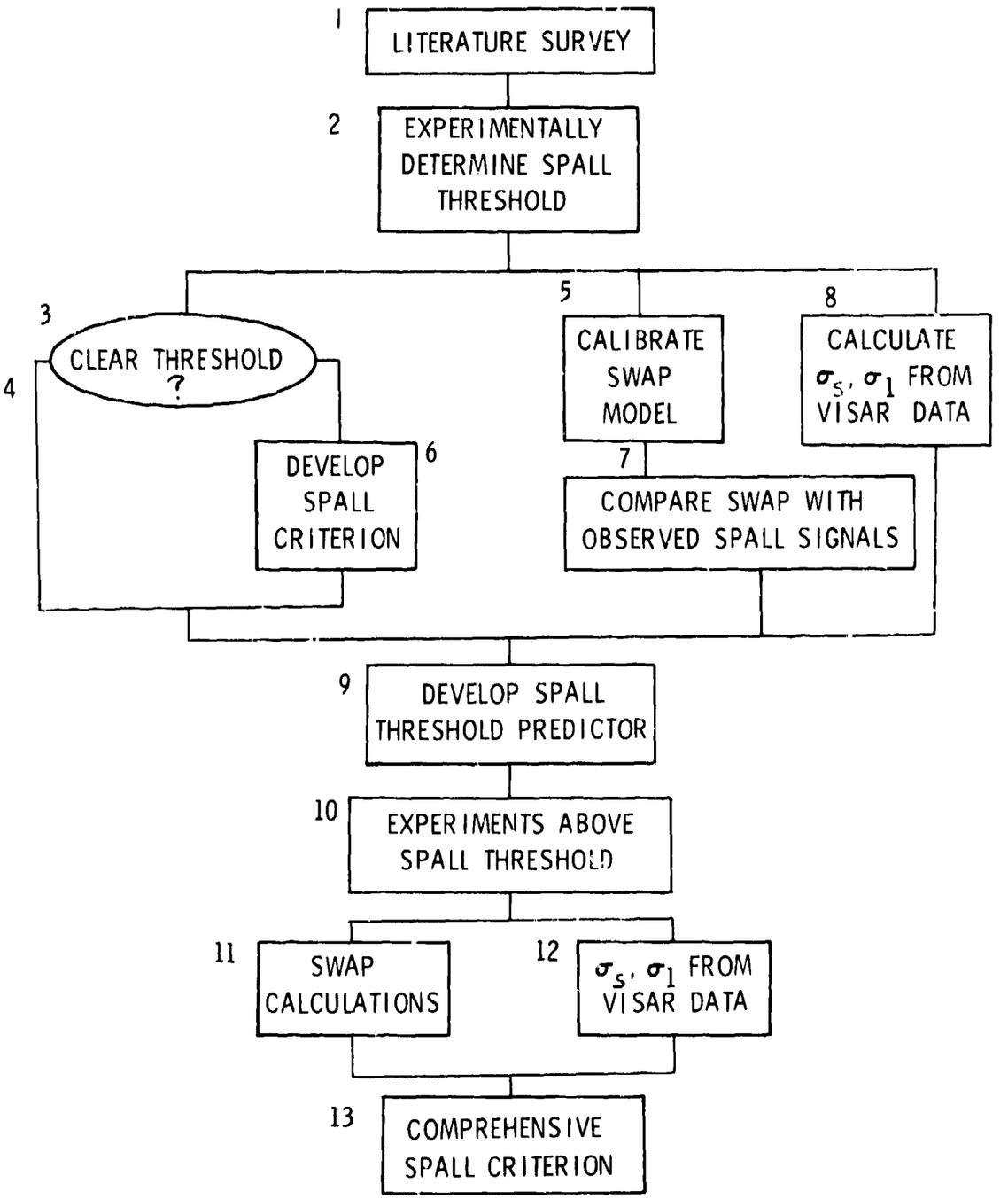

Figure 5. Flow Chart Showing Approach for Spall Characterization of Materials.

turn out to be inaccurate, VISAR data unaffected by spall can be used to develop improved constitutive properties for the undamaged material.

6. Spall should be introduced into the SWAP code in order to reproduce the observed spall plane and the observed time of arrival of the spall signal. The results for amplitude of the spall signal must be checked. If agreement is poor, then the material properties must be affected by incipient damage in a way not accounted for by the SWAP constitutive relations. This information must be incorporated in the fracture model.

7. Estimate of the spall stress, σ_s, and the residual stress on the spall plane, σ_1, directly from the VISAR free surface velocity records.

8. Develop a model describing spall threshold condition based on threshold data, VISAR analysis, and the SWAP code analysis. SWAP will allow accurate calculation of the $K_{\lambda c}$ parameter. If equation (1) is inadequate, then develop an improved version.

9. Carry out experiments well above the spall threshold. Obtain VISAR data for these impacts.

10. Carry out SWAP calculations and iterate to obtain agreement with VISAR records. Evaluate spall plane conditions leading to rupture.

11. Use VISAR records to directly obtain estimates of σ_s, σ_1, and the time required for the spall plane to coalesce.

12. Determine whether or not the over-driven spall criterion is same as the threshold condition. If not, introduce a dependence of $K_{\lambda c}$ on stress rate. Express results in terms of ε_p and $\bar{\sigma}/Y$ also.

For the case of 1020 steel, step 12 was followed by an additional process. Two-dimensional targets were impacted, as shown in Figure 2a. The complex fracture surfaces that resulted were compared with finite difference calculations.

SECTION II
SPALL IN 1-D IMPACT EXPERIMENTS

The simplest geometry for study of spall phenomena is that of "one-dimensional impact." This term refers to strain in the material under investigation:

$$\varepsilon_x = \Delta V/V \tag{9}$$

$$\varepsilon_y = \varepsilon_z = 0 \tag{10}$$

One-dimensional strain states are commonly produced by planar impact. Many discussions of planar impact loading are available (for example, ASAY and LIPKIN, or McQUEEN et al.). The techniques used in the present program are mainly described in Appendix A.

1. WAVE INTERACTIONS IN TARGET

The experimental configuration needed to produce the one-dimensional state is shown in Figure 6. A flat flyer plate impinges on a flat target with negligible tilt. Observations are confined to the region of time and space unaffected by release waves from the edges of the flyer plate.

Figure 7 is an x-t diagram showing a somewhat simplified version of the principal shocks and release waves produced by an impact. A flyer of thickness d and velocity u_o strikes a target of thickness T of like material. Impact occurs at the origin. Elastic and plastic shock waves are generated at impact. The elastic wave travels at the compressional sound velocity, C_L. The plastic shock waves propagates at the shock velocity, which is nearly equal to the bulk sound speed. All waves in Figure 7 are represented as characteristics, across which the Hugoniot equations apply:

$$\rho_2(U-u_2) = \rho_1(U-u_1) \tag{11}$$

$$\sigma_2 - \sigma_1 = \rho_1 U\ (u_2 - u) \tag{12}$$

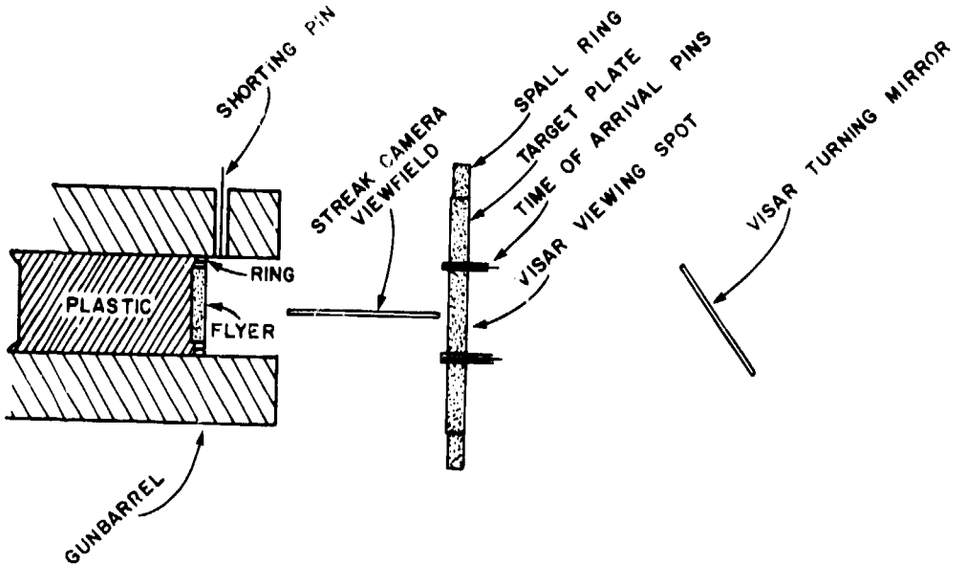

Figure 6. Geometry of One-Dimensional Impact Experiments.

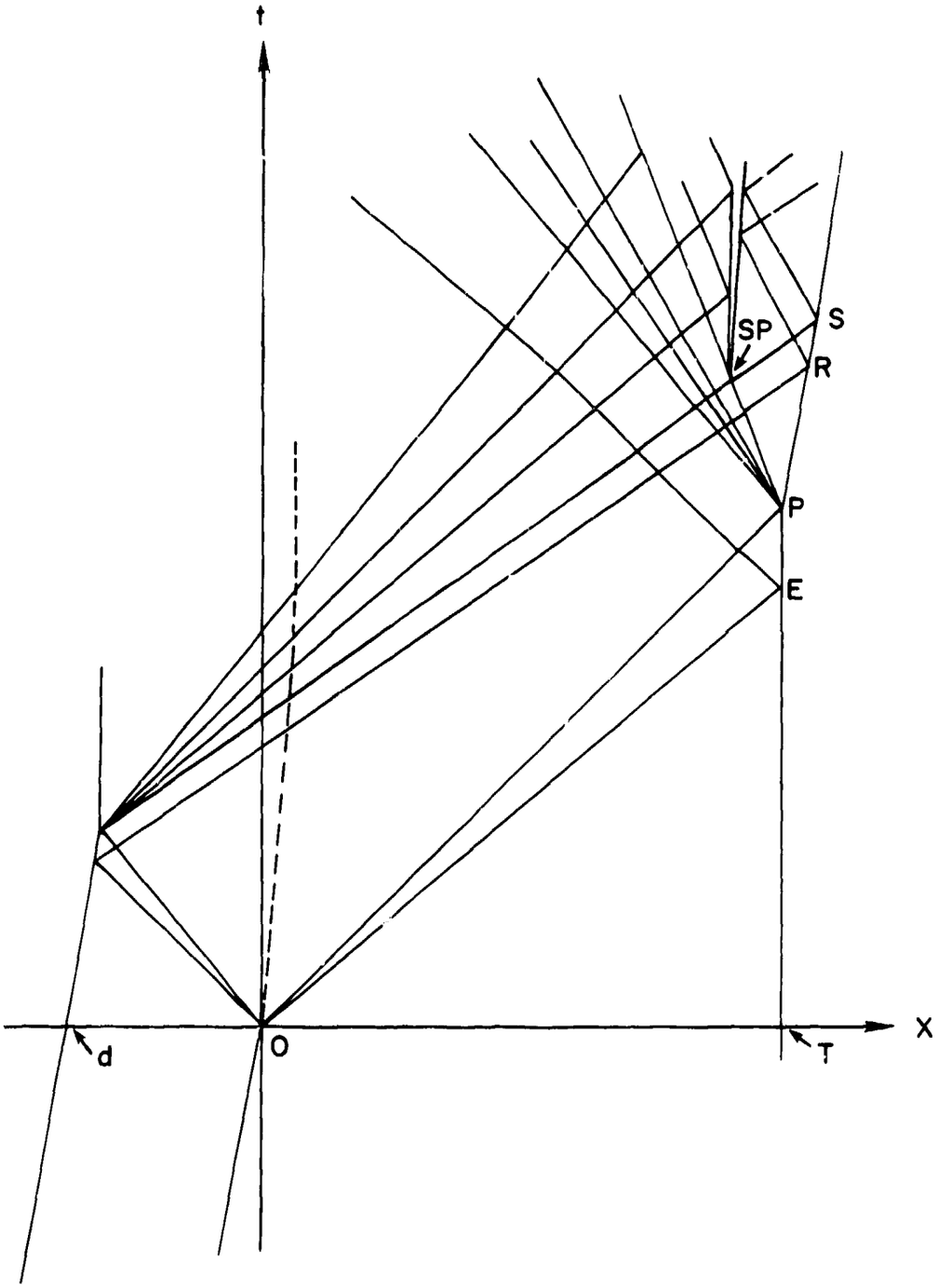

Figure 7. (x,t) Diagram for a One-Dimensional Impact.

for a wave travelling into state 1, behind which the material is in state 2.

When a wave carrying a particle velocity jump Δu impinges on a free surface, the surface is launched with a velocity increment given by:

$$\Delta v = 2\Delta u \tag{13}$$

Shock waves reflect from free surfaces as tensile waves. Such tensile waves are termed release or rarefaction waves. In this example, the release waves are also assumed to behave in an elastic-plastic way, so the first release waves propagate at an elastic wavespeed. Actual release waves are continuous because release waves are dispersive. In Figure 7, as in the SWAP code, the continuous release fan is modelled as a sequence of discreet waves. The release fan from the flyer plate traverses the target. If the target is relatively thin, it may even overtake the plastic shock wave.

The train of right-travelling waves arrives at the target free surface. E represents the elastic wave arrival, P the plastic wave arrival, R the first release arrival. To the extent that the first release wave is elastic, the time of R can be used to calculate the longitudinal elastic modulus in the shock-compressed material.

As the right-travelling and left-travelling release waves cross each other, a region of the target experiences tensile stress. If the tensile strength of the material is exceeded, someplace a spall plane develops. This is labelled SP in Figure 7.

2. SIMPLIFIED INTERPRETATION OF FREE SURFACE VELOCITIES

When the spall plane separates, the stress relaxes to zero. Hence, a shock wave is generated that raises the stress from the spall stress to zero. In general, at the instant of spall failure, release waves are propagating away from SP behind which

$\sigma = \sigma_s$. The spall shock will usually overtake a portion of these release waves. The arrival at S communicates to the free surface that the stress in the spall region was suddenly reduced to zero. However, since the shock may have overtaken several release waves on the way from SP to S, the magnitude of the shock arriving at S is somewhat less than σ_s. The spall plane presents a free surface to incoming waves; hence, later release waves reflect as shock waves, and incoming shock waves reflect as tensile waves. The free surface velocity history corresponding to Figure 7 is shown in Figure 8. Several important observations follow careful consideration of Figure 7 and other variants on the same level of complexity.

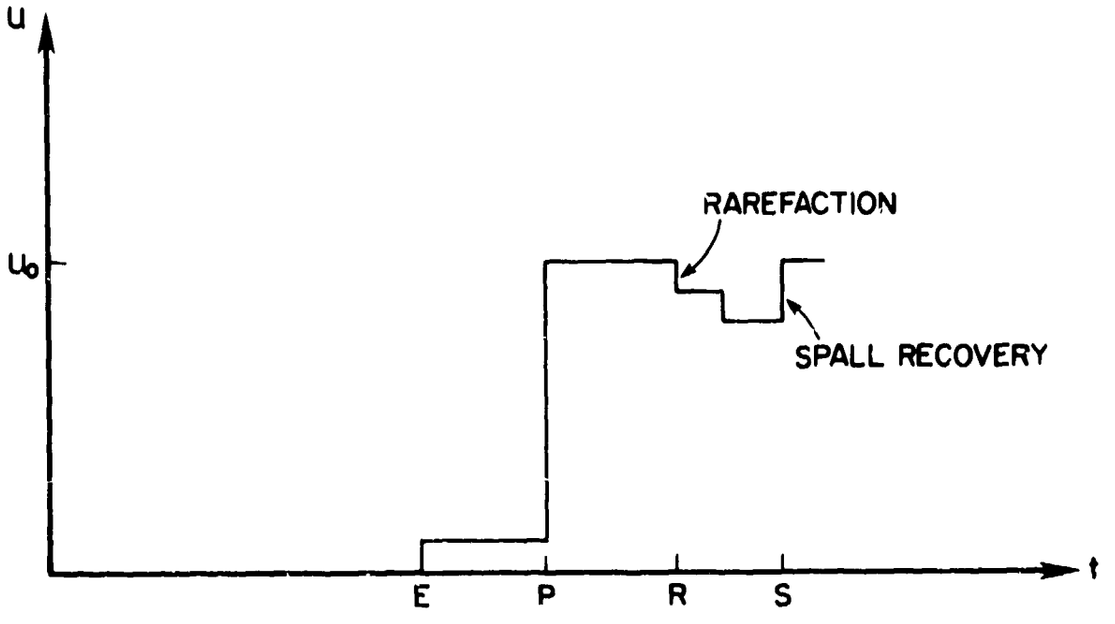

Figure 8. Free Surface Velocity History Corresponding to Figure 7.

It can be seen by inspection from Figure 7 that spall takes place first on the tail characteristic in the release fan from P. This is a consequence of the fact that the two intersecting release fans are similar; if the release fan from the flyer surface was much more compact than that from the target free surface, then spall might take place within the release fan from P. Let J_p be the Riemann invariant along the characteristic leading from P to SP.

$$J_- = u - \int_P^{SP} \frac{d\sigma}{\rho U} = J_p \tag{14}$$

Since at P,

$$u = v_p$$

$$\sigma_x = 0$$

then

$$J_p = v_p$$

Hence

$$\int_P^{SP} \frac{d\sigma}{\rho U} = u_{sp} - v_p \tag{15}$$

Where u_{sp} is the value of u just prior to separation, and σ_s is the value of stress just prior to separation. We make the assumption ρ = constant = ρ_o and $U = C_B$, hence:

$$\sigma_s = \rho_o C_B \ (u_{sp} - v_p) \tag{16}$$

The J_+ characteristic at SP, the instant before failure, is

$$J_+ = u + \int_P^{SP} \frac{d\sigma}{\rho U} = J_s \tag{17}$$

Its value may be found from the value of the free surface velocity just before the arrival of the spall plane shock, v_{min}.

$$J_s = v_{min} \tag{18}$$

Using the same assumptions as before

$$\sigma_s = \rho_o C_B \ (v_{min} - u_{sp}) \tag{19}$$

$$u_{sp} = 1/2 \ (v_p + v_{min}) \tag{20}$$

Finally,

$$\sigma_s = 1/2\rho_o C_B \ (v_p - v_{min}) = 1/2\rho_o C_B \Delta v_s \tag{21}$$

A derivation somewhat similar to the present was given by DAVID et al. Equation (21) was used by CHRISTMAN and ISBELL to deduce spall stress values from their data. According to them, it was first proposed as an empirical formula by TAYLOR. In many impacts, $\rho_o C_B$ may vary by as much as 10% between the target free surface and spall plane. Therefore, at worst, equation (21) should be accurate to about ± 5%.

There are at least three second-order effects that modify the above portrayal. The first is associated with reflections from discontinuities. Wherever two characteristics cross each other, a discontinuity results across which there is a density contrast. Later characteristics incident on the discontinuity may split or reflect. For example, when the elastic release wave crosses the plastic shock near the flyer free surface or target free surface, a discontinuity of 0.01 g/cm^3 is created in iron. When a rarefaction wave train crosses this continuity, about one percent of it is reflected. The region between the spall plane and the free surface is rich in such discontinuities. Detailed SWAP calculations show that the characteristics traversing this space are dispersed and attenuated. The consequence for equation (21) is that spall stress will be underpredicted by a few percent.

The second source of errors in equation (21) is overtaking of the SP-S rarefaction by the separation shock. Figure 9 shows the effect on free surface motion; the solid line illustrates the observed free surface velocity history, and the dotted line shows the history, that would have occurred if not for the overtaking.

The decrement in free surface velocity, v' is lost, and cannot be deduced from the experimental record. Consequently, equation (21) will underestimate σ_s. The extent to which spall information is lost depends on d, and whether or not the spall shock travels at an elastic or plastic wavespeed. All right-travelling release waves arriving at the spall plane for a time Δ_{st} before spall occurs are "lost". For $T > \sim 2d$, Δ_{st} is very nearly

$$\Delta_{st} = \frac{d}{U_s} - \frac{d}{U_R} \tag{22}$$

where U_s is the shock velocity from SP, and U_R is the typical release velocity. It has also been assumed that SP is a distance d from the target free surface, and the effects of changes in particle velocity have been neglected. For steel, $\Delta_{st} \simeq 0.1$ μs for d = 2mm and 0.05 μs for d = 1 mm, if U_s is an elastic wavespeed. This leads to a substantial value of v'. If U_s is plastic, then for steel $\Delta t_s \simeq 0.016$ μs for d = 2mm, and $\Delta t_s \simeq 0.008$ μs for d = 1 mm. SWAP calculations permit an estimate of the magnitude of these corrections. For copper and other targets for which the elastic strength is relatively small, the corrections needed for this effect are not important.

The third possibility is that the spall plane continues to support a stress σ_1 after fracture. The resulting free surface history is shown in Figure 10. The spall signal fails to rebound to the peak free surface velocity, missing it by an amount Δv_f. Equation (21) is still valid for σ_s, the stress at which the fracture initiates. The spall plane strength σ_1 is given by

$$\sigma_1 = 1/2\ \rho_o C_B\ \Delta v_f \tag{23}$$

If σ_1 varies with time, then no simple interpretation of the velocity, record is possible. Most spall records, at least near the threshold, look like Figure 10.

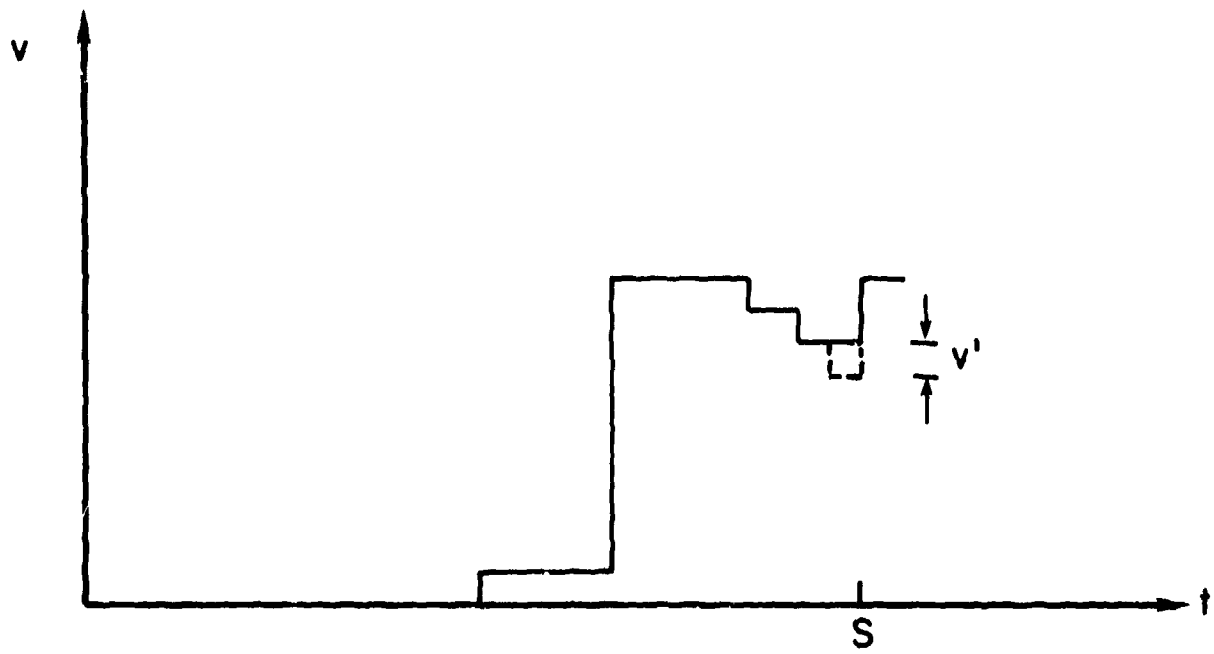

Figure 9. Free Surface Velocity History Modified by Spall Shock Overtake.

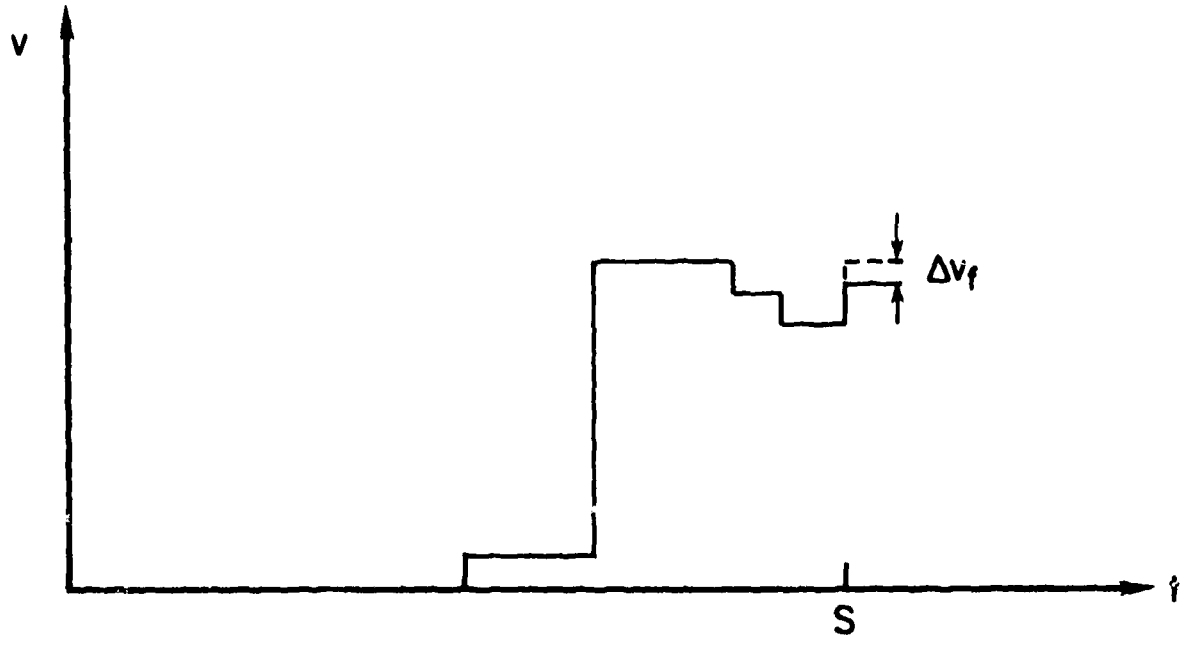

Figure 10. Free Surface Velocity History Modified by Residual Stress on Spall Plane.

3. THRESHOLD CRITERIA

The data obtained in this program were analyzed with both time-dependent and time-independent formulations. The Tuler-Butcher relationship was used for the time-dependent approach (TULER and BUTCHER). The mean stress-plastic strain approach embedded in Figure 4 was used for the time-independent approach.

As discussed in Section 1, the form of the Tuler-Butcher equation to be chiefly employed is

$$K_2 = \int (\sigma - \sigma_o)^2 \, dt \qquad (24)$$
$$K_2 \geq K_{2c} \text{ for spall}$$

In equation (24), σ_o is the critical stress for spall formation, and K is a damage parameter. Spall cannot occur if the tensile stress does not exceed σ_o. The tensile loading on the incipient spall plane is approximately a pulse of amplitude $-\sigma_{max}$ and duration $2d/C_B$ (where no spall occurs). It follows that the threshold conditions for formation of a spall plate are approximately as shown in Figure 11a.

Some numerical insight into the consequences of equation (24) can be obtained by substituting:

$$\sigma = 1/2 \, \rho_o \, u_o \, (C_B + Su_o) \qquad (25)$$
$$\sigma = 1/2 \, \rho_o \, C_B \, u_c$$

which gives:

$$u_o(1 + 1/2 \, Su_o) = \frac{2K}{\rho_0^2 \, dC_B} + u_c \qquad (26)$$

Equation (26) is graphed in Figure 11b for values representative of steels, namely $\rho_o = 7.85$ g/cm^3, $C_B = 4.67$ mm/μs, $S = 1.33$, $u_c = 0.2$ mm/μs, and $K = 337$ kbar^2- μs. It can be seen from Figure 11b that the range of flyer plate thickness over which the spall criterion depends on thickness is rather small, $d \lesssim 1$ mm. The

(a)

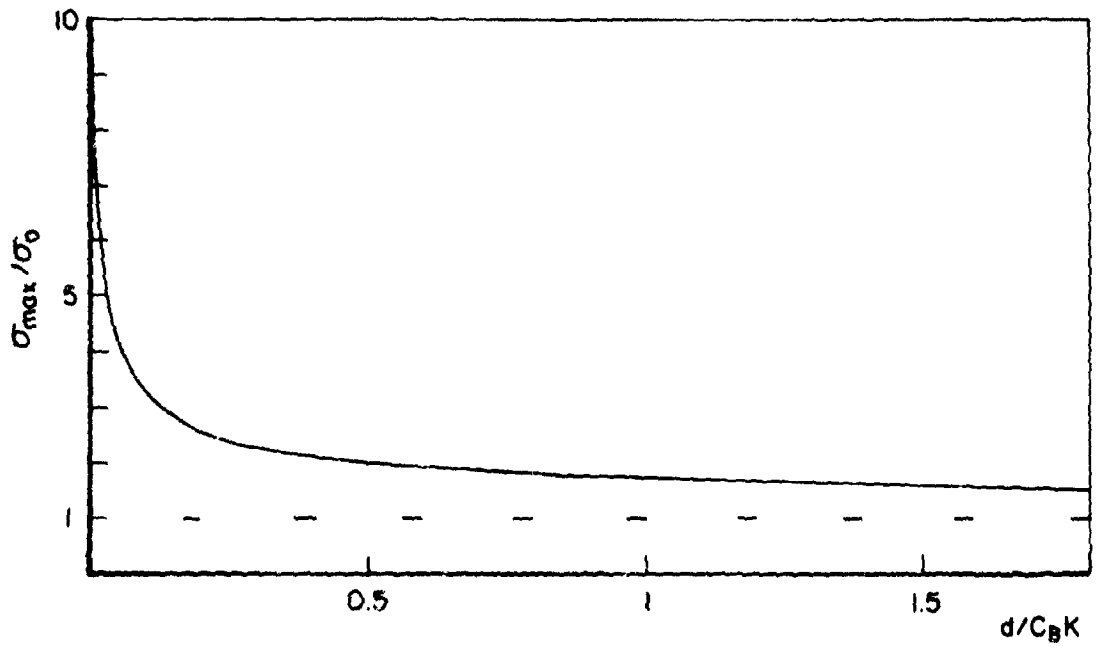

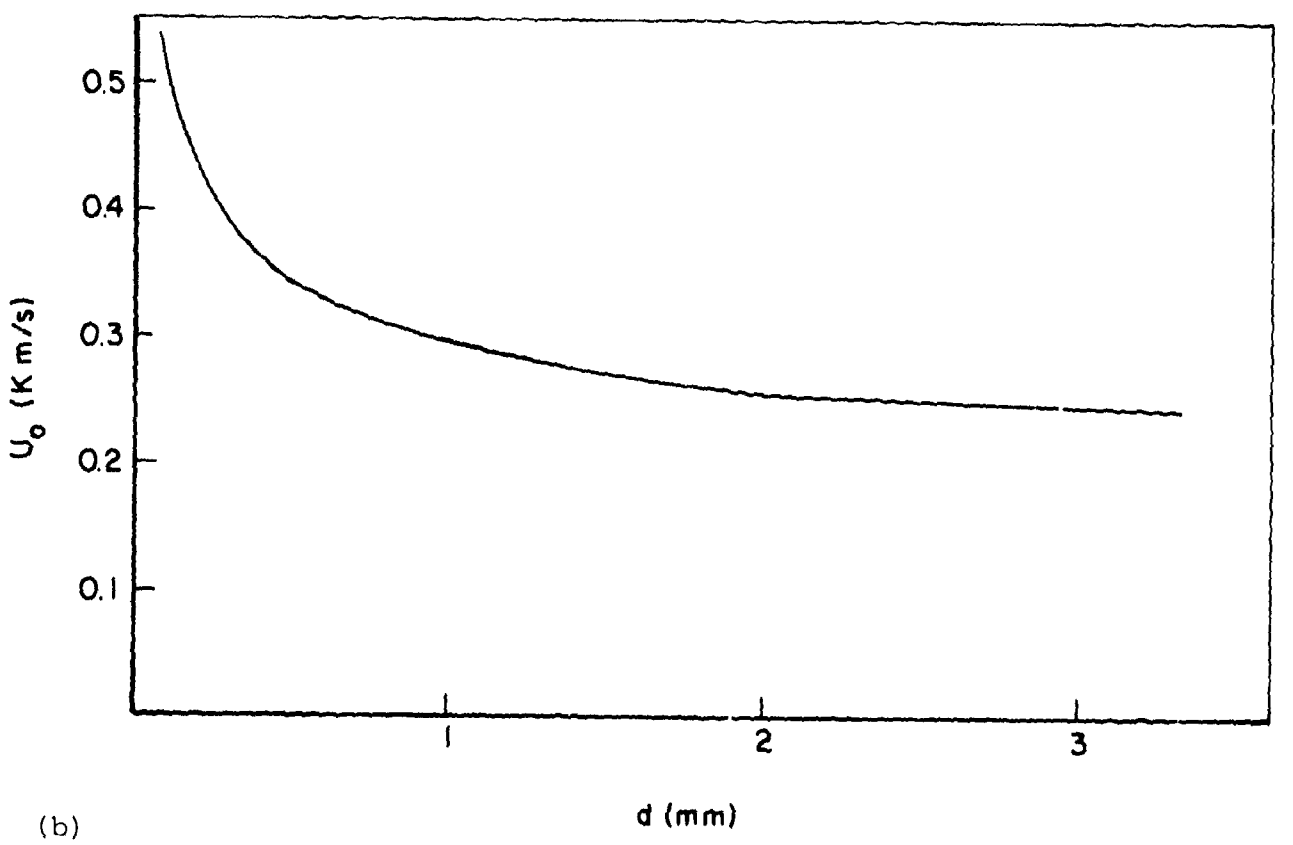

(b)

Figure 11. Spall Threshold Criterion Predicted by Equation (24) (a) General; (b) Representation of Steel.

transition from d-dependence to u_o-dependence depends on $K^{-1/2}$. It is necessary to use impractically large values of d to observe spall at $u = u_c$ directly. Actual points on the curve of Figure 11 can be used to calculate σ_o and $K_{\lambda c}$. For such a threshold shot, does $K_{\lambda c}$ depend on σ_{min}? The answer can be obtained by using SWAP to calculate K_λ for shots in which $\sigma_{min} \ll \sigma_o$. If it is found that $K_\lambda = K_{\lambda c}$ here too, then the answer is yes. Otherwise, a complete spall criterion would need to express $K_{\lambda c}$ as a function of σ_{max}. The dependence of $K_{\lambda c}$ on σ_{max} can have two origins. Shock-induced fractures may affect $K_{\lambda c}$. Or, spall may be associated with a critical time scale, so that σ can drop far below σ_o for a while before spall occurs. This latter point of view is more consistent with recent developments in fracture mechanics.

4. VISAR DATA PRESENTATION

Free surface velocities were measured with a VISAR. The analysis of VISAR data is discussed in Appendix C. Each VISAR record yields a curve showing how v varies with time. Uncertainties in VISAR data vary from shot to shot, and point to point. Time of arrival data are almost always very precise. Likewise, relative velocities are usually rather well determined. However, a variety of effects conspire to introduce uncertainties in absolute velocity measurements, as discussed in Appendix C.

In order to express uncertainties, VISAR results are often presented in tabular form in this report. Figure 12 shows a velocity record with most features that are observed. (Not every shot or every material displays all of these features.) The parameters used to describe the VISAR data are defined in Figure 12.

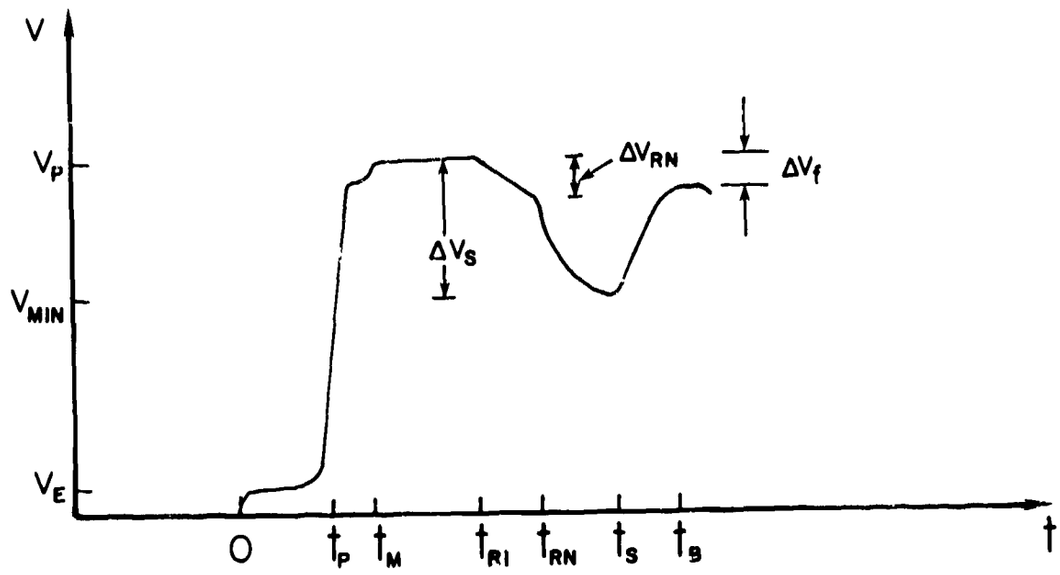

Figure 12. Representative VISAR Trace, Showing Parameter Definitions.

SECTION III
RESULTS FOR COPPER

The results of the investigation of spall in copper are organized according to the flow chart of Figure 5.

1. PREVIOUS WORK

Several data for tensile yielding and fracture of copper can be found in the literature. In addition, many authors have tried to use ductile fracture in copper as a paradigm for fracture of ductile metals in general. In spite of these previous efforts, a general fracture criterion for copper for use in HULL-type finite difference codes does not seem to be available.

It is well known that copper is a rate sensitive material, and there is evidence that the phenomena responsible for yielding and fracture change at strain rates below about 100 s^{-1} (CHRISTMAN and ISBELL, 1971; BAUER and BLESS, 1978). Therefore, this review will be mainly limited to high strain rate data.

a. Intermediate Strain Rate Results

CHRISTMAN and ISBELL (1971) performed split Hopkinson bar tests on annealed (RF35) and half-hard (RF78) OFHC copper. The results of uniaxial stress tests are shown in Figure 13. Relative to the annealed material, the half-hard material was extremely rate sensitive, but did not work harden.

Depending on hardness, initial yield stress Y_0, varied from 0.3 to 3.3 kbar. The annealed material could be described by work hardening exponents, defined in the equation:

$$Y_1 = Y_0 \left(\frac{\varepsilon}{\varepsilon_Y} \right)^N \qquad (27)$$

where N = 0.27. For half-hard copper, there was almost no work-hardening, N = 0.031. The exponential work hardening relation does not fit low strain rate data (PERRA, 1976).

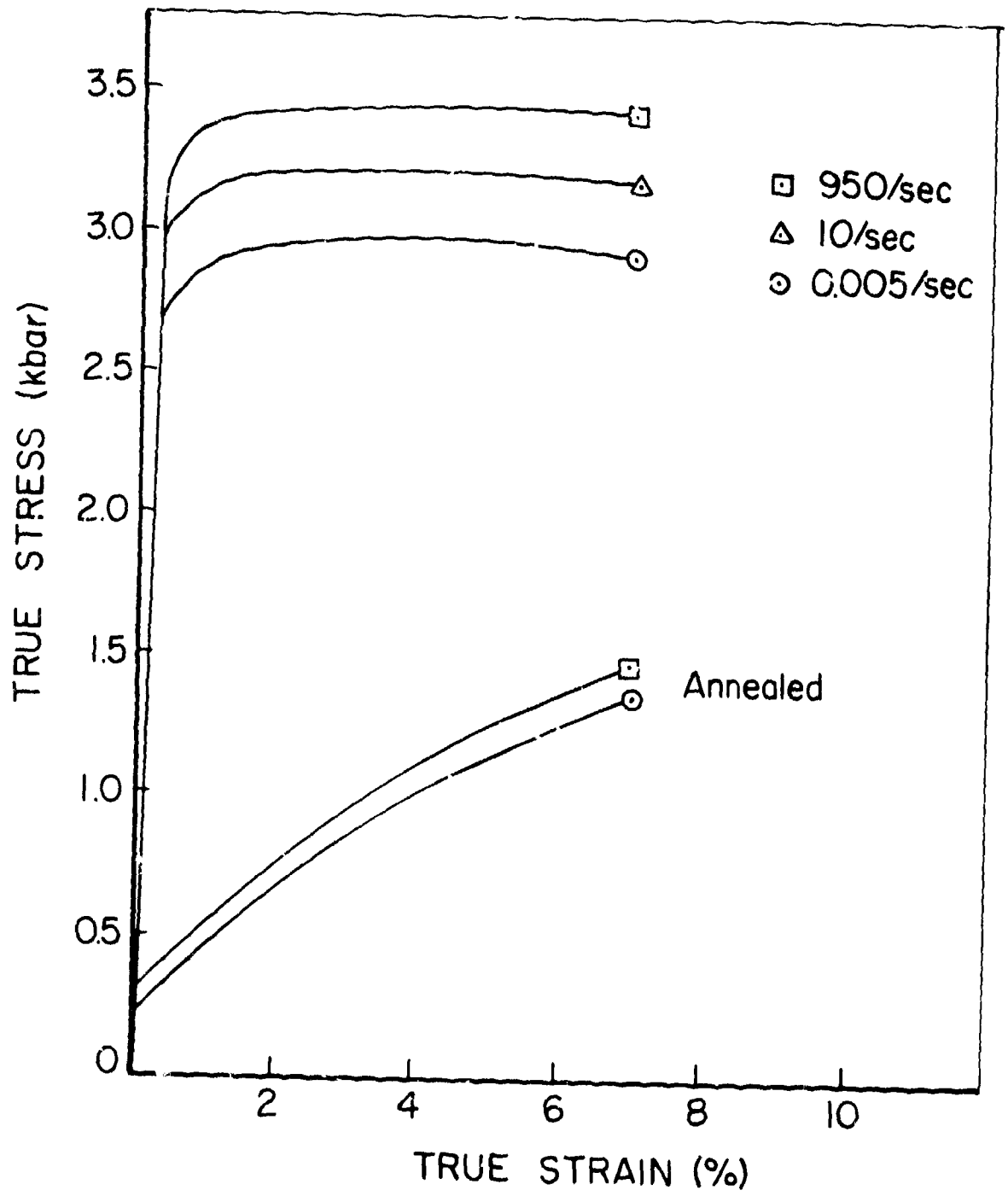

Figure 13. Yielding of Half-Hard and Annealed OFHC Copper in One-Dimensional Compressive Stress, from CHRISTMAN and ISBELL.

CHRISTMAN and ISBELL also investigated the extent of the Bauschinger effect in copper by performing compressive-tensile cyclic loading to yield at low strain rates. They found the effect was not significant. However, MCMILLAN et al., 1971, found it necessary to invoke the Bauschinger effect to explain shock release data.

SHULTZ (1969) determined the high strain rate yield behavior of OFHC copper using a wire-impact technique. His copper had a static yield strength of 2.50 kbar, comparable to the half-hard copper tested by CHRISTMAN and ISBELL. At $10^3 s^{-1}$, this material had a yield strength of 3.16 kbar, which is consistent with CHRISTMAN and ISBELL'S data.

Rapid tensile failure in a uniaxial stress state must be accomplished by expanding rings or cylinders. These have been studied by BAUER and BLESS (1979) and by RAJENDRAN and FYFE (1980). Both sets of investigators found dramatic increases in strain to failure due to suppression of local instabilities at higher strain rates. This increase in average strain to failure was especially large in the interval $10^3 - 10^4\ s^{-1}$. According to BAUER and BLESS, ultimate strain (true strain) at failure actually decreased from a static value of 1.6 to value of 1.0 at $\dot{\varepsilon} \sim 10^3\ s^{-1}$. That is, when the strain in the failed region alone is considered, it becomes clear that the material is less ductile at high rates, as shown in Figure 14.

b. Spall Data

There have been three principal experimental investigations of spall in copper: by SRI, summarized in SEAMAN et al. 1972; by General Motors, summarized by CHRISTMAN and ISBELL, 1971; and by CEA, reported by DAVID et al. 1973.

SEAMAN et al., modelled copper with the SRI NAG theory. Parameters in the theory were evaluated by impacts below the spall separation threshold. Wedge shaped flyers were sometimes used, in which the duration of the tensile pulse varies across the sample. The material studied was fully annealed OFHC copper.

Eight impacts were carried out at velocities up to 129 m/s, which was below the separation threshold. The void concentration on the incipient spall planes were determined by counting on sectioned targets. Several parameters in the NAG theory could not be directly measured. The initial radius of voids was taken as 10^{-4} cm. The viscosity of copper η was taken as 750 p. The constants $\dot{n}$ and P_1 in the growth equation

$$\dot{N} = \dot{n}_0 \exp \frac{p-p_0}{p_1} \tag{28}$$

were $\dot{n}_0 = 2.8 \times 10^{12}$ $cm^{-3}s^{-1}$ and $p_1 = -2$ kbar. Then the nucleation threshold turned out to be -5 kbar.

In relating p_0 to a threshold velocity, the yield behavior of the copper must be taken into account. The peak tensile stress in planar impacts is about equal to the peak compressive stress. For a given strain, the peak stress in one-dimensional strain exceeds the mean stress by 2/3 Y. If p_0 = 5 kbar, and Y $\sim$ 3 kbar, then $\sigma_{max} \sim 7$ kbar, which means that spall damage will start to accumulate at velocities as low as $\sim$ 25 m/s.

The growth parameter, p_{go}, defined in:

$$\dot{R} = \frac{p-p_{go}}{4\eta} R \tag{29}$$

where R is void radius), was also recommended as 5 Kbar for copper. A useful equation for checking the NAG formulation is the prediction of maximum void size produced by a square tensile pulse of duration Δt, which is:

$$\frac{R_{max}}{R_0} = \exp\left(\frac{p-p_{go}}{4\eta}\right)\Delta t \tag{30}$$

In the SEAMAN et al., study, the NAG parameters were used in a finite difference code especially modified to account for the influence of void growth on mechanical properties. Naturally, this formulation had to account in an average way for the plastic flow and plastic instabilities (see PERRA, 1978) that occur around

voids. The agreement with predicted void concentrations was rather good, but void content was underpredicted at high damage levels. This indicates that the void growth assumption employed becomes invalid as voids become large and start to interact with each other. SEAMAN et al. did not present an explicit discussion of uniqueness or sensitivity for their parameters, although they did discuss several test calculations which also yielded reasonably good correlation with experiments. In these, the values p_0 = 6.5 kbar and η = 3570 p gave good agreement.

Both SEAMAN et al., and MOSS, (1977), discuss techniques for predicting NAG parameters. The viscosity parameter that determines void growth can be determined independently. WALTERS, (1979), recently reviewed viscosity data and reports a value of 3000 p for copper at 93 kbar. SEAMAN et al. cite literature values of 1150 to 3600 p. None of these is in very good agreement with the value of 750 p needed to reproduce the observed void pattern with equation (29) or (30). Similarly, σ_{go} should be related to the yield stress and fracture toughness. MOSS derives:

$$\sigma_{go} = \frac{\pi}{4R_o} K_{1C} \tag{31}$$

However, apparently there are not data for K_{1C} appropriate for shock-damaged copper, which limits the usefulness of equation (31).

More useful is the identification of σ_{go} with plastic yielding in the vicinity of voids. CHRISTMAN and ISBELL give a value for the HEL of 8 kbar (see below). SEAMAN et al. identified void growth with the HEL (p.57), leading to a prediction of $p_0 = \sigma_{HEL} - 2Y/3$ which agrees with the value of p_0 that gave gave good results in calculations. (It is not clear in their discussion if the value of p_0 was in fact set equal to $\sigma_{HEL} - 2Y/3$ and not varied).

CHRISTMAN and ISBELL determined experimental values of spall threshold velocities for half-hard OFHC copper. They defined spall threshold as the point at which cracking occurred over 50 percent of the spall plane. Their data are give in Table 1. Stress wave profiles were measured with a VISAR or other techniques.

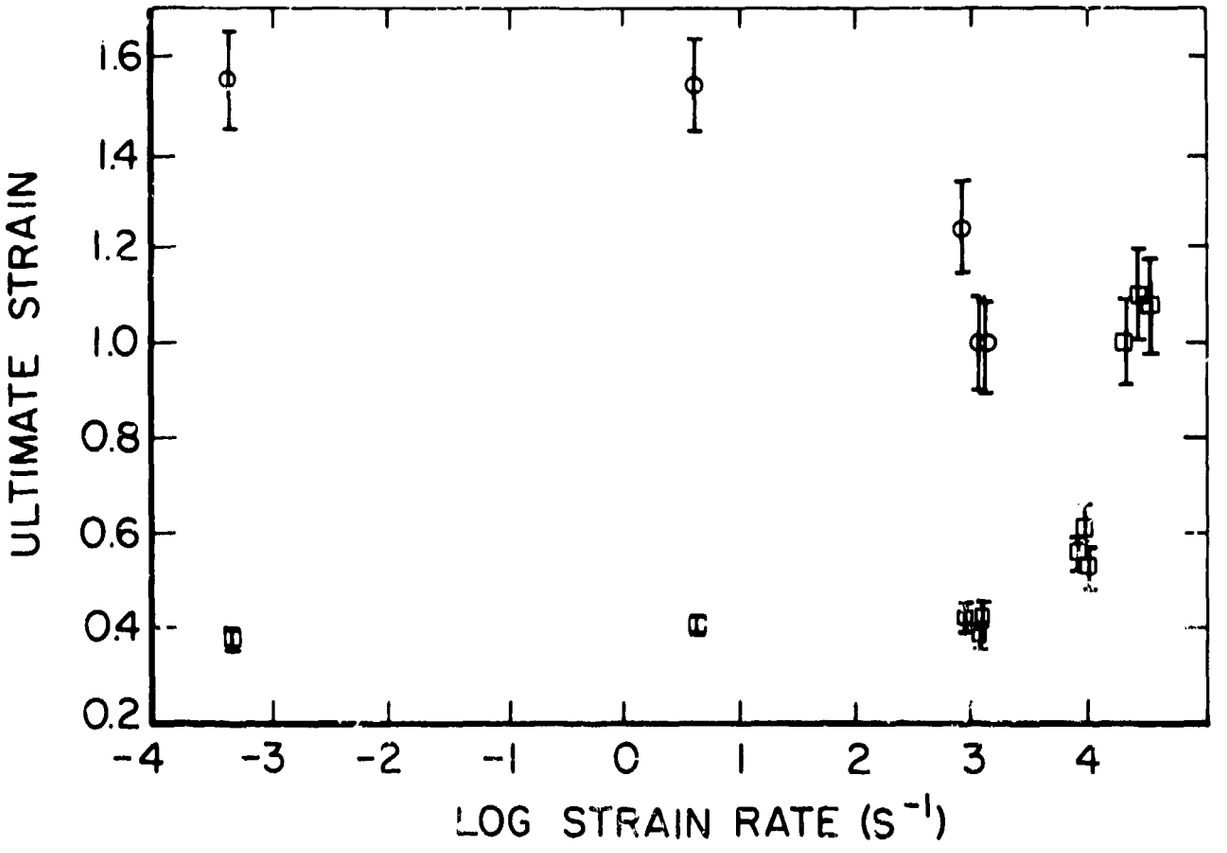

Figure 14. Maximum Average Values of Strain (Squares) and Local Values of Strain (Circles) as a Function of Strain Rate for Fully Annealed ETP Copper. From BAUER and BLESS.

TABLE 1

SPALL THRESHOLDS FROM CHRISTMAN & ISBELL

Flyer Thickness (mm)	Target Thickness (mm)	Threshold Velocity (m/s)
0.49	1.01	135
1.49	3.04	110
3.04	6.07	95
0.40	3.85	180

They used the equation (21) to calculate the spall stress. The result depended on flyer thickness, being σ_s = -21 kbar for 1-mm flyers and -35 kbar for thinner flyers.

DAVID et al., also studied spall in OFHC copper of 0.01 mm grain diameter. In distinction to the other studies, they used impact velocities in the range 2300 to 3500 m/s to produce shock stresses between 100 kbar and 1 Mbar. They carried out extensive analysis of recovered samples and observed that cracks occurred in parallel zones separated typically by 0.3 mm. (Some of the results of SEAMAN et al. also show this.) Measurements of Δu_s, accurate only to about 40%, are given in Table 2.

DAVID et al., propose a numerical micromechanical model quite different in approach from that of SRI. It is based upon the stress needed to open cracks and make them grow in essentially discontinuous jumps. The critical stress for growth, σ^*, is assumed to be a linear function of pressure. For copper, the model parameters are δ = 0.3 mm (cracks open at last $\delta/3$ apart), Θ = 2.55 μs, where it is assumed that when cracks grow, they do so at a rate:

$$\frac{dc}{dt} = \frac{c}{\Theta} \frac{\sigma^2 - \sigma_1^2}{\sigma_f^2} \tag{32}$$

c being crack length, and σ_f the stress that a crack can support

$$\dot{\sigma}_1 = \begin{cases} 0 & \text{for } \sigma < \sigma_1 \\ \dfrac{\sigma_1^2 - \sigma^2}{2\Theta\sigma_1} & \text{for } \sigma > \sigma_1 \end{cases} \tag{33}$$

the last model parameter is the constant k defined as:

$$k = \sigma^*/P \tag{34}$$

which for copper is equal to 0.03. Good agreement is obtained in finite difference calculations of free surface velocity history using this rather simple model.

TABLE 2

SPALL RECOVERY DATA, FROM DAVID et al.

Flyer Plate Velocity (m/s)	Flyer Thickness (mm)	Thickness (mm)	Peak Particle Velocity (m/s)	Δu_s (m/s)
3500	3	20	3200	520
		25	2800	450
		30	2530	380
		35	2235	250
		40	1190	220
2700	3	25	2300	250
		30	2150	230
		35	1950	200
		40	1850	120
(80 mm diameter targets and flyers)				

c. Other Properties of Copper

Table 3 contains a list of other properties of OFHC copper which are useful in finite difference modelling. These values are taken from the compilations given by CHRISTMAN and ISBELL and McMILLAN et al.

2. EXPERIMENTAL DETERMINATION OF SPALL THRESHOLD

The copper used in this program was supplied to the University by AFATL. It was in the form of a bar, 33 mm thick, and it was labelled as cross-rolled OFHC plate. Its hardness as used in these impact tests was RF48. The data for spall threshold determination is shown in Table 4. The shots used copper flyers and targets, except shot 109, in which an aluminum flyer plate was used to produce lower peak pressures; the peak pressure in shot 109 is equivalent to an impact with a copper flyer at 98 m/s. Peak stress values were calculated from standard Hugoniot data, namely, $U = 3.9u + 1.489$ (in units of mm/μs).

In many targets extensive void production was observed, although separation at the spall plane did not occur. Figure 15, for example, shows a section through the target in shot 109, and Figure 16 shows a view of the spall plane viewed on a surface parallel to the spall plane. It is evident that the mean density on this plane is about half the original sample density. Figure 17 shows a photomicrograph from shot 109 showing damage in the trajectory plane. Figure 18 shows a macroscopic view of damage caused by successively higher impact velocities. The data show that for the 1.5 mm flyer plates against 4.0 mm targets, void growth occurred at $u_o \geq 244$ m/s. For 2 mm flyer plates, spall separation occurred at $u_o \geq 168$ m/s. This is significantly less than the value for 1.5 mm plates suggesting rate effects are important. Another indication of results were obtained in shots 189 and 322; even though these impacts produced the same peak stress, the results differed. For 2.5 mm flyer plates, spall separation occurred at 286 m/s.

TABLE 3

PROPERTIES OF OFHC COPPER

Longitudinal sound speed C_L = 4.757 mm/μs

Shear wave speed C_s = 2.247 mm/μs

Density ρ = 8.917 g/cm^3

Expansion coefficient $\beta = 51.5 \times 10^{-6} + .006 \times 10^{-6} T$ °C^{-1}

Heat capacity C_p = 0.0915 + 0.00003T cal/g

Melting temperature T_m = 1080°C

Boiling temperature T_b = 2595°C

Heat of fusion L_f = 49 cal/g

Heat of vaporization L_v = 1146 cal/g

Bulk modules K_s = 1418 kbar

$\partial K_s/\partial T = 0.278T$

$\partial K_s/\partial P = 5.53$

Shear modules μ = 450 kbar

$\partial \mu/\partial p = 1.30$

Gruneisen parameter γ = 2.13

$\partial \gamma/\partial T = 0.00076$ °C^{-1}

$\partial \gamma/\partial P = 0.002$ kbar^{-1}

Low pressure Hugoniot $\sigma_h = 1.5 + 3.44u^2 + 143u^2$

High pressure Hugoniot (>1 Mbar) U = 3.964 + 1.463u

Hugoniot elastic limit, (anomalous precursor behavior, best value)

σ_{HEL} = 8 kbar

Release wave speed $C_r \geq 5.3$ mm/μs, no elastic/plastic separation observed.

TABLE 4

COPPER DATA SHOTS

Velocity (m/s)	Max Stress (Kbar)	Flyer Thickness (mm)	Target Thickness (mm)	Shot No.	Remarks
80	14	1.50	4.00	121	No voids
103	19	1.45	3.90	111	Void layer
244	45	1.45	4.00	110	Spall separation
168	30	2.0	4.00	221	Spall separation
189	35	2.0	4.00	220	Spall separation
322	35	2.0 (Al)	3.96	109	Void layer
286	53	2.5	3.94	108	Spall separation
334	62	2.5	4.00	222	Spall separation

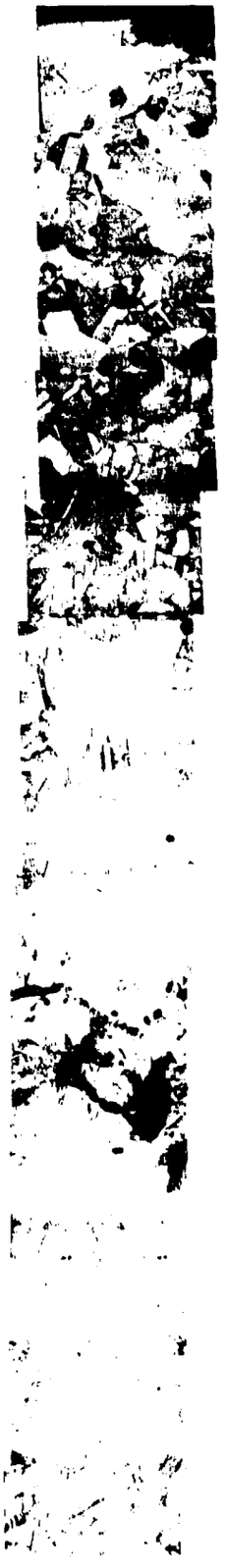

Figure 15.
Section through Target from Shot 109, Showing Void Layer. (The Crater on the Impact Surface in a Central Fiducial Mark Implaced after the Shot).

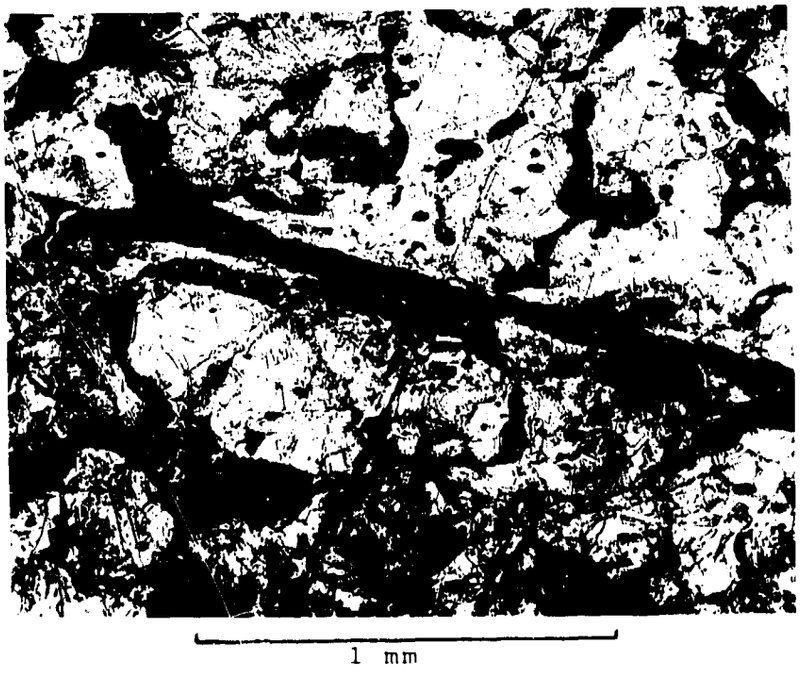

Figure 16. Photomicrograph from Shot 109, Taken in Incipient Spall Plane.

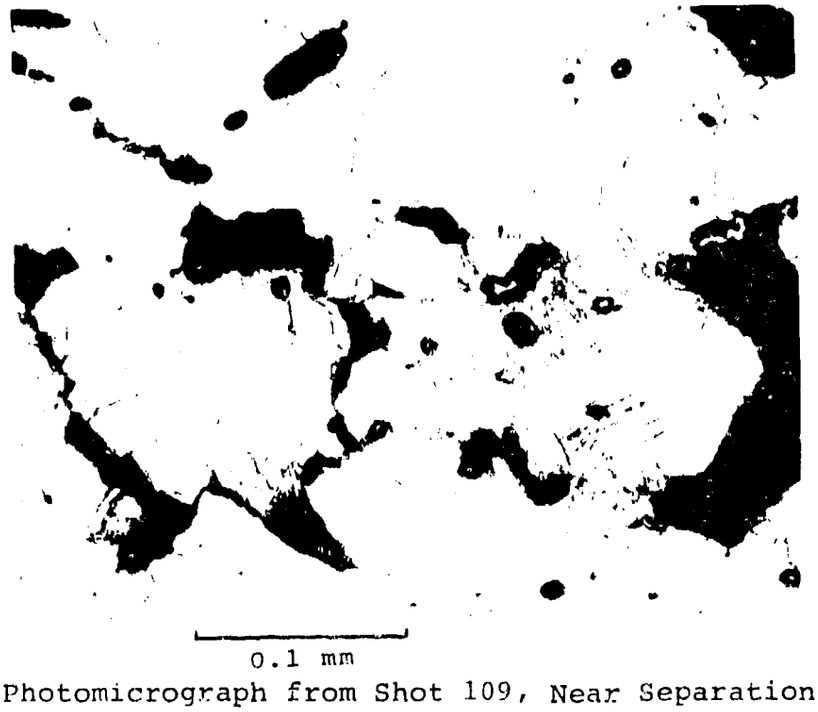

Figure 17. Photomicrograph from Shot 109, Near Separation Plane.

Figure 18. Comparison of Copper Targets from Shots 109, 221, and 220.

The range of impact parameters over which void formation occurs is comparatively large in copper. As a practical manner, the spall criterion used by CHRISTMAN and ISBELL is a useful definition: a 50 percent reduction in cross sectional area on the incipient spall plane.

3. VISAR DATA FOR COPPER

Good VISAR data were obtained on two copper shots: 222 and 220. The free surface records were distinctive for their rather featureless shape. Figure 19 shows the oscilloscope data for shot 222. The "spall signal" is very small, indicating that σ_s is very small. The VISAR data are summarized in Table 5. The parameters in Table 5 are defined in Figure 12.

4. THRESHOLD CRITERIA

The threshold data from this work and from CHRISTMAN and ISBELL are plotted in Figure 20. SWAP calculations were carried out for the spall threshold data. The input parameters were based on the conclusions in Section III.1. The SWAP model for release waves was a simple elastic plastic process with no strain hardening or softening. The VISAR data did not reveal sufficient structure in the release process to warrant more elaborate models. The parameter K_λ was calculated from

$$K_\lambda = \int (|\sigma-\sigma_0|)^\lambda dt$$

On the incipient spall plane, taken as $x = T - d$. The nucleation stress σ_0 was set equal to -5 kbar, based on the results discussed in Section 3.1, and $\lambda = 2$ as discussed in the Introduction. The resulting values of K_λ are shown in Figure 21, where they are plotted against flyer plate thickness d.

An uncertainty in the u_c data of CHRISTMAN and ISBELL of 10 m/s should be applied in Figure 20 for $d < 2$ mm, based on the scatter in their results. The data for $d = 0.4$ is for a target in which the peak shock stress was seriously eroded by the release

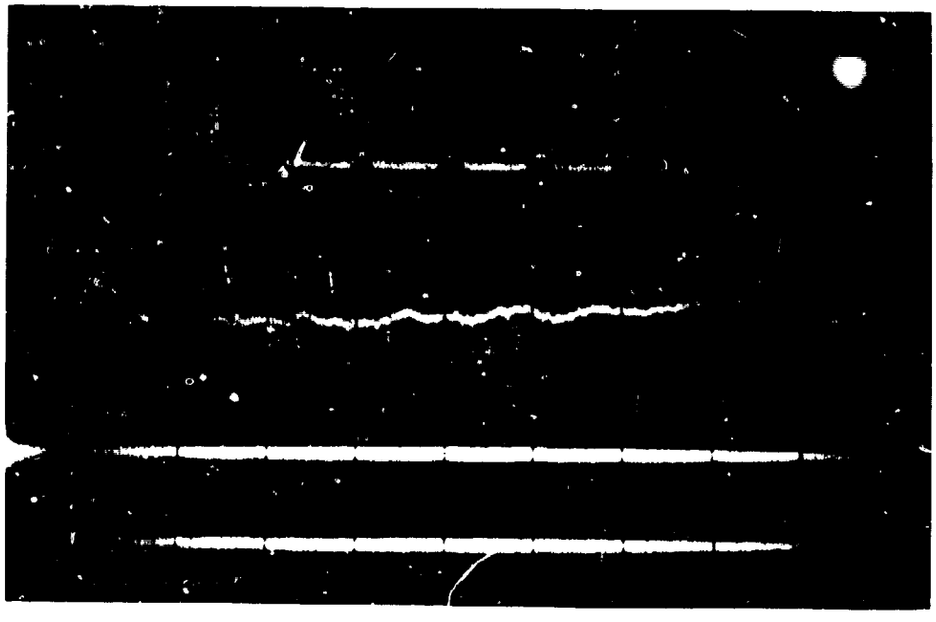

Figure 19. VISAR Record for Copper Shot 222. Fringe Constant was 322 m/s.

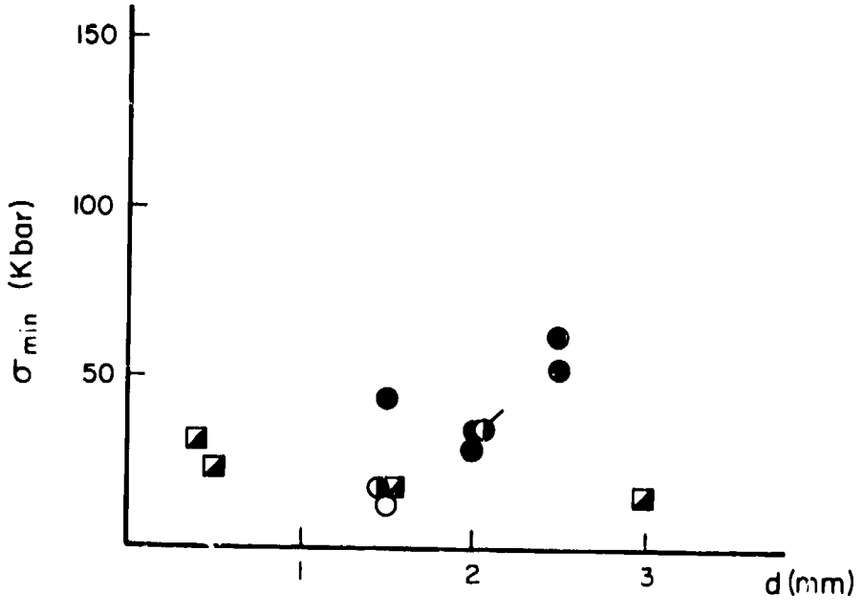

Figure 20. Most Tensile Stress vs Flyer Plate Thickness for Spall in Copper. (Shading indicates extent of spall. Circles are present work. Flag marks shot with aluminum flyer plate.)

TABLE 5

SUMMARY OF VISAR DATA FOR COPPER

(Units = μs and m/s)

Shot Number	222	220
t_p	.07 ± .03	.25 ± .03
t_{r1}	NR	.84 ± .05
t_{r2}	1.18 ± .03	.93 ± .05
t_s	1.25 ± .03	1.24 ± .03
t_b	NR	NR
Δv_s	20 ± 5	18 ± 5
Δv_f	1 ± 4	0 ± 5
v_p	365 ± 20	191 ± 10
v_{min}	345 ± 20	173 ± 10

wave from the flyer rear surface. This result is much more sensitive to the treatment of the release process in SWAP than are the other data points. The value for K_λ for this point is thus less reliable.

It is evident from Figure 21 that the value of K_2 is a much more volatile function of impact velocity than is σ_{max}. The data can be described by $50 < K_{2c} < 110$ kbar^2 - μs with two exceptions. The first is the datum at d = 0.4. As already discussed, this datum is considerably less precise than its neighbors, and can probably be disregarded. The other anomalous point is from shot 109, in which an aluminum flyer was launched at a copper target. In the SWAP calculation, the description of aluminum used by BARKER and YOUNG was employed. The SWAP calculations of K_{2c} are unlikely to be in serious error. Increasing σ_0 to -10 kbar, or decreasing λ to 1 does not significantly reduce the discrepancy between this shot and the others with copper flyer plates. The origin of the discrepancy has not been resolved at this time. Since it is a singular occurrence, it is recommended that a value of K_{2c} = 50 to 110 kbar^2 - μs be employed as a spall threshold predictor for copper.

5. OVERDRIVEN SPALL

The spall stress computed from the Δv_s data, using equation (21) turns out to be:

$$\sigma_s = -3.2 \pm 0.8 \text{ kbar}$$

SWAP calculations also require values of $\sigma_s \sim -5$ kbar to reproduce the VISAR data. This is considerably less than the values reported by DAVID et al. and by CHRISTMAN and ISBELL. We do not have an explanation for why the values of σ_s observed here differ from past results. We note that the ratio of d/T was only half that used by CHRISTMAN and ISBELL, the smaller ratio of d/T would probably lead to a large value of v' (as discussed in Section 2). The VISAR data also showed that the residual stress on the spall plate, σ_1, is essentially zero.

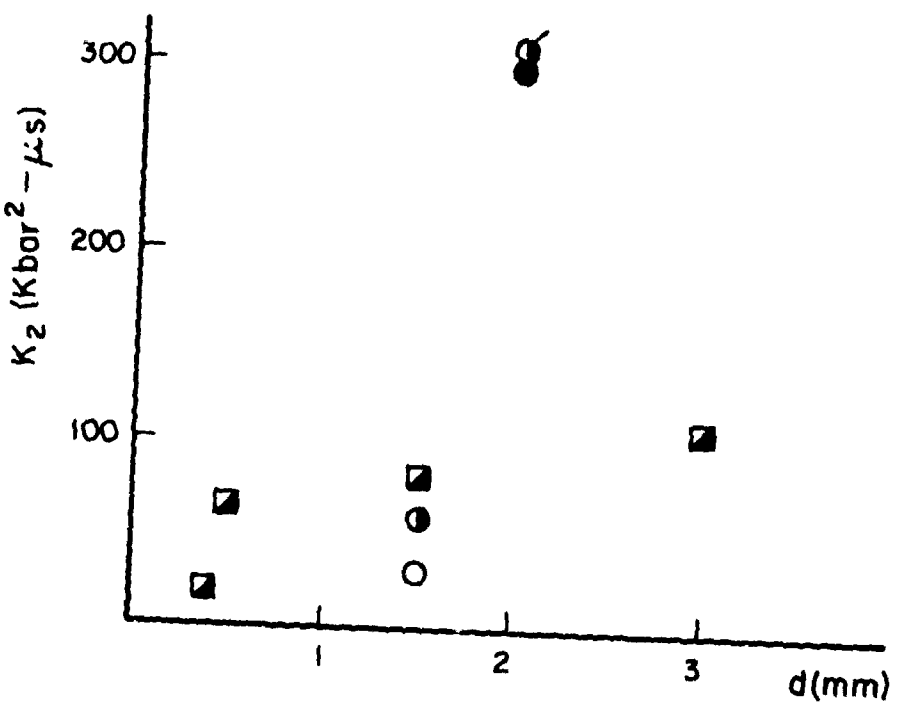

Figure 21. Damage Parameter K_2 for Spall in Copper. (Same symbol definition as in Figure 20.)

The result that $|\sigma_s| < |\sigma_0|$ is implausible. One way to reconcile the disparity in results is to invoke a sudden loss in fringe contrast in the records obtained in this program. CHRISTMAN and ISBELL used a specularly-reflecting VISAR, which may have been less sensitive to the mechanism responsible for contrast degradation. On the other hand, loss of fringe contrast is not self-evident in the data. Perhaps for reasons not yet determined, spall signals are difficult to observe in copper. It is recommended that this problem be subjected to further investigation.

The Δv_s data of CHRISTMAN and ISBELL give $\sigma_s = -20 \pm 1$ kbar for three shots with 1 mm flyer plates and $\sigma_s = -31$ kbar for 0.5 mm flyer plates. The correction to these values due to the $\Delta v'$ effect discussed in Section II is relatively small, since copper has relatively low yield stress. Calculations of K_{2c} give 22 to 53 kbar^2 - μs for the shots with d = 1 mm, and 24 kbar^2 - μs for the shot with d = 0.5 mm. The slight discrepancy between these values and the values of K_{2c} derived from the threshold shots should not result in significant errors in predictions of spall location and time of occurence. For the present, it is recommended that K_{2c} = 75 kbar^2 - μs for prediction of spall of OFHC copper.

6. STRAIN AT FAILURE

Between threshold conditions and overdriven spall, failure occurred at computed values of $-15 < \sigma_s < -31$ kbar. The corresponding value of ε_f, from SWAP calculation, are $0.01 < \varepsilon_p < .022$. For prediction purposes, a mean value of $\varepsilon_p = .015$ can be used. The value of $\bar{\sigma}/Y$ at this point was 4.9. The uncertainty in this figure, due to possible errors in deviatoric stress, is about ±25 percent. This fracture datum should be compared with the datum from the expanding cylinder experiments, $\varepsilon_p = \sim 1.0$ at P/Y = 0/3. The dependence of the critical value of ε_p on P/Y is very significant. However, a ε_p failure criterion by itself misses the essential time-dependence of spall-type fracture in copper.

SECTION IV
RESULTS FOR SAE 1020 STEEL

1. PREVIOUS WORK

The mechanical properties of mild steel have been discussed by many authors. Recent data, as well as a pertinent review, can be found in BLESS and BARBER (1979). In their study, the 1020 steel hardness was Rockwell B 81.2. Tensile tests were performed with conventional testing machines and with a split Hopkinson bar device operated by Dr. T. Nicholas at the Materials Laboratory, Air Force Wright Aeronautical Laboratories. The material was found to be significantly strain-rate dependent. The yield strength associated with the recovery from the overshoot increased from 3.29 kbar at 10^{-4}/s to 4.1 kbar at 1/s, to 6.6 kbar at 10^{3}/s. There was also no downward turning of the stress strain curve at the highest strain rate; this is apparently associated with the relative decrease in necking with strain rate. At 10^{3}/s the sample could not be driven to rupture because the load duration was limited to 300 μs. The true strain at failure was estimated from the cross sectional area of the failed region to be 0.9.

The SRI nucleation and growth model for fracture has been applied to Armco iron. It is a priori plausible that these parameters will apply to mild steel also. As given by SEAMAN and SHOCKEY (1972), the nucleation threshold stress is 3 kbar (p_o in equation 28). The sensitivity parameter, p_1 is 4.56 kbar. The growth threshold, p_{go} in equation (29), is -0.2 kbar.

Matuska has carried out Hull code calculations to try to reproduce the hemispherical impact data of BLESS and BARBER. He employed a work hardening model designed to fit the observed velocity decay - Y_o = 4.6 kbar, increasing linearly to 6.3 kbar at ϵ = 0.3, and thereafter constant. He used an ultimate failure criteria discussed in Section I.2. The ultimate failure surface was fit to the Hopkinson bar results. It passed through the points P/Y = 0.33 and ϵ_p = 0.9, and P/Y = 1.5 ϵ_p = 0.3. The HULL

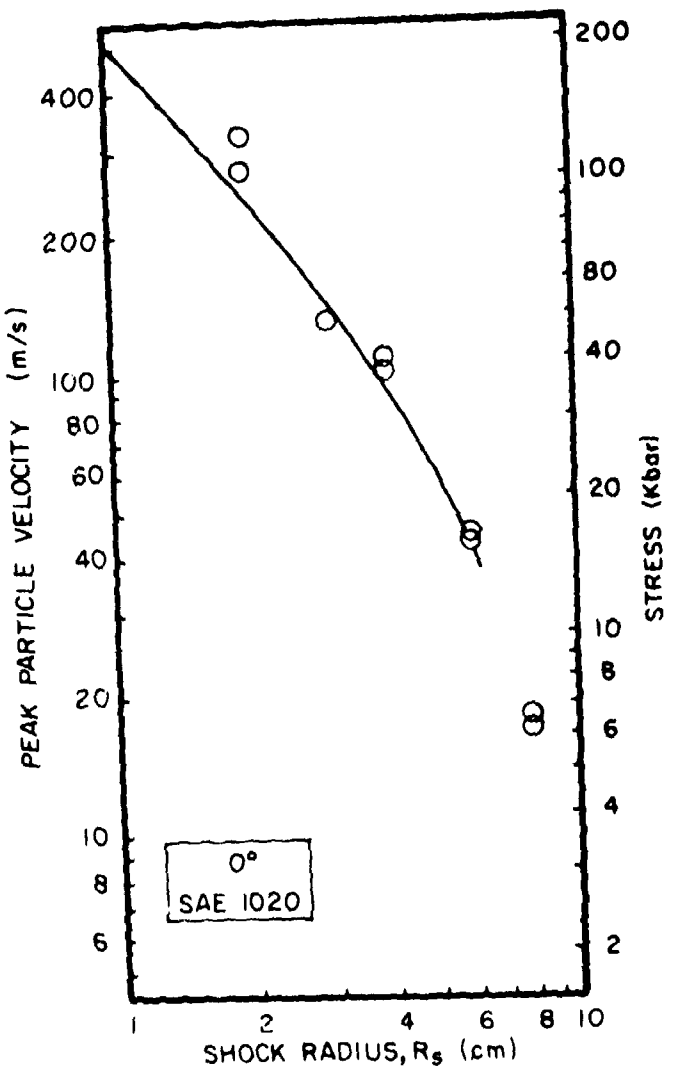

Figure 22. Comparison of Measured and Calculated Stress Delay in Impacted 1020 Steel Targets (from BLESS, BARBER, and MATUSKA).

calculations were able to reproduce the observed velocity decay and failure patterns. This agreement was only obtained after interactions on yield and failure criteria. Figure 23 shows the calculated failure zones for the experiment pictured in Figure 1. This result is described by BLESS, BARBER, and MATUSKA. These fracture data for 1020 steel are graphed in Figure 4a.

The variation of release wave speed and bulk sound speed with pressure is essentially linear for α-ferrite. This is discussed in Appendix B.

2. EXPERIMENTAL DETERMINATION OF SPALL THRESHOLD

The material used in the study was commercial SAE 1020 steel. Representative microstructures are shown in Figure 24. The hardness varied from sample to sample. The range for almost all targets was RB 62 to 75.

The data shots for spall threshold for 1020 steel are summarized in Table 6. The compressive stress is calculated from the α-phase iron Hugoniot (VAN THIEL et al., 1968).

$$U = 4.62 + 1.74\ u$$

Tensile stress maxima were computed with the SWAP code, as described below. There was no discernible variation in the position of the spall plane for 2 mm flyers; the values were all nearly 1.9 mm. In the shots with 1 mm flyers, spall thickness was only 0.65 mm to 0.79 mm. The experimental spall thresholds may be summarized as follows: for 1 mm flyers and 5 mm targets, $251 < u_c < 346$ m/s. For 2 mm flyers and 5 mm targets, $u_c \sim 239$ m/s.

Measurements were made of microhardness in shot 58 across a cross section. In the center of the shocked region the hardness was VH 148. No softening on the incipient spall plane was detected.

The evidence from the threshold experiments indicates that under the circumstances considered here, tensile rupture is so abrupt that it would probably not be useful to consider a partial-damage model. In only two shots were voids nucleated that failed

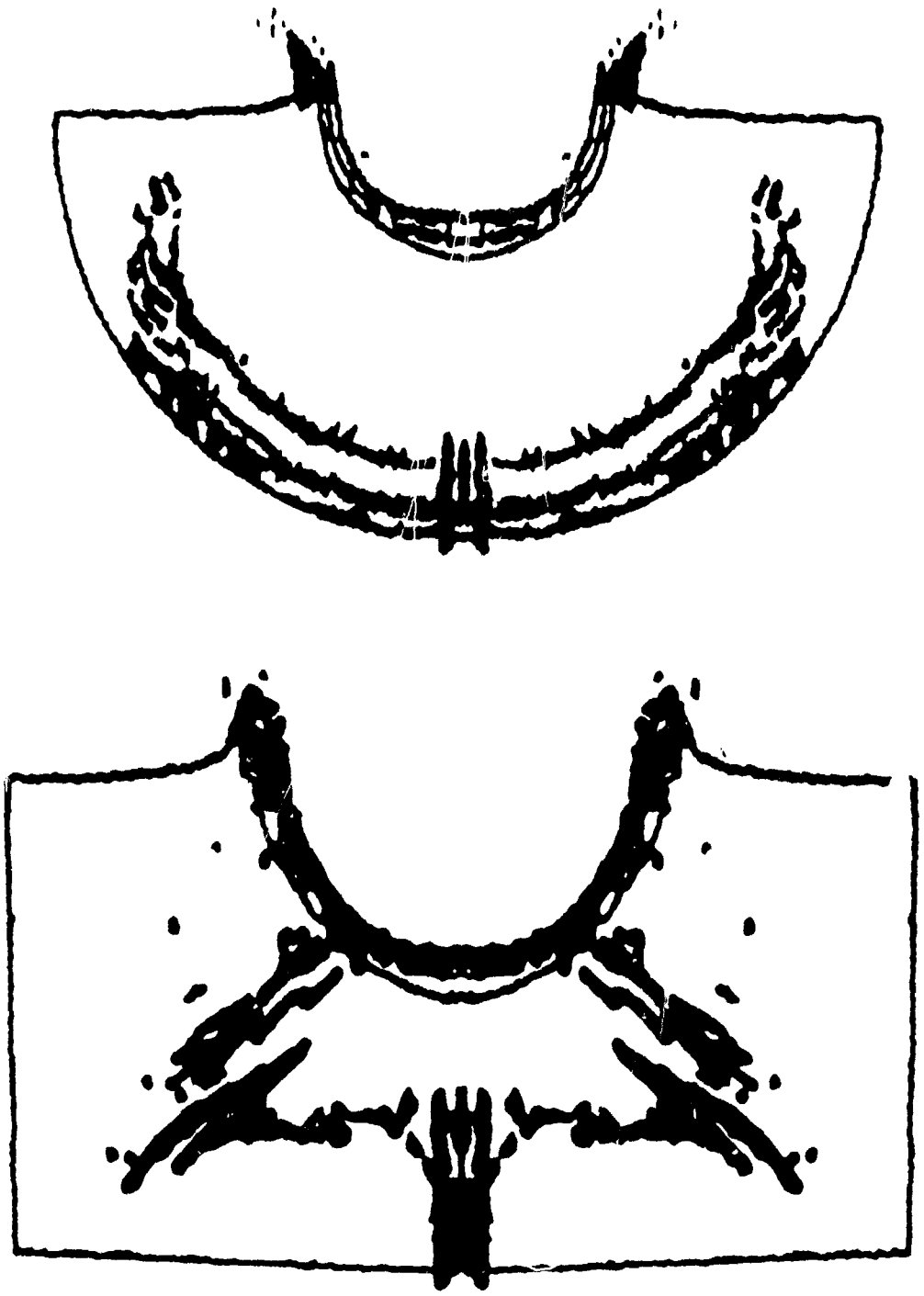

Figure 23. Agreement to Observation of Figure 1 Obtained With Hull Code Calculation (From BLESS, BARBER and MATUSKA).

(a) 300 x
1020 Steel,
Shot 42

(b) 300 x
1020 Steel,
Shot 53

Figure 24. Sample Microstructure of 1020 Steel. (These specimens Were Taken from Edge of Target Plates, Unaffected by Impact).

TABLE 6

SUMMARY OF SPALL OBSERVATIONS FOR 1020 STEEL

Velocity m/s	Flyer Thickness (mm)	Target Thickness (mm)	Max. Compressive Stress (kbar)	Max. Tensile Stress (kbar)	Shot Number	Hardness (RB)	Spall
545	1.0	4.0	109		223	74	Complete
574	1.0	4.0	115		63	84	Complete
136	1.0	5.0	25		53	64	No
251	1.0	5.0	49	38	58	69	No
279	1.0	5.0	53	43	269	79	Voids
346	1.0	5.0	68	55	54	70	Complete
524	1.0	5.0	102		42	79	Complete
239	2.0	5.0	47	39	107		Isolated voids
283	2.0	5.0	53		55	60	Complete
478	2.0	5.0	93		41	82	Complete
571	2.0	5.0	112		24		Complete
664	2.0	5.0	135		112		Complete
548	2.0	4.0	107		11	82	Complete
582	2.0	4.0	115		13	75	Complete
1041	2.0	4.0	86		14	75	Complete
1223	2.0	4.0	229		10	62	Complete

to coalesce into a rupture plane. Shots differing in σ_{max} by only 4 kbar showed complete spall or no spall. Figure 25 illustrates the appearance of voids in a sub-threshold shot.

3. FREE SURFACE VELOCITY

VISAR data were obtained for both loading and unloading of this material. A summary of the shot configurations for which VISAR data were obtained is given in Table 7. The free surface trace parameters are given in Table 8. The elastic precursor was resolved in three shots as shown in Figure 26. The stress levels corresponding to these shots are approximately 9, 27, and 42 kbar, all for 4 mm thick targets. Only the low value is consistent with HEL data for α-iron: BARKER and HOLLENBACK found 10.5 kbar for 6.4 mm thick samples; MCQUEEN et al. give 14 to 15 kbar for "hard" iron, and 9 to 11 kbar for "soft" iron. The observed higher amplitude arrivals may be reflections of the elastic wave from the advancing plastic wave front; the data for both shots 14 and 23 are consistent with indistinct arrivals at ∿14 kbar. We conclude that the initial elastic wave was missed in those shots.

Figure 27 shows sample curves for release wave arrivals and spall signals. These shots were very helpful in developing a deviatoric stress model and spall criteria for use in SWAP calculations, as explained below.

4. SWAP MODEL

The SWAP models were tried using various descriptions of unloading, given in Table 9. All models employed identical loading description, appropriate for $\sigma_{max} < 130$ kbar, namely:

$$\rho_o = 7.846 \text{ g/cm}^3$$

$$C_o = 3.61 \text{ mm/}\mu\text{s (VAN THIEL, 1968)}$$

$$S = 1.75 \text{ (VAN THIEL, 1968)}$$

Figure 25. Void Structure in 1020 Steel on Incipient Spall Plane. Shot 107 300x.

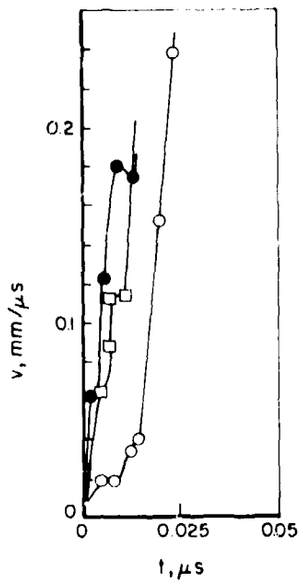

Figure 26. Observations of Elastic Precursor Signals. Shot 14 (Closed Circles) 63 (Open Circles), and Shot 223 (Squares)

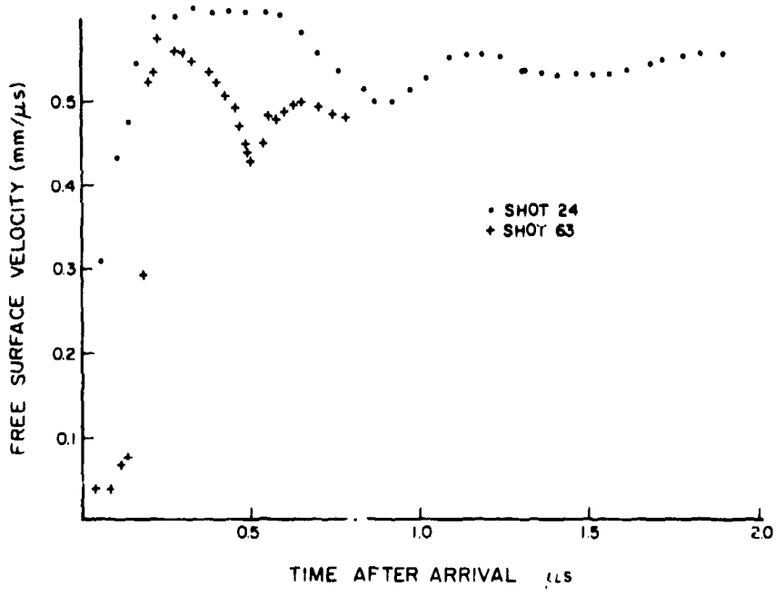

Figure 27. VISAR DATA from Shots 24 and 63.

TABLE 7

VISAR DATA AVAILABLE FOR 1020 TARGETS

Shot	d (mm)	T (mm)	Quality
223	1.0	4.0	Good
63	1.0	4.0	Good
14	2.0	4.0	Good
24	2.0	5.0	Good
13	2.0	4.0	Good
273	2.0	Cone	Fair
274	2.0	Cone	Good
275	2.0	Cone	Good

TABLE 8

FREE SURFACE VELOCITY PARAMETERS FOR 1020 STEEL

(Units = μs and m/s)

SHOT	223	63	14	24	13
t_p	.15 ± .03	.18 ± .02	.16 ± .02	.10 ± .02	.12 ± .05
t_m	.22 ± .01	.23 ± .01	.67 ± .02	.16 ± .02	.28 ± .02
t_{r1}	.40 ± .01	.24 ± .01	.78 ± .02	.61 ± .01	.65 ± .02
t_{r2}	.43 ± .01	.31 ± .01	NR	NR	NR
t_{r3}	NR	.46 ± .01	NR	NR	NR
t_s	.53 ± .01	.51 ± .01	.88?	.90 ± .02	.85 ± .02
t_B	.57 ± .01	.56 ± .01	NR	.97 ± .02	.92 ± .02
v_p	576 ± 15	574 ± 10	950 ± 15	600 ± 15	550 ± 10
v_{min}	940 ± 10	428 ± 10	685 ± 15	490 ± 10	430 ± 5
v_E	115 ± 10	39 ± 5	180 ± 10	NR	
Δv_s	140 ± 10	146 ± 10	265?	100 ± 10	120 ± 10
Δv_f	20 ± 5	92 ± 10	NR	65 ± 10	90 ± 15
v_{r2}	25 ± 5	16 ± 5	NR	NR	NR
v_{r3}	NR	81 ± 10	NR	NR	NR

TABLE 9

VALUES OF YIELD PARAMETERS FOR VARIOUS SWAP MODELS

Model C gave the best agreement with VISAR data.

Model	A	B	C
Y eq.	1	2	3
Y_o	7.124	6.50	6.30
y_1	0.3125	3.20	4.60
y_2	7.36	60.68	0.3

y eq. 1: $Y = Y_o(1+y_1\varepsilon)(1-\frac{W}{Y_2})$ (W is internal energy)

y eq. 2: $Y = Y_o(1+\alpha P)$ (P is hydrostatic stress)

$\alpha = (y_1/y_o-1)/Y_2$ y_1 is max Y at $P = y_2$

y eq. 3: $Y = Y_o(1+\alpha\varepsilon_p)$ (ε_p is plastic strain)

y_1 is max Y at $\varepsilon_p = y_2$

$$\gamma = 1.25 \text{ (BARKER and YOUNG, 1974)}$$

$$\partial\gamma/\partial\varepsilon = -10 \text{ (BARKER and YOUNG, 1974)}$$

$$\partial\mu/\partial P = 0$$

Model A has a constant yield stress that has been adjusted to describe our observed elastic processor. Model B includes the yield description used by BARKER and HOLENBACK 1972, for Armco iron. Model C (strain hardening) is the one used by Matuska to duplicate the results of BLESS and BARBER. The differences in assumed yield stress cause the variations in the amplitudes of the first two release arrivals which are elastic reflections from the elastic precursor and main shock at the back of the flyer plate. Figure 28, for example, illustrates the release wave fronts generated by these models, crossing the impact plane. Model C clearly gave the best agreement with data. Figure 29 shows the SWAP calculations for shot 24. The agreement with the VISAR data is good. Agreement in shot 63 was equally good. Shot 223 (Figure 30), however, showed the elastic wave arriving a little faster than in the SWAP model. It would appear that only a varying shear modulus could reproduce this result. In spite of this defect, the predicted time of arrival and amplitude of the spall signal are in excellent agreement with the data. Overall, the SWAP model was judged adequate for computing stress histories on spall planes.

5. SPALL THRESHOLD CRITERIA

Spall threshold data are graphically summarized in Figure 31. The SRI data for Armco iron are also included. It can be seen that the 1020 steel tested here is clearly more resistant to fracture than the iron.

SWAP runs were carried out to calculate K_2 on the incipient spall planes for 1 mm and 2 mm flyer plate impacts. The parameter σ_o was varied until the same value of K_{2c} was obtained for both conditions. The optimum value was $\sigma_o = -29 \pm 1$ kbar. For $\sigma_o = -29$ kbar, spall occurred when $K_2 = 34 \pm 1$ kbar^2 -μs.

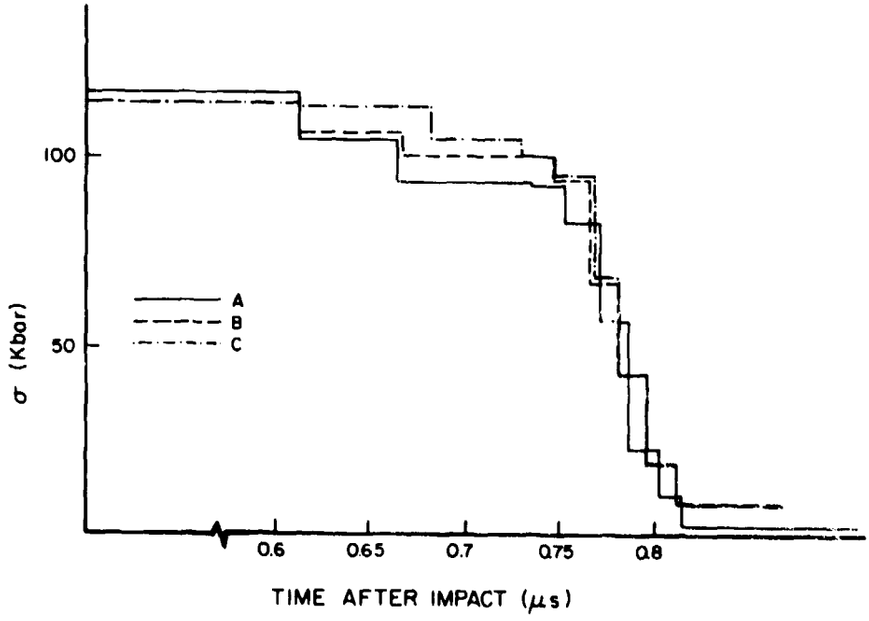

Figure 28. Release Waves from Flyer Free Surface Crossing the Impact Plane in Calculation for Shot 24

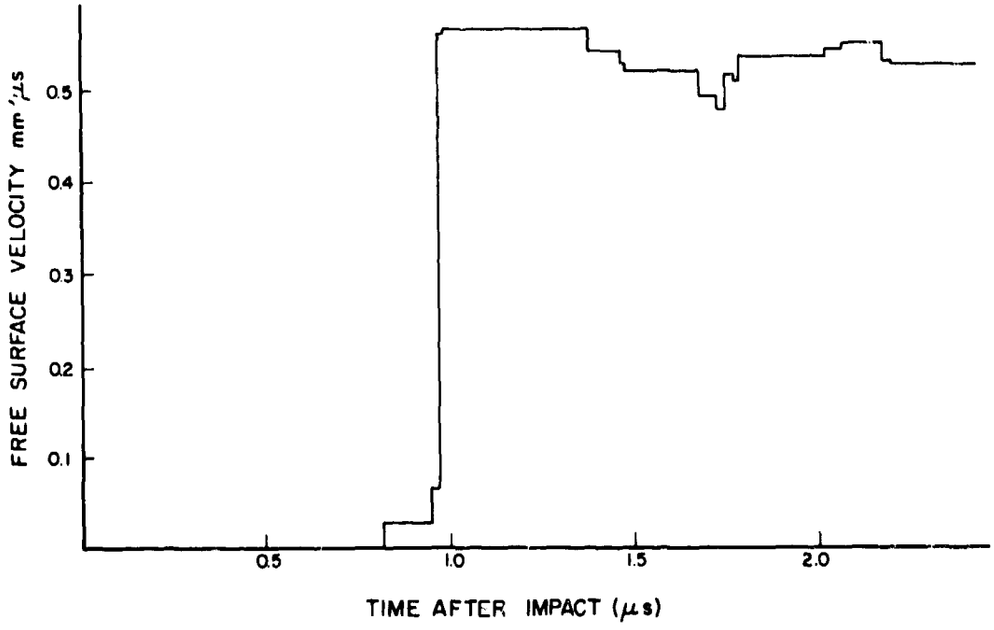

Figure 29. SWAP Result for Shot 24.

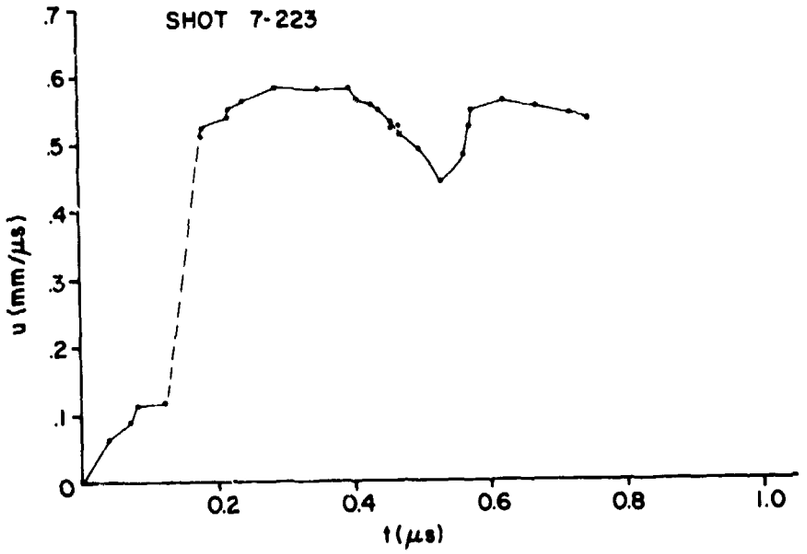

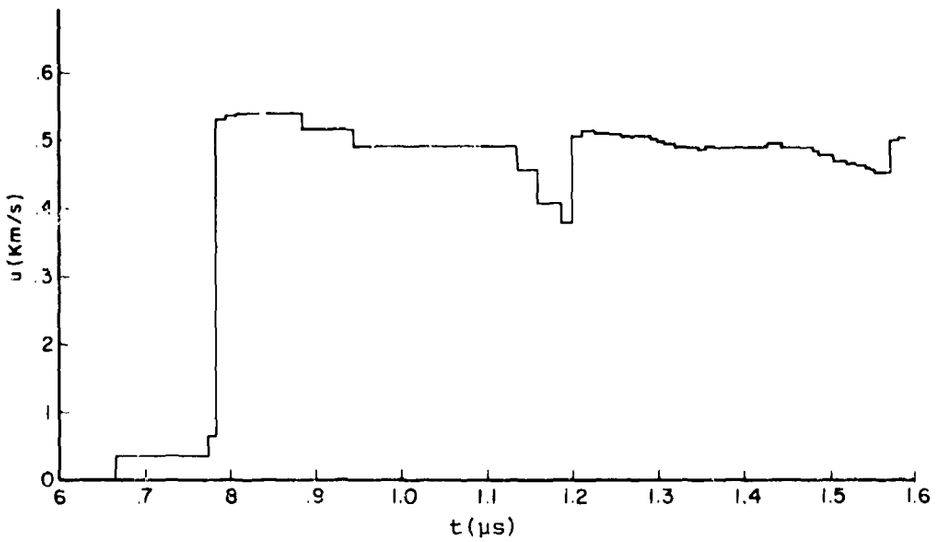

Figure 30. Comparison of SWAP Result and VISAR Data for Shot 223.

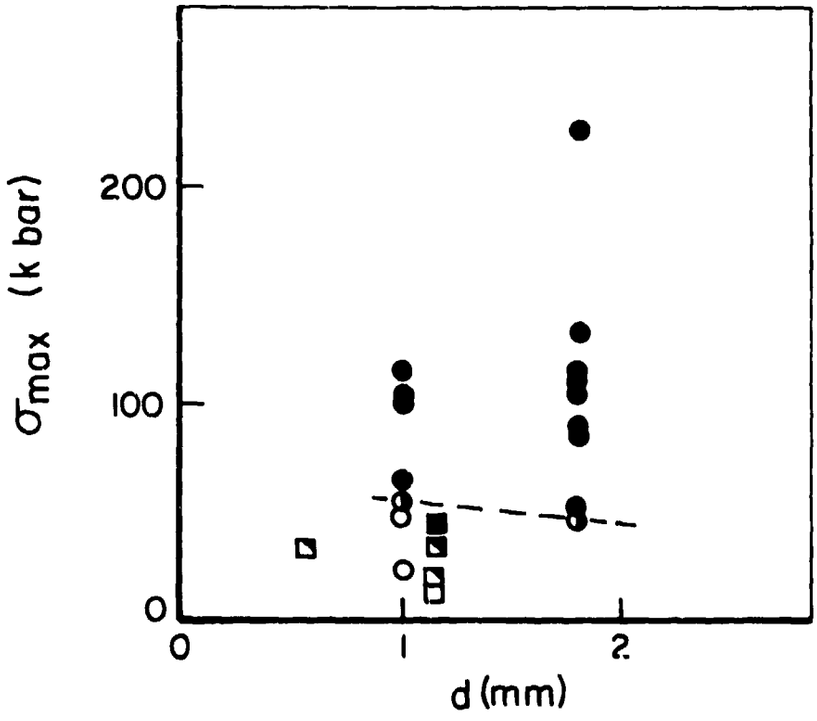

Figure 31. Data for Spall Threshold in 1020 Steel. (Squares are data from SEAMAN et al.; relative shading indicates extent of spall.)

6. OVERDRIVEN SPALL

The spall stress calculated from the VISAR data using equation (21) varies with flyer thickness. For d = 1 mm, $\sigma_s = -34 \pm 1$ kbar. For d = 2 mm, $\sigma_s = -25 \pm 3$ kbar. This is consistent with the present damage model. The release fan from thinner flyers is tighter, and thus the value of σ_o may be more exceeded.

Attempts to use SWAP to reproduce observed spall signals were not wholly satisfactory. The magnitude of Δv_s was relatively insensitive to σ_s. Values -40 to -50 kbar provided the best agreement, but the uncertainty is about ±5 kbar. The problem seemed to be that even finely zoned problems digitized release waves in $\sim$ 10 kbar steps. The SWAP calculations showed the spall shock travelling at the longitudinal elastic sound velocity, and that value was used to calculate the values of σ_s given in the preceding paragraph. The SWAP calculations showed that the errors in using equation (21) may amount to as much as a factor two in spall stress. It is, therefore, concluded that the most accurate measures of σ_s are the relatively imprecise values required to bring SWAP and VISAR data into agreement. In other words, $\sigma_s = -45 \pm 5$ kbar for both 1 mm and 2 mm thick flyers, when $u \gg u_c$.

The SWAP code was used to estimate K_{2c} in cases of rapid spall. It turned out that the values were very small, between 5 and 10 $kbar^2$ - μs. Uncertainty in K_{2c} is probably of little practical importance because exact values of σ_s and K_{2c} have very little effect on the location or time of spall fracture. In most impact situations, when K_{2c} is exceeded, it is exceeded very quickly, and it is first exceeded in the region where $\partial\sigma/\partial t$ has the most negative value. A more complete model is obtained by considering K_{2c} a function of σ_{min}, as shown in Figure 32. According to this model, the threshold, criterion involving K_{2c} and σ_0 is only important near the threshold, where σ_{min} does not exceed σ_o by more than about 10 kbar. For more extreme value of σ_{min}, spall takes place more rapidly than would be predicted by a constant value of K_{2c}. This conclusion is relatively insensitive to the value of σ_s.

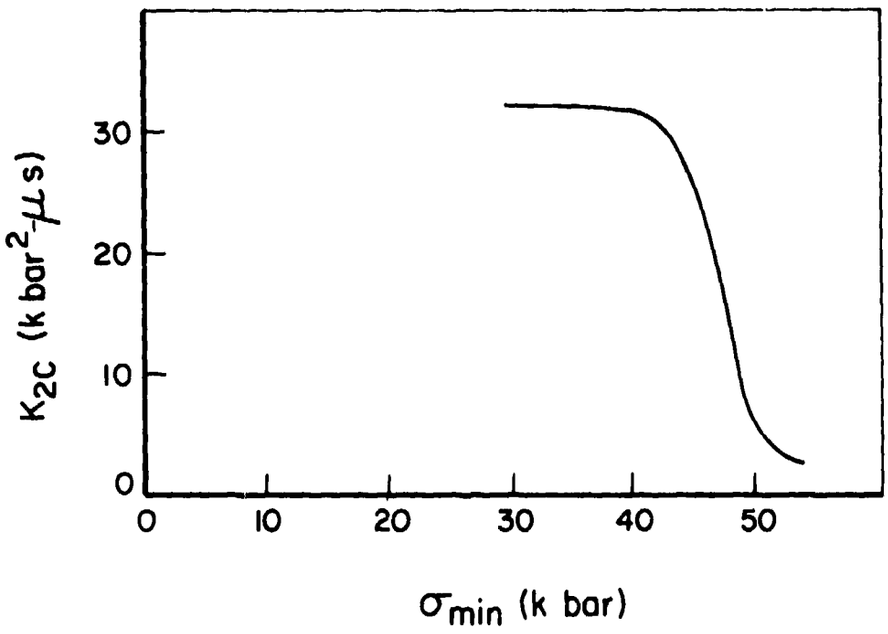

Figure 32. Variation of K_{2c} with σ_{min} for 1020 Steel.

7. TWO-DIMENSIONAL TARGETS

A limited number of experiments were done with two-dimensional impacts in order to more effectively assess the effects of shear strain on fracture. The targets were cones 25 mm in height with a 90° included angle. They were machined from 1020 steel. The flyer plates were 2 mm thick, 38 mm diameter, 1020 steel discs. The shot matrix is presented in Table 10. Predictions of the results of the impact were made by staff at the Air Force Weapons Laboratory (AFWAL) using the HULL code. Figure 33 illustrates a target before impact. A single crush pin was emplaced to provide a trigger for instrumentation. Table 10 lists the shots.

a. Fracture of Conical Targets

Figure 34 through 36 show cones recovered from several shots. It can be seen that fracture developed on four separate systems. A spall-type fracture developed parallel to the cone surfaces. This fracture was apparently the first one to develop, and it is first manifest at about midheight.

The second fracture system consisted of radial cracks which initiated on the cone surface. These cracks seemed to form at separation angles of 35 to 40°. They were influenced by the presence of the crush pin hole. The jagged appearance of the cracks suggests that they were formed very rapidly over much of the surface of the cone. The earliest cracks coalesced, and the later cracks were arrested.

The third crack system was a roughly cylindrical failure about 12 mm in diameter symmetric to the cone axis. This failure resembles base failures in impacting cylinders observed by PAPIRNO et al. Lastly, there was a radial crack system expending outward from the cylindrical fracture surface. Its trace was clearly visible on the impact surface. These cracks were spaced by about 90°.

b. Surface Velocity

Surface velocity was measured by Hopkinson flyoff plates and by the VISAR. Hopkinson flyoff plates are small discs

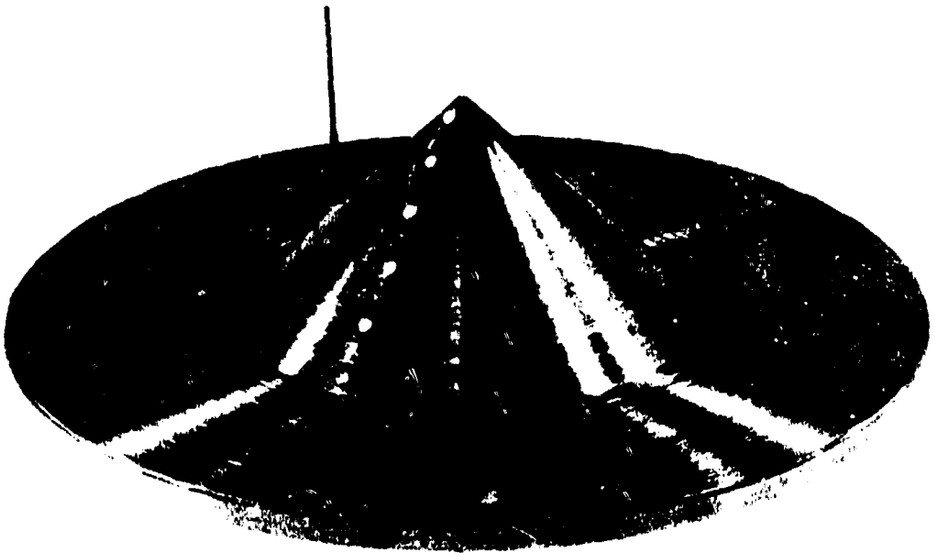

Figure 33. Preimpact Photograph of Conical Target from Shot 276 .

Figure 34. Cross Section of Recovered Cone in Shot 273, u_o = 383 m/s.

Figure 35. Top View of Cone Recovered from Shot 277.

Figure 36. Base View of Cone Recovered from Shot 277.

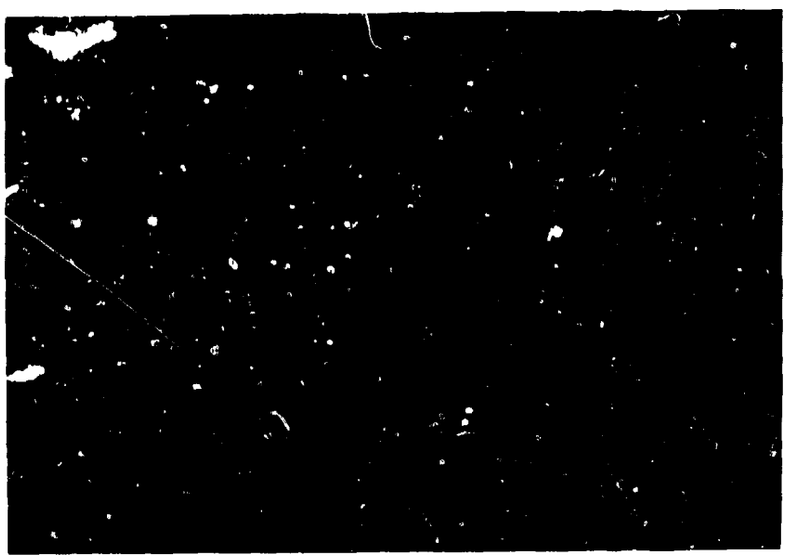

Figure 37. Flyoff Plates in Motion from Shot 277.

Figure 38. Superimposition of Preimpact and Postimpact Frames from Shot 278. (Separated by 42 μs)

TABLE 10

SHOTS WITH 1020 STEEL CONES

Flyer plates were 2.0 mm thick.

Shot Number	(mm/μs)	Diagnostics
273	0.383	VISAR
274	0.520	VISAR
275	0.504	VISAR
276	0.489	Streak camera
277	0.493	Flyoff discs
278	0.490	Flyoff discs

that are placed on the target surface; they are launched at the peak free surface velocity. In shot 277, the discs were 0.05 mm steel shims, 1.7 mm in diameter (see Figure 33). They were contoured to the target surface and held in place by minute amounts of silicon grease. In shot 278, the disc size was decreased to 1.2 mm, and they were held in place by magnetization. The flyoff plates were placed on the two sides of the target silhouette. The motion of the flyoff plates was photographed by a Beckman and Whitley Model 300 framing camera at a rate of about 1.2×10^6 frames/s. Sample frames from shot 277 are shown in Figure 37 and 38.

Results of limited precision were obtained from the two flyoff plate shots. In shot 277 flyoff plates were relatively large and they only moved about 100 mm during the camera recording time. The normal velocity near the cone apex was 260 ± 20 m/s. At midheight it was 310 ± 30 m/s, and near the base it was 290 ± 30 m/s. The flyoff plates in shot 278 turned out to be too small to reliably observe, and no velocity data were obtained. The photographic data does clearly show the bulging of the target. The target reaches its final shape by 40 μs after impact. Reliability of flyoff plate data should be checked by using plates of varying size in order to show that the size of the geometry disc does not affect launch velocities. Since this test was not done, the quoted results should be regarded as upper bounds.

Three shots were carried out using the VISAR to measure free surface velocity history at a point 7 mm from the cone base. In one, only a digital oscilloscope recorded the data (due to triggering error, and the digitizing rate of 50 ns was too low to reliably follow the signal. Oscilloscope data from the other two shots are shown in Figures 39 and 40.

The normal velocity history is shown in Figure 41. It has been assumed there that no fringes were lost. The data are ambiguous in that the velocity at all points beyond the break in the curve could exceed that shown in the figure by 322 m/s.

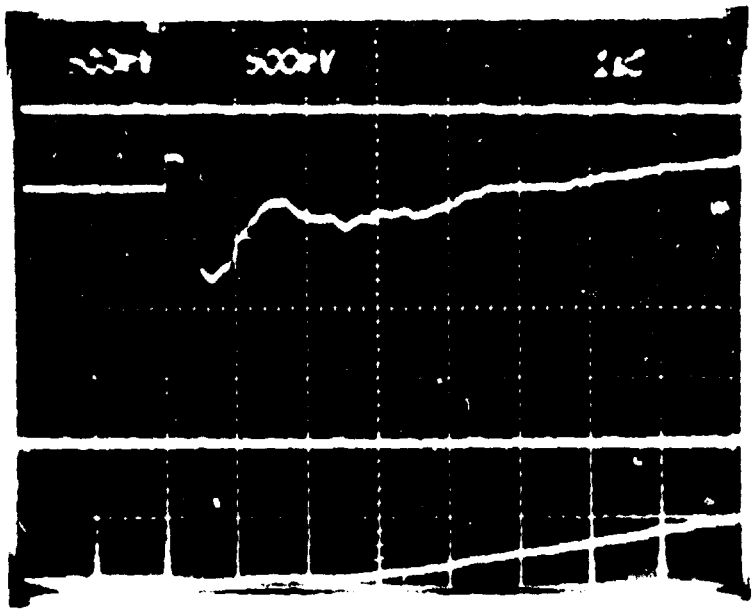

Figure 39. VISAR Record of Normal Surface Velocity from Shot 274.

Figure 40. VISAR Record of Shear Surface Velocity from Shot 275.

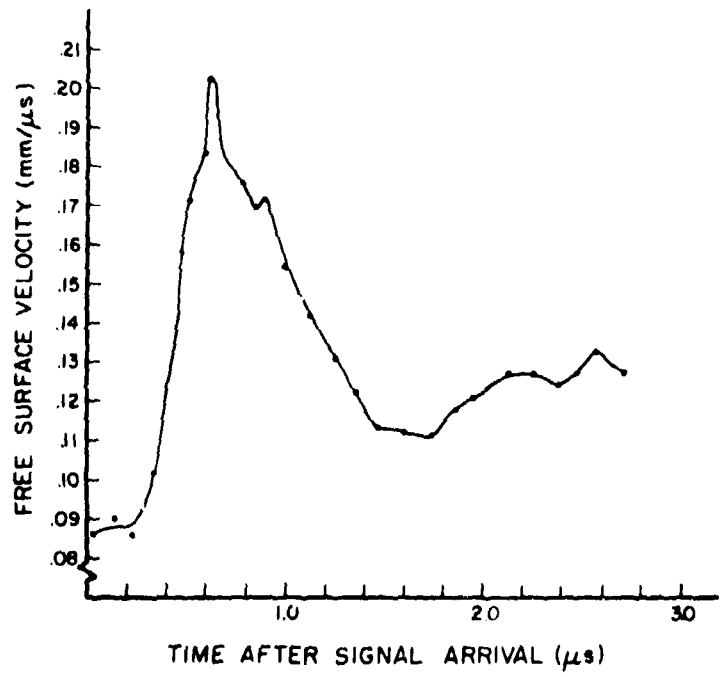

Figure 41. Velocity Data from Shot 274.

The uncertainty in velocity can be resolved with the aid of the data from shot 275. In this show the VISAR was incident at an angle of 45°, and viewed at an angle of 45°. The velocity measured by the VISAR is equal to $2v\sin\Theta_i$, where v is the free surface normal velocity and Θ_i is the angle of incidence. (Initially an error was made in this derivation and it was thought that the measured velocity was sensitive to the in-plane motion of the free surface; measurement of the in-plane motion was the motivation for the shot). Due to the spread of viewing angles (about ±15°), there is probably loss of fringe contrast in shot 275. The peak measured velocity in shot 275, uncorrected for change in fringe contrast, is 59 m/s, giving V = 83 m/s. The actual velocity could have been higher by about 100 m/s, due to loss of fringe contrast. If the peak normal surface velocity was actually 522 m/s (corresponding to loss of a fringe in shot 275), then the measured peak velocity in shot 275 would have been 369 m/s, which means more than one fringe would have occurred in the first half microsecond. This interpretation seems clearly incompatible with the oscillograph. Thus, the data from shot 276 support the interpretation given in Figure 41.

c. Shock Arrival Velocity

The shock arrival velocity along the cone free surface was measured in shot 276. A rear-surfaced mirror was cemented to the surface. The rupture of the mirror was observed using a pulsed light source and a 70 mm streak camera. The velocity 14 mm above the base was 5.0 ± .05 mm/μs. 20 mm above the base the velocity was 4.61 ± .14 mm/μs. These are consistent with the plastic wave speed in steel.

d. Code Simulation

A HULL code simulation of the cone impacts was carried out by personnel from AFWL. The impact velocity was 500 m/s. No fracture criterion was used. Instead, the density

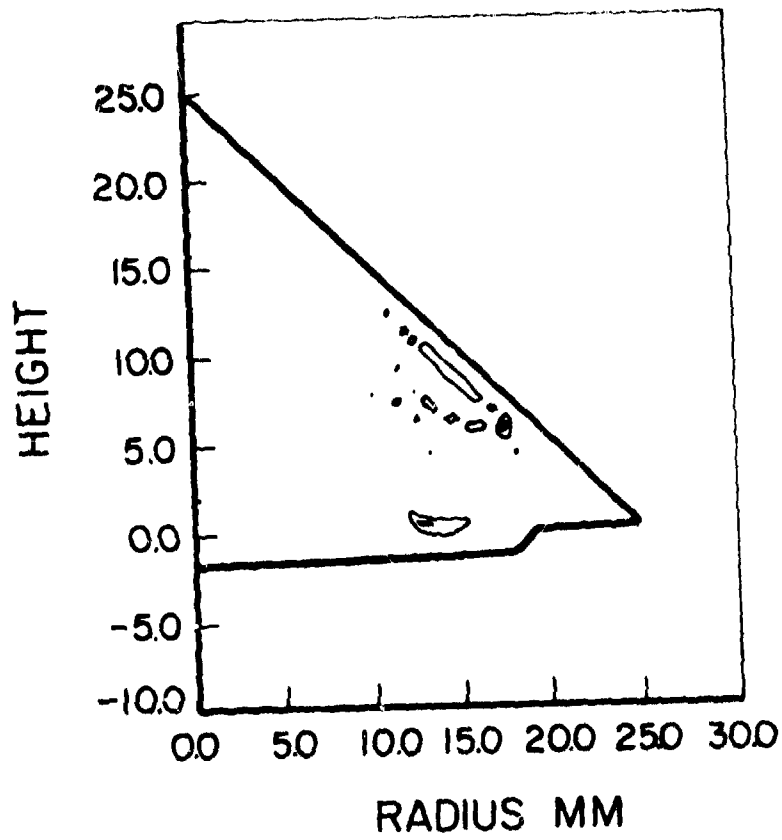

Figure 42. Density Contours 3.548 μs After Impact, from a HULL Calculation, Showing Regions Where $\rho < \rho_o$.

was allowed to drop to less than ρ_o. The result is shown in Figure 42 for the time at the end of the calculation.

The failure parallel to the free surface has been predicted. However, the fracture takes place 1.5 mm from the surface, whereas, actually the distance was 3 mm. The radial fracture patterns and interior conical fractures have not developed. At this time there are no negative stresses exceeding -15 kb, so further fractures near the cone base are unlikely. However, the compressive wave has not yet reached the apex, so additional fracture may occur in the upper part of the cone. In conclusion, it appears that the fracture model in the code is not adequate to predict at least some of the major features of the target response.

The peak free surface velocity predicted by the calculation is 200 m/s at 15 mm height, and 460 m/s at 7 mm height. These differ by about 50% from the measured values.

SECTION V
RESULTS FOR 4340 STEEL

1. LITERATURE REVIEW

Most of the physical properties of AISI 4340 steel do not differ significantly from SAE 1020 steel. The low pressure shock properties have recently been reported by FRANZ and ROBITAILLE. The α-phase Hugoniot is: $U = 4.67 + 1.44u$ (for units of mm/μs). According to these authors, the $\alpha \rightarrow \varepsilon$ phase transition takes place at 132 kbar. The longitudinal elastic wave speed is 5.86 mm/μs, and the bulk wave speed is 4.67 mm/μs. The ε phase Hugoniot of 4340 is the same as pure iron within experimental error.

The Hugoniot Elastic Limit (HEL) of 4340 steel varies widely. GUST reports apparently random variations from 10 to 28 kbar in RC58 material. Apparently, variation of 10% in σ_{HEL} may be due to effects of sample thickness. (The HEL decreases with propagation distance due to dissipation). GUST summarized HEL data. A plot of his summary, together with data of FRANZ and ROBITAILLE is shown in Figure 43. For the material used in this study, σ_{HEL} = 20 kbar is appropriate.

PAPIRNO et al. found that for RC 52 material, the dynamic yield point was the same as the static value at 50 percent strain, namely 25 kbar. BLESS and BARBER report dynamic stress strain curves of Nicholas for annealed material. Neglecting a short "overshoot", characteristic of high strain rate tests, the yield strength increased from 8.2 kbar to 11.3 kbar as $\dot{\varepsilon}$ increased from $10^{-4}s^{-1}$ to $10^{3}s^{-1}$. The ultimate strain was 0.16. BUTCHER and CANON also studied the effect of strain rate on yield. Soft material, RC 15 to RC 32 was quite rate dependent; however, RC 54 material was not.

There do not appear to have been previous studies of spall in 4340 similar to the present study. Cylinder impacts of 4340 were carried out by MESCALL and PAPIRNO. Their tests were with

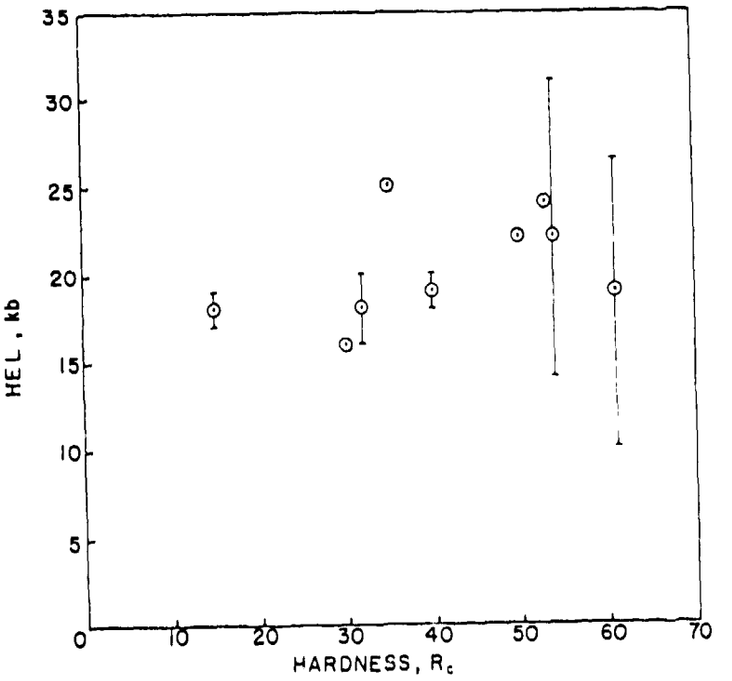

Figure 43. Variation of HEL With Sample Hardness for 4340 Steel (Various Sources).

RC15 material. They used a simple wave propagation code and achieved satisfactory agreement between post-shot observation of tensile failure and calculations. The spall model of a Tuler-Butcher form was used with $\lambda = 2$, $\sigma_o = 7$ kbar, and $K_{2c} = 337$ kbar^2 μs. These results were probably not very sensitive to the spall threshold criterion, since peak stresses were well above σ_o. NOVIKOV, et al. (1966), studied a Russian steel which is probably similar to 4340. In the annealed version ($Y = 4.4$ kbar), the critical rupture stress was 28.4 kbar. Rupture stress was calculated from free surface history measurements by equation (21). Thus, the rupture stress is similar to PSPALL as used in SWAP calculations.

Static studies of tensile fracture in 4340 have been carried out by several authors. COX and LOW reported valuable observations and summarized previous findings. Tensile failure initiates with spherical voids which grow at inclusion sites. The larger inclusions, principally MnS, nucleate voids first. The higher the purity, the higher the stress required to achieve a given void content. Voids coalesce by propagation of hairline cracks which involve fracture initiation at tiny cementite inclusions. The first hairline cracks grow parallel to the maximum shear stress. The amount of triaxiality in the stress significantly effected void growth and coalescence.

COX and LOW measured the fraction of void area on the cross sections. This was found to vary with stress state and material purity. It did not correlate with fracture strain. A typical curve is shown in Figure 44.

2. DATA FOR SPALL THRESHOLD

The 4340 material tested in this program was the same as used in BLESS and BARBER. It was vacuum remelted, and was RC30 ± 2.

The data for spall threshold for 4340 steel are shown in Table 11. For 1 mm flyers, there were some targets for which partial spall damage was observed. The range of stress over which this occurs was at least 6 kbar. In shot 56, although some voids were present in the polished section, the VISAR records did not indicate a spall signal. The threshold velocities for spall formation are very similar for 1 mm and 2 mm flyers. For 1 mm flyers, plates u_c = 360 m/s. For 2 mm flyer plates, u_c = 345 m/s. Both of these values are probably accurate to ± 10 m/s.

3. FREE SURFACE VELOCITY MEASUREMENTS

Table 12 lists the shots for which free surface velocity measurements are available. Table 13 lists the free surface velocity parameters for 4340 steel. The data for the shots are shown in Figures 45, 46, and 47. The oscillographs for shot 219 are given in Appendix C.

The spall signal varied little with velocity, even though in shot 15 the release was from the ε-phase. The average value of σ_s from equation (21) is -47 kbar.

4. SPALL CRITERIA

SWAP calculations were carried out for the threshold conditions of

(a) u_c = 345 m/s, d = 2.0 mm, T = 4.0 mm

and

(b) u_c = 360 m/s, d = 1.0 mm, T = 5.0 mm

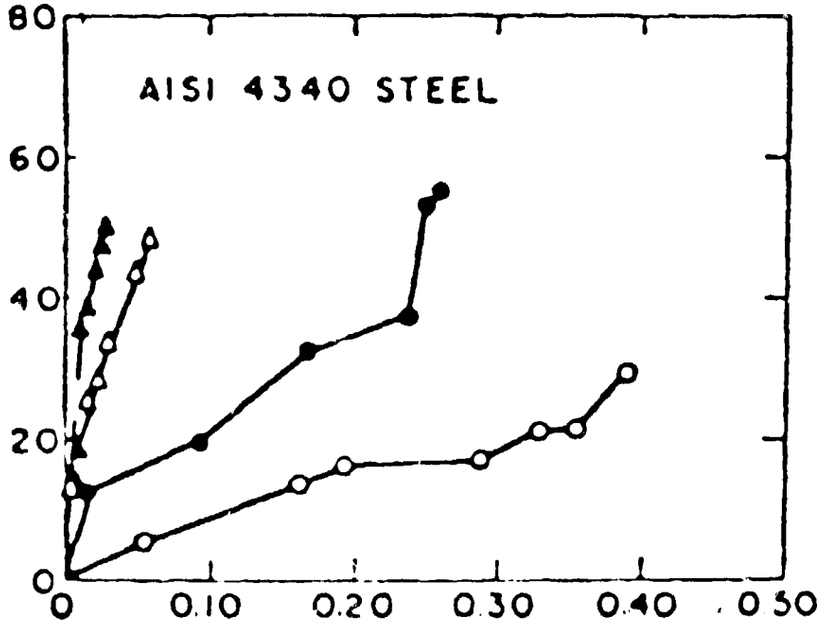

Figure 44. Average Cross Sectional Area of Voids Versus Strain, from COX and LOW.

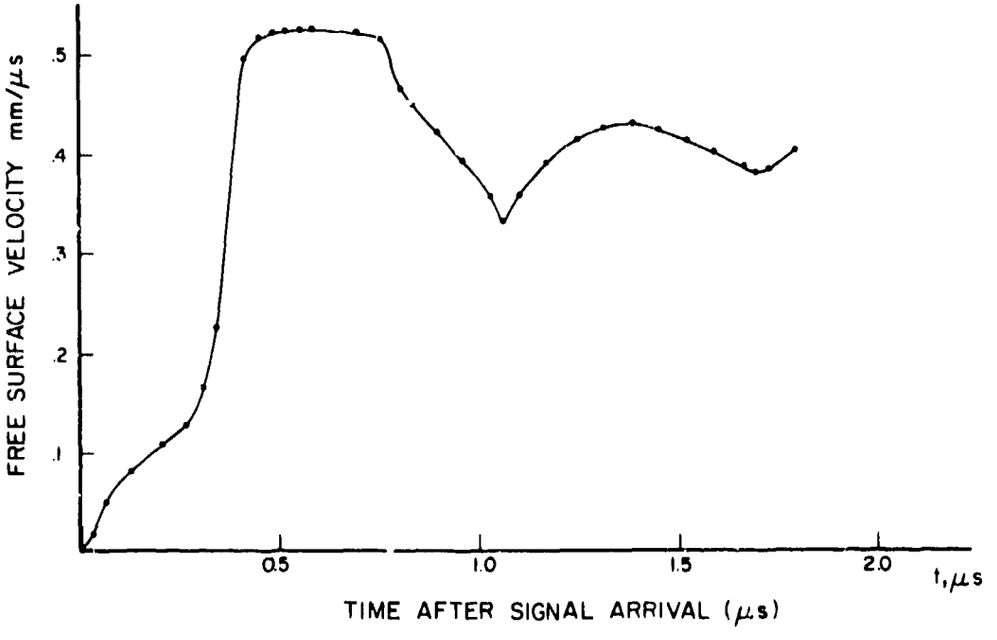

Figure 45. Free Surface Velocity from Shot 15.

TABLE 11

SUMMARY OF SPALL OBSERVATIONS FOR 4340 STEEL

Velocity m/s	Flyer Thickness m/s	Target Thickness m/s	Max. Compressive Stress (kbar)	Shot Number	Spall
233	1.0	5.0	44	113	No
320	1.0	5.0	61	56	Isolated voids
354	1.0	5.0	67	57	Connected voids
483	1.0	5.0	94	46	Complete
335	2.0	4.0	64	16	No
356	2.0	4.0	69	219	Complete
408	2.0	4.0	78	17	Complete
854	2.0	4.0	135	15	Complete

TABLE 12

FREE SURFACE VELOCITY PARAMETERS FOR 4340 STEEL

(Units = μs and mm/μs)

SHOT	15	17	219
t_p	.12 ± .01	.15 ± .02	0.22 ± .02
t_m	.52 ± .01	.33 ± .02	0.31 ± .02
t_{r1}	0.77 ± .02	.62 ± .01	0.64 ± .01
t_{r2}	1.14 ± .02	NR	0.73 ± .01
t_s	1.17 ± .03	.98 ± .02	1.09 ± .01
t_b	1.65 ± .03	1.29 ± .05	1.35 ± .05
v_E	50 ± 5	100 ± 10	120 ± 5
Δv_s	175 ± 10	220 ± 10	198 ± 5
Δv_f	50 ± 5	52 ± 10	176,106 ± 5
v_p	760 ± 10	420 ± 10	379 ± 5
v_{min}	575 ± 5	200 ± 10	180 ± 5

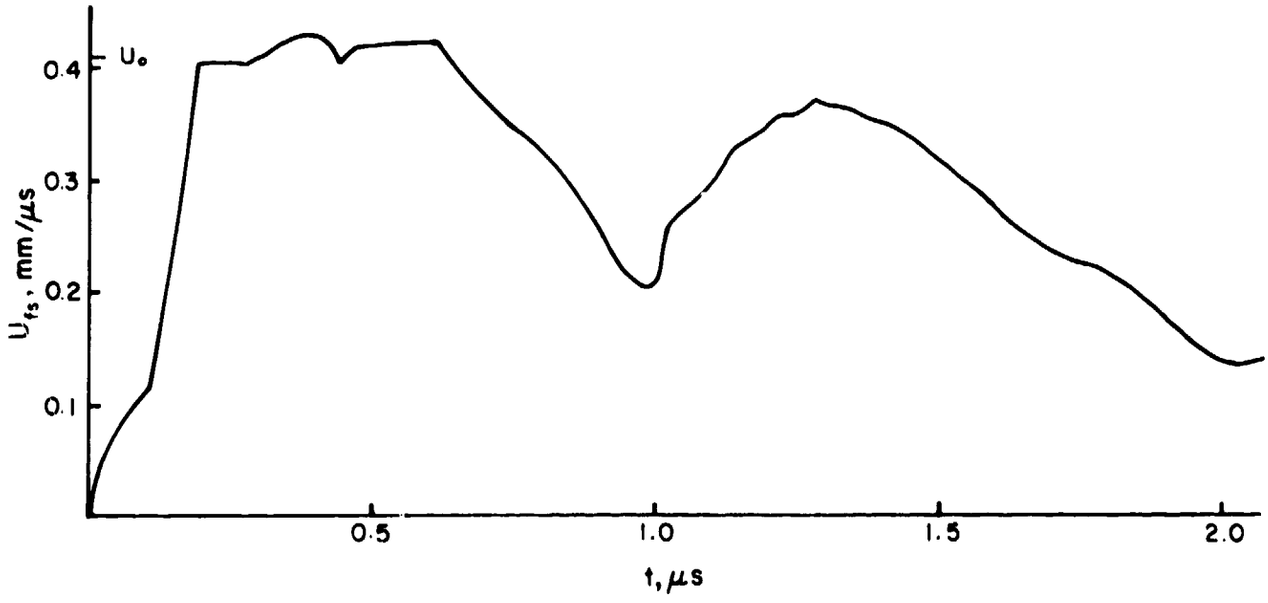

Figure 46. Free Surface Velocity from Shot 17.

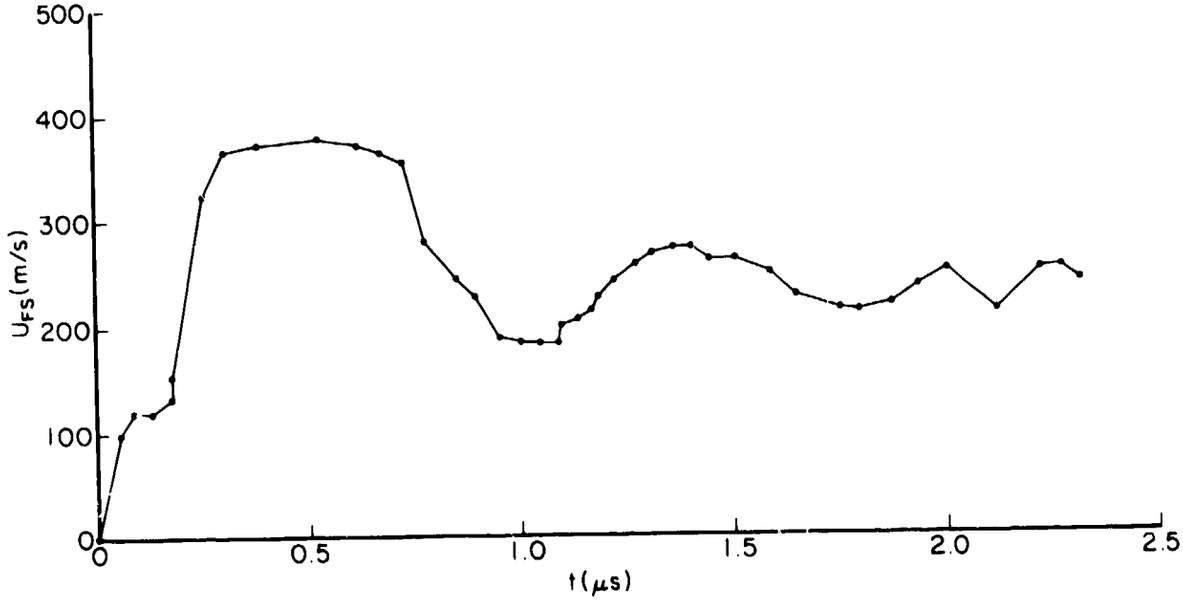

Figure 47. Free Surface Velocity from Shot 219.

It was immediately apparent that these [illegible] were inconsistent with a Tuler-Butcher approach because on the [illegible] lane σ_{min} = -58 kbar for case (a) but only -55 kbar [illegible] case (b). (The σ_{min} values in the thicker targets a[illegible] decreased by stress wave overtake.

The values of K_{2c} and σ_c used by MESCALL and PAPIRNO were widely inappropriate. For case (a) K_2 = 1600 kbar^2-μs, and for case (b) K_2 = 500 kbar^2-μs, when σ_o = 7 kbar. For this material, it was decided to abandon the K_λ, σ_o format. The threshold data are best described by a single stress criterion, namely σ_s = -56.5 kbar. SWAP runs for shot 219 also produced the best agreement with Figure 47 for a value of σ_s = ∿-60 kbar (although the uncertainty is about ±5 kbar). Thus, 1340 can be described by the relatively simple spall criterion of σ_s = -55 kbar.

SECTION VI

FRACTURE OF ARMOR PLATE

The rolled homogenous armor plate (RHA) tested in this program was RC 33. It was supplied by AFATL in the form of an 11 mm thick plate. The official specification for RHA are given in MIL-S-12560C.

1. PREVIOUS WORK ON RHA

The shock properties of RHA have been principally investigated by HAUVER. He found that C_L = 5.83 mm/μs. The HEL varied with hardness and sample thickness. His results imply that for the material and specimen thicknesses employed in this program, the HEL should be between 22 and 24 kbar. The Hugoniot for α-RHA was almost the same as α-iron, namely U = 4.51 + 1.43u (in mm/μs).

Fracture in RHA has been investigated by SHOCKEY et al. The NAG model was used to evaluate flat plate and penetrator impacts. The material was RC38, which is somewhat harder than that used here. They found Y_o = 11 kbar and ultimate strain of 0.2 (static test). The stress threshold for dynamic void formation was 11 kbar.

2. SPALL THRESHOLDS FOR RHA

Table 13 presents the spall threshold data for the RHA tested. In all cases, separation was essentially complete. However, in shot 268 the spall plate did not completely detach. All data were for 2 mm flyer plates. In shot 60 there was a discrepancy between the VISAR measured velocity and that measured by the time interval between crush pin closure. The VISAR data were used in the analysis.

TABLE 13

SPALL THRESHOLD DATA FOR RHA

u (m/s)	d (mm)	T (mm)	shot no	results
236	2.0	4.0	265	no spall
390	2.0	4.0	268	spall
771	2.0	4.0	21	spall
247	2.0	5.0	62	no spall
380	2.0	5.0	60	spall
449	2.0	5.0	123	spall
535	2.0	5.0	25	spall
622	2.0	5.0	23	spall

For 5 mm thick targets, the threshold velocity is between 247 and 390 m/s.

3. VISAR DATA FOR RHA

Good VISAR data were obtained in shots 25, 60, and 65. Limited VISAR data were obtained on shots 21 and 123. A sample velocity record, from shot 25, is shown in Figure 48. Table 14 presents the free surface velocity parameters determined from the VISAR data.

4. SPALL CRITERIA FOR RHA

The SWAP calculations were used to calculate the stress history on the incipient spall planes for the threshold conditions. SWAP calculations were carried out for RHA, using a material model consistent with the discussion in the preceeding

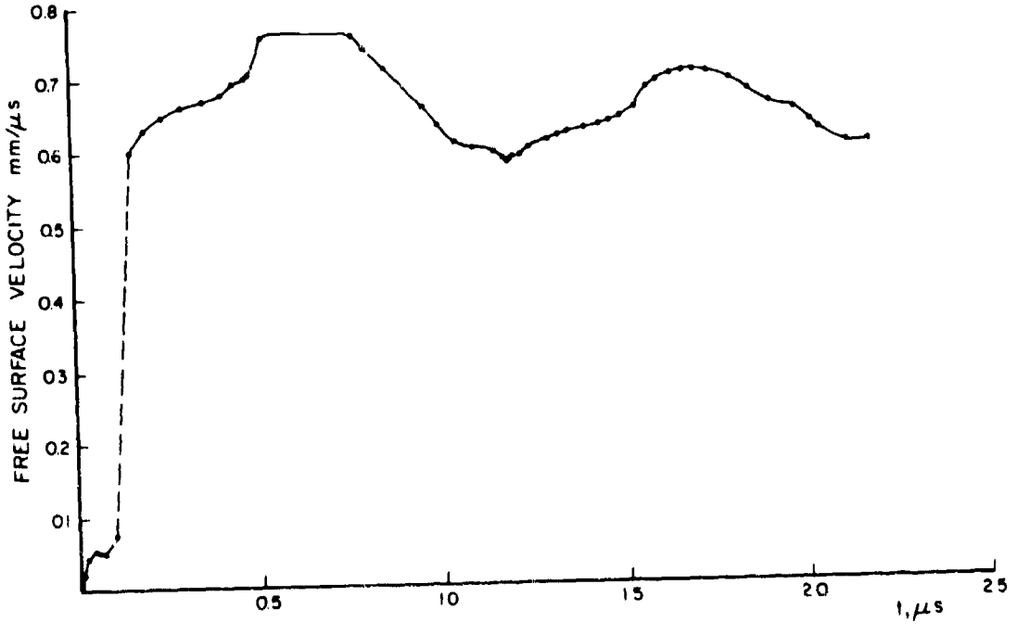

Figure 48. Free Surface Velocity of Measured in Shot 25.

TABLE 14

FREE SURFACE VELOCITY PARAMETERS FOR RHA

(units = s and m/s)

Shot No.	21	25	60	265
t_p	.10±.02	.35±.03	.21±.02	.22±.02
t_m	.20±.02	.42±.02	.82±.02	.34±.01
t_{r1}	.67±.05	.81±.02	.55±.02	.61±.01
t_{r2}	.81±.01		.92±.01	
t_s	.89±.02	1.07±.01	.01±.01	1.33±.05
t_b	NR	1.59±.05	NM	NA
V_E	75±5	60±20	60±5	84±10
V_p	630±10	535±10	380±10	234±10
V_{min}	395±10	338±10	170±10	34±10
ΔV_s	235±15	197±15	210±15	200±15
ΔV_f	NM	125±10	NM	NA

section. The threshold shots show that spall occurs at σ_s = -41 to -62 kbar for d = 2 mm. The spall stress calculated from equation (21) for three shots that spalled (21, 25, and 60) lie between 46 and 55 kbar, with a mean of 50 kbar. It appears σ_s does not change as σ_{max} varies from 73 to 150 kbar. SWAP calculations were not performed for these shots. However, in a series of SWAP calculations for spall in 4340 experiments with this geometry (d = 2 mm, T = 4 mm), $\sigma_s/(.5\rho C_L \Delta u_s)$ had a mean value of 1.74. Applying this result to shots 4, 25, and 60 gives σ_s = -87 kbar for a wide range of impact velocities.

Data are not available to evaluate the effect of stress history on spall for RHA. The SWAP calculations show the stress histories in 4 mm and 5 mm thick targets struck by 2 mm flyer plates are virtually identical.

Based on the data here, the recommended spall criteria is σ_s = -60 kbar. This value may slightly overestimate threshold conditions and slightly underestimate spall stress in overdriven material.

SECTION VII
RESULTS FOR NICKEL

The material tested was commercially pure nickel 200. No previous spall-related fracture data for this material were located. Hugoniot data are available from standard references, namely VanTHIEL et al., and MARSH. The low pressure Hugoniot can be represented as

$$U = 4.59 + 144u$$

in units of mm/μs. The density is $\sigma_o = 8.875$ g/cm^3. $C_L = 5.76$ mm/μs.

Spall threshold data for nickel are given in Table 15. Only one VISAR shot was carried out on a nickel target, the results of which are shown in Figure 49. Microstructures of voids in nickel is shown in Figure 50.

The VISAR data indicate considerable residual stress on the spall plane in shot 218. This is consistent with the observation that in 229, which differed in σ_{max} by only 1.5 kbar, separation on the spall plane was incomplete. The value of σ_s calculated from equation (21), using c_B as the spall shock speed, is 22 kbar. Using C_L gives 28 kbar, but because of the low strength of nickel c_B is probably more appropriate.

There is quite a wide range of values of impact velocities over which uncoalesced voids are observed. For 2 mm flyer plates, the range is about 15 kbar in σ_{max}.

There are not enough data available to adequately evaluate a time dependent spall threshold for nickel. The data available imply a threshold stress for void formation of 20±5 kbar. This applies for either threshold conditions or for overdriven spall conditions.

TABLE 15

SPALL THRESHOLD DATA FOR NICKEL

u (m/s)	d (mm)	T (mm)	Shot No	Results
55	1.0	5.0	267	No voids
205	1.0	5.0	119	Voids
307	1.0	5.0	120	Spall separation
00	2.0	5.0	214	Voids
122	2.0	5.0	115	No voids
167	2.0	5.0	266	Voids
229	2.0	5.0	116	Voids
236	2.0	5.0	218	Spall separation

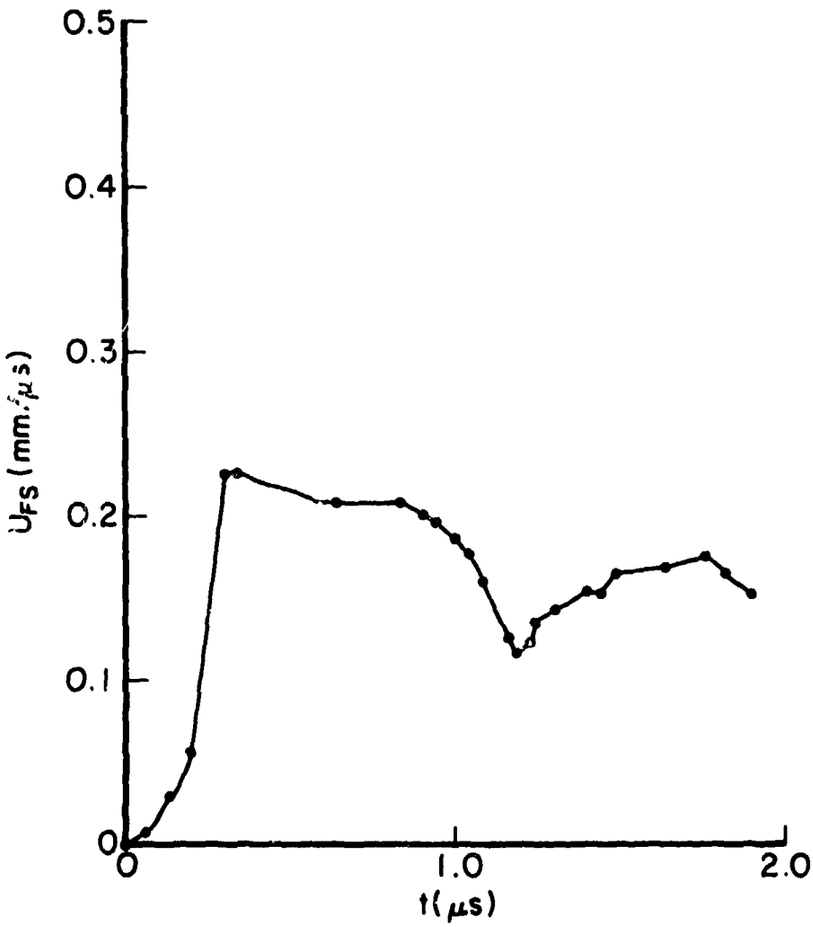

Figure 49. Free Surface Velocity from Shot 67.

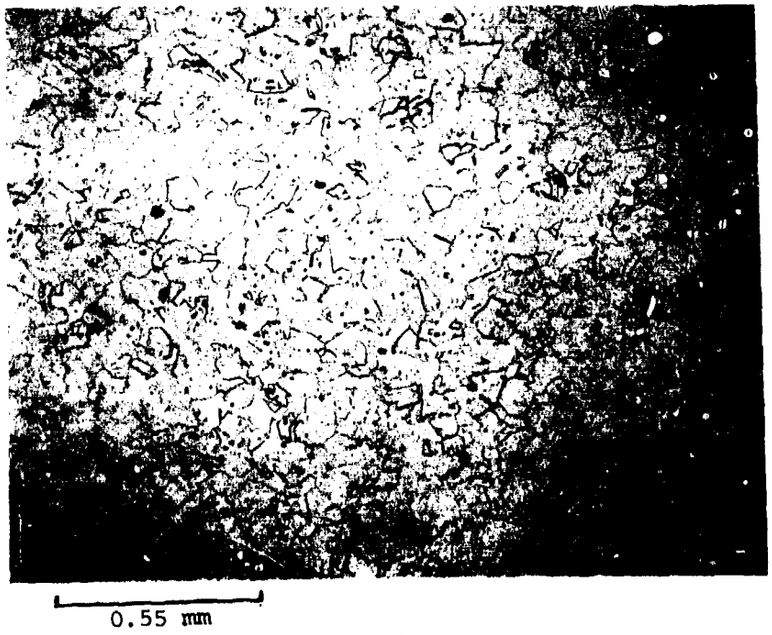

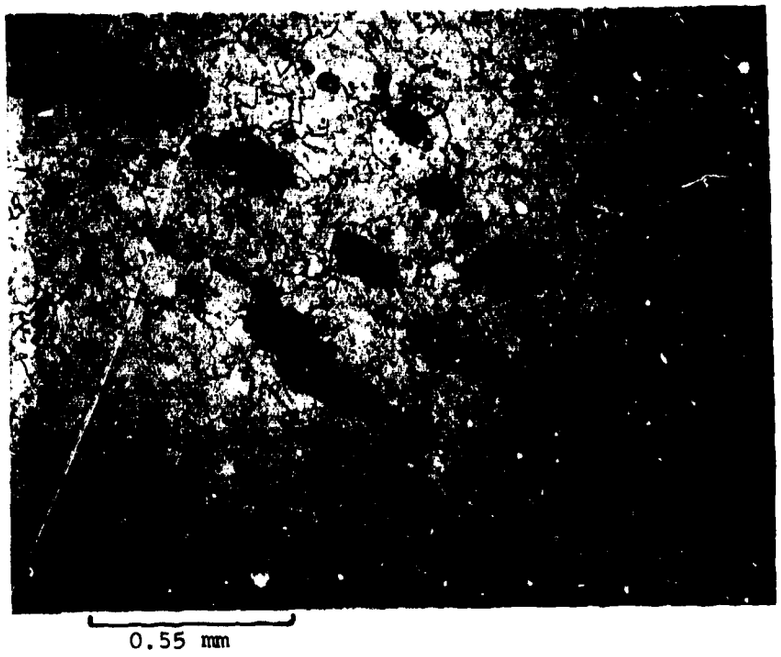

Figure 50. Microstructure of Nickel, Before Impact and in Void Region.

SECTION VIII
RESULTS FOR 1100 ALUMINUM

The aluminum that was the subject of this study was commercial grade 1100 alloy. Sample microstructure is shown in Figure 51.

1. PAST WORK

The compressive properties of aluminum are well known, and can be found, for example, in the compendium edited by MARSH. The Hugoniot for 1100 aluminum is $U = 5.38 + 1.34u$ (mm/μs).

The major past study of spall in 1100 series aluminum is that of BARBEE et al. They found that damage accumulated relatively slowly over a range of impact velocities. For $d = 5.8$ mm and $T = 15.8$ mm, incipient damage occurred for flyer plate velocities of about 89 m/s. For $d = 2.4$ mm and $T = 6.4$ mm, the critical velocity was about 126 m/s. The critical stress for void nucleation (in the NAG model) was 8 kbar. However, the time dependence of void growth and coalescence was quite significant.

2. PRESENT RESULTS

The spall threshold data are shown in Table 16. Complete separation was very hard to achieve in this material. Apparently the spall plate is launched with such a low velocity that shear failure along its edges (necessary for complete detachment) could not occur. Figure 52, for example, shows a cross section through the target from shot 51. Even though this shot was well above the spall threshold, a connected failure plane is absent. Spall plate thickness in aluminum was about 25 percent less than the flyer plate thicknesses. There was a relatively large velocity region in which voids formed but a connected

Figure 51. Sample Preshot Microstructure in Aluminum.

Figure 52. Microstructure on Spall Plane in Shot 51.

TABLE 16

SPALL THRESHOLD DATA FOR 1100 ALUMINUM

u (m/s)	d (mm)	T (mm)	shot no	results
300	1.0	4.0	272	connected voids
324	1.0	4.0	271	partial crack
365	1.0	4.0	270	connected voids
472	1.0	5.0	51	partial cracks
590	1.0	5.0	50	isolated voids
1556	1.0	5.0	52	isolated voids
409	2.0	5.0	47	isolated voids
570	2.0	5.0	49	spall separation
894	2.0	5.0	106	spall separation
1024	2.0	5.0	48	spall separation

spall fracture system was absent. Figure 53 shows an example. Spall occurred on three or four parallel planes, as in the model of DAVID et al.

SWAP calculations were carried out for the shots shown in Table 16. The results for σ_{min} are shown in Figure 54. The abscissa in Figure 54 is the length of time that the tensile stress exceeded $\sigma_{min}/2$.

The damage accumulation in aluminum was gradual. The spall criterion was taken as the occurrence of connected voids as shown in Figure 53.

The threshold for spall failure in aluminum was not well determined in these experiments. The impact velocity for causing connecting voids was lower than could practicably be obtained with the impact range employed. It appears that shots 47 and 272 are close to the threshold. Calculations of $K_{\lambda c}$ suggest that a value of $\lambda=1$ is much more appropriate than $\lambda=2$. However, even with $\lambda=1$, no time-dependent model produces less spread between K_λ values of shots 272 and 47 than exist just in σ_{min} values for these shots. If they are both near the threshold, then the best description is simply $\sigma_s < -20$ kbar. Evidently over the time scale of 0.3 to 0.7 μs, spall in this aluminum is not time dependent. At $\sigma_x = -20$ kbar, $\epsilon_p = -0.028$ for aluminum.

The VISAR data for aluminum shot 272 are given in Figure 55. The spall signal is $\Delta V_s = 76 \pm 5$ m/s. The residual stress on the spall plane is substantial consistent with the fact that the voids did not fully coalesce in this target. The value of σ_s from equation (21) is 5.5 or 7.4 kbar, depending on whether the bulk or elastic sound speed is employed. This is consistent with literature values of growth initiation stress.

Figure 53. Microstructure in Spall Plane in Shot 272.

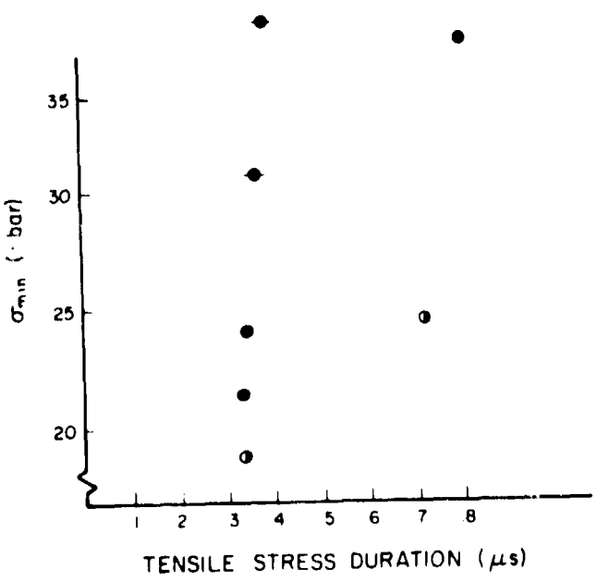

Figure 54. σ_{min} as a Function of Tensile Stress Duration for Aluminum Targets.

In summary, the data for 1100 aluminum are not definitive. The most prudent interpretation is that significant void growth begins in aluminum at values of σ_s = -7.4 kbar, and that over time scales of 0.3 to 0.7 μs, spall formation is not significantly time dependent.

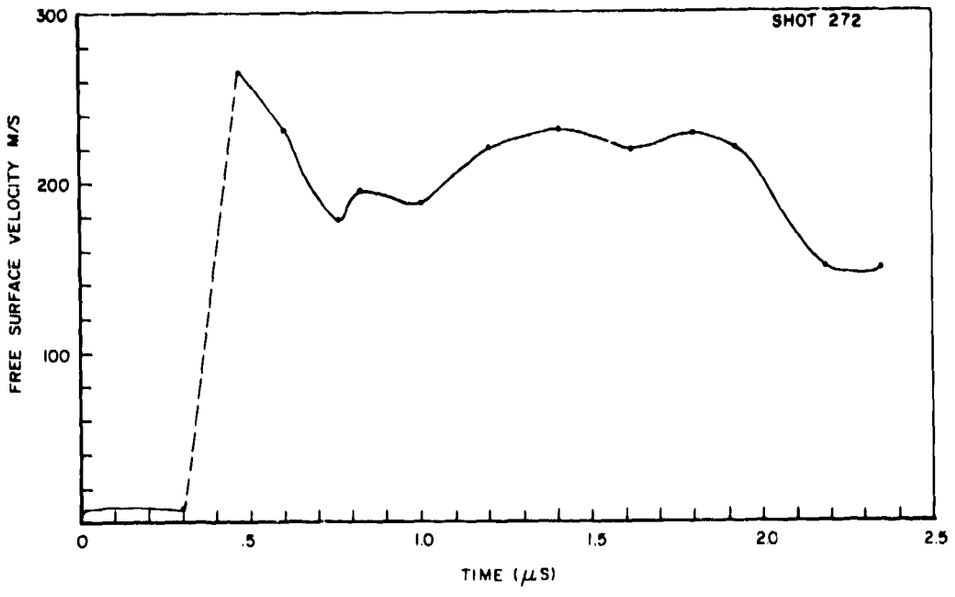

Figure 55. Free Surface Velocity from Shot 272.

APPENDIX A
EXPERIMENTAL TECHNIQUES

The program was carried out in the Impact Physics Facilities of the University of Dayton Research Institute. These facilities are described in detail by BLESS (1981).

1. LAUNCHER

All of the data shots in the program employed a 40 mm solid propellant gun. The launch tube was 4 m long, and is composed of two sections. The breech accepts conventional M40 brass cartridges. For the relatively low velocities required in this program an insert was designed so that less powder could be used without introducing irregularities in the loading curve.

The barrel was instrumented with a contact pin near the muzzle. A metallic ring on the front of the projectile closed the contact pin circuit, which generated a time of arrival signal.

The projectiles were made from PMMA. A description of a projectile is shown in Figure A-1, from which most details of its construction are evident. For shots higher than 100 m/s, the range was evacuated to 0.5 mm Hg. For lower velocity shots, the pressure was 5 mm Hg.

2. TARGET MOUNTING

The target was rigidly mounted 80 mm beyond the muzzle of the gun. Target orientation was adjustable. Prior to each shot perpendicularity to the trajectory was verified. Crush pins provided time of arrival data on the target. Initially, four crush pins were used to monitor tilt. Tilt was found to be always negligible, and in later data shots only one crush pin was used. At velocities above 200 m/s, the pin was crushed

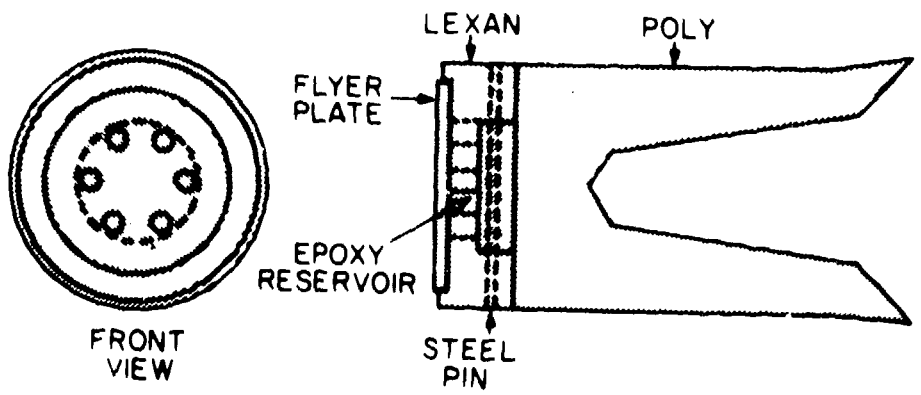

FLYER PLATE & SABOT

Figure A-1. Projectile Design.

by the PMMA sabot. At lower velocities, it was necessary to strike the pins with the flyer plates in order to be certain of prompt trigger signals.

Impact velocity was measured by several different techniques. For shots with shot number less than 212, impact velocity was measured from two transit times. The first was between a laser beam at the muzzle and a crush pin 12 mm from the impact surface. The second interval was the time between closure of crush pins 12 mm and 1 mm from the impact surface. The crush pins were manufactured by Dynasen Corporation. The crush pins were positioned so that they were struck by the PMMA ring around the flyer plate. The average of the velocities calculated by these techniques was employed, using inverse variance weighting. In 212 and later, a Cordin Model 241 70 mm streak camera was used to view the projectile prior to impact. The velocity was calculated from the photographic record. The flash lamp for the streak camera was initiated from a contact switch in the barrel that was closed by a conducting ring added to the projectile. The velocity was also calculated from the interval between closure of the pin and impact on a crush pin 1 mm from the target surface. High speed framing camera pictures were taken during test shots to verify the accuracy of the velocity measurement and the integrity of the launch package. For this purpose, a Beckman and Whitley Model 300 camera was employed. In most shots, two or three crush pins were also dedicated to monitoring impact planarity. Figure A-2 shows the mounting arrangement.

The VISAR was mounted next to the target tank on an air-cushioned table. The VISAR beam was directed by three adjustable mirrors. Initial alignment was done with the target removed. The VISAR laser was then adjusted to be coincident with the

reference laser that shown along the barrel axis. At ATA VISAR was employed. The VISAR oscilloscope was triggered by a crush pin 1 or 0.5 mm from the impact surface. Sometimes a delay generator was also used.

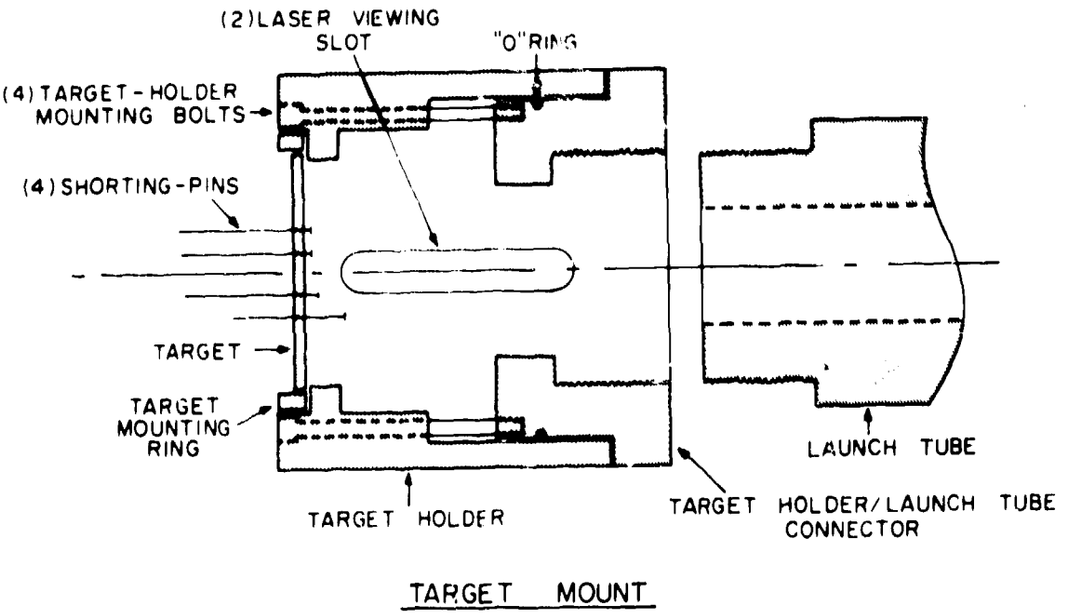

Figure A-2. Target Mounting Arrangement.

APPENDIX B
RELEASE WAVE SPEEDS IN FERRITE

Barker (1974) concluded that in a one-dimensional shock/release process in α Armco Iron, the release process was essentially hydrodynamic. By assuming that it is in fact hydrodynamic, one can calculate release wave speeds.

An excellent description of hydrostatic compression is given by:

$$P = 3K_s f\ (1-2\varepsilon)^{s/2}\ (1+2\varepsilon\xi) \qquad \text{(B-1)}$$

(see Birch) where K is the isontrop bulk modules; ε is a strain parameter, related to density by:

$$\rho = \rho_o\ (1-2\varepsilon)^{3/2} \qquad \text{(B-2)}$$

and ξ is a correction containing the third order elastic content

$$\xi = \frac{3}{4}\ (4 - \frac{\partial K}{\partial P}) \qquad \text{(B-3)}$$

also

$$K = K_s\ (1-2\varepsilon)^{s/2}\ [1-7\varepsilon + 2\xi\varepsilon(2+9\varepsilon)] \qquad \text{(B-4)}$$

where K_s is here the initial bulk modules at zero pressure. The bulk wave speed may be computed from:

$$C_B = \sqrt{K/\rho} \qquad \text{(B-5)}$$

Values for these parameters are K_s = 1664 kbar, $\frac{\partial k}{\partial p}$ = 5.29 (GUINAN and BESHERS). Hence ξ = -0.9675.

C_B as a function of P can now be computed. Representative values are:

ε	ρ (g/cm^3)	P kbar	C_B km/s
0.0	7.85	0	4.604
-0.01	8.0867	53.5	4.726
-0.02	8.3257	114.4	4.856

When C_B is plotted as P between 0 and 130 kbar, it is seen that it is very nearly linear. The least-square-best-fit-straight line is

$$C_B = 4.6068 + 0.00218P \tag{B-6}$$

This misses the calculated points by only ~2 m/s at both ends of the pressure range.

If the shock and release process takes place wholly in α-iron, pressure profiles may be calculated from the method of characteristics. The C_+ characteristics are

$$x = u + C(u)t \tag{B-7}$$

Before the release waves intercept, the C_- invariant is

$$J_- = u_o \tag{B-8}$$

Hence, anywhere, and in particular along C_+

$$\int \frac{dP}{\rho c} = u - u_o \tag{B-9}$$

To a very good approximation

$$\int \frac{dP}{\rho c} = -1.25\text{x}10^{-19}\ P^2 + 2.758 \text{ x } 10^{-7}\ P \tag{B-10}$$

when cgs units are used. The relationship between $\Delta u = u-u_o$ and P is then

$$P = -1103.2 + \sqrt{1.217\text{x}10^6 - 8\text{x}10^6 \Delta u} \tag{B-11}$$

where Δu is in km/s and P is in kbar (note $\Delta u<o$).

APPENDIX C

REDUCTION OF VISAR DATA

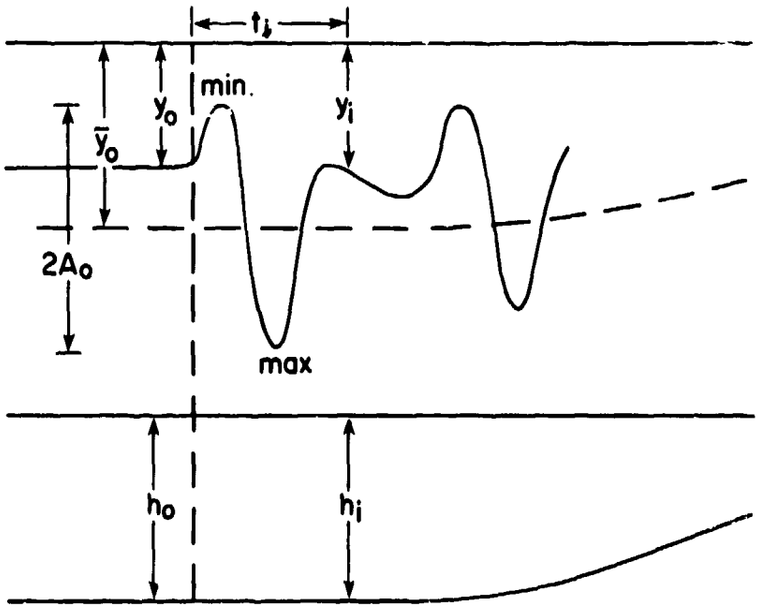

Figure C-1. Sample Visar Data Trace

Referring to Figure C1:

A = Fringe amplitude (contrast)

A_o = Initial value of firing amplitude

$\bar{y}$ = Mean value of data signal

$\bar{y}_o$ = Initial values of $\bar{y}$

h = Beam intensity

h_o = Initial value of h

i = Subscript denoting measurement time

The fringe amplitude, f, is given by:

$$f = \frac{y - \bar{y}}{A} \qquad \text{(C1)}$$

This quantity varies between -1 and +1. The phase angle, Θ is given by:

$$\Theta = \text{arc sin } f \tag{C2}$$

The initial value of Θ is denoted Θ_o
At a measurement time, t_i

$$\Theta_i = \text{arc sin } \frac{y_i - \bar{y}_i}{A_i} \tag{C3}$$

The current values of $\bar{y}_i$ and A_i are calculated from the beam intensity:

$$\bar{y}_i = \bar{y}_o \ (h_i/h_o) \tag{C4}$$

$$A_i = A_o \ (h_i/h_o) \tag{C5}$$

The velocity at time t_i is computed from.

$$V_i = KF$$

Here K is the fringe constant, and F is the phase shift, defined by:

$$F = \frac{\Theta - \Theta_o}{2\ \pi} \tag{C6}$$

or

$$F = \frac{\Theta - \Theta_o}{360} \tag{C7}$$

If Θ is expressed in degrees. In hand-calculator operations, using Θ in degrees is somewhat simpler and the form is used in this work. In BARKER (1970), it is explained how K is calculated from the VISAR delay and laser wavelength.

The most difficult stage of the analysis is to determine A_o and $\bar{y}_o$. When the peaks labelled min and max in Figure C1 are discernable, then:

$$A_o = \frac{y_{max} - y_{min}}{2}$$

$$\bar{y}_o = \frac{y_{max} + y_{min}}{2}$$

Preshot photos of fringe contrast were taken to help determine y_{max} and y_{min}. However, it became clear that during a shot the value of A_o could be more than in the preshot calibration. This is probably due to improved gain of the PM tubes on low duty cycles.

Unfortunately, much of the time the peaks labelled min and max at the beginning of the trace are not present, either because the shock rise time is too fast for the VISAR to follow, or else because the maximum velocity corresponds to less than one full fringe. Usually late peaks are present. However, in this case, interpretation must be injected to distinguish reversals from peaks. When an unfamiliar material is being tested, sometimes several records must be examined before reversals and peaks can be definitively distinguished. Trial values of A_o and $\bar{y}_o$ must be employed in order to force $f = \pm 1$ at the designated points.

In most experiments, the peak free surface velocity is known from measurements of the impact velocity. This also provides a check on A_o and $\bar{y}_o$. In some worst cases, it is the only check on these values; when that happens, the VISAR record loses value as a quantitative measure of velocity, although it still yields accurate data for arrival times.

It is possible for fringe amplitude to change during an experiment independent of changes in beam intensity. This is most likely to occur when severe target deformation is produced by the shock. It is seldom a concern in the present investigation. Changes in fringe contrast can be accounted for by introduction of a contrast parameter, C.

Initially,

$$C = \bar{y}_o - A_o$$

At later times,

$$A_i = \bar{y}_i - C_i$$

C_i may be still defined in terms of C_o.

$$C_i = \frac{h_i}{h_o} C_o$$

However, C_o is considered a slowly-varying adjustable parameter. Introduction of variable C_o can introduce considerable uncertainty in calculated values of u_i.

The VISAR records two signals in quadrative; that is, separated in phase by 90°. This aids in the distinction of fringe extreme and velocity reversals. Preshot calibration pictures were often very useful in interpreting VISAR records. The preshot beam intensity, h_c, was usually slightly less than h. The value of $\bar{y}_o$ could be taken as equal to $\bar{y}_c h_o/h_c$. Often $A_o = A_c h_o/h_c$, also, although sometimes $A_o > A_c h_o/h_c$ for reasons not well understood. Figure C-2 shows a sample set of data.

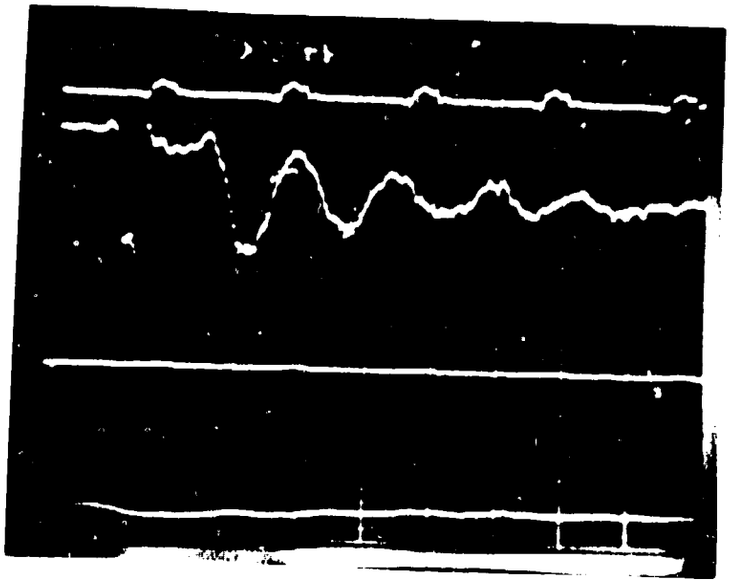

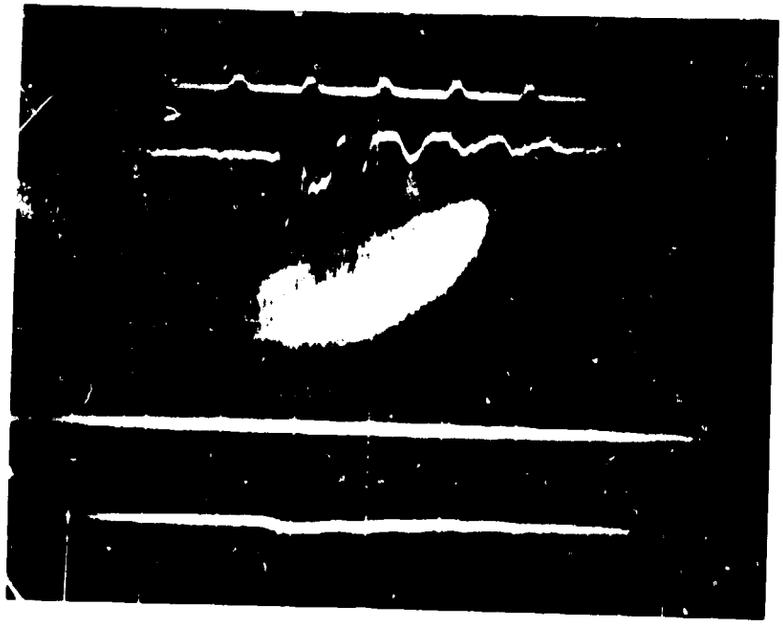

Figure C-2. Two Quadrature Channels from Shot 219. (Timing marks are 1 MHz.)

REFERENCES

1. J.R. Asay and J. Lipkin, "A Self-Coinsistent Technique for Estimating the Dynamic Yield Strength of a Shock-Loaded Material", J. Appl. Phys. 49, 4242-4247, 1978.

2. T. Barbee, L. Seaman, R.C. Crewdson, "Dynamic Fracture Criteria of Homogeneous Materials", AD878449, November 1970.

3. L.M. Barker and R.E. Hollenbach, "Laser Interferometer for Measuring High Velocities of Any Reflecting Surface", J. Appl. Phys. 43, 4669-4674, 1972.

4. L.M. Barker and E.G. Young, "SWAP-9: An Improved Stress Wave Analyzing Program", SLA-74-0009, June 1974.

5. D.P. Bauer and S.J. Bless, "Strain Rate Effects on Ultimate Strain of Copper", AFML-TR-79-4021, November 1978.

6. L.D. Bertholf, L.D. Buxton, B.J. Thorne, R.K. Byers, A.L. Stevens, and S.L. Thompson, "Damage in Steel Plates from Hypervelocity Impact II. Numerical Results and Spall Measurement", J. Appl. Phys. 96, 3776-3783, 1975.

7. S.J. Bless, J.P. Barber, and D.A. Matuska, "Impact Induced Tensile Failures in Steel", High Pressure Science and Technology, ed. B. Vodar and Ph. Marteau, 1029-1031, 1980.

8. B.M. Butcher and J.R. Canon, "Influence of Work-Hardening on the Dynamic Stress-Strain Curves of 4340 Steel", AIAA Journal, 2174-2179, December 1969.

9. D.R. Christman and W.M. Isbell, "Measurements of Dynamic Properties of Materials, Volume V. OFHC Copper", AD728 846, July 1971.

10. T.B. Cox and J.R. Low, "An Investigation of the Plastic Fracture of AISI 4340 and 18 Nickel-200 Grade Managing Steels", Met. Trans. 5, 1457-1470, 1974.

11. F. David, J. Varellies, F. Prouteau, and J. Legrand, CEA-R-4414 (France) (available NTIS), 1973.

12. G.R. Fowles, "Shock Wave Compression of Hardened and Annealed 2024 Aluminum", J. Appl. Phys. 32, 1975-1987, 1961.

13. R.E. Franz and J. L. Robitaille, "The Hugoniot of 4340 Steel, RC54-55", AD A076968, September 1979.

14. W.H. Gust, "Hugoniot Elastic Limits and Compression Parameters for Brittle Materials", High Pressure Science and Technology, ed. B. Vodar and Ph. Marteau, Pergamon Press, 1009-1013, 1980. (Also UCRL-83020, 1979).

15. G.E. Hauver, "The Alpha-Phase Hugoniot of Rolbd Homogeneous Armor", ADB012871, August 1976.

16. A.C. MacKenzie, J.W. Hancock, and D.K. Brown, "On the Influence of State of Stress on Ductile Failure Initiation in High Strength Stuls", Eng. Fracture Mech. 9, 167-188, 1977.

17. S.P. Marsh, ed. LASL Shock Hugoniot Data, U.C. Press, 1980.

18. A.R. McMillan, W.M. Isbell, and A.H. Jones, "High Pressure Shock Wave Attenuation", AD 733 490, June 1971.

19. R.G. McQueen, S.P. Marsh, J.W. Taylor, J.N. Fritz, and W.J. Carter, "The Equation of State of Solids from Shock Wave Studies", in High Velocity Impact Phenomena, R. Kinslow, ed., 1970.

20. G.L. Moss, "Critical Growth Stress for Spallation", AD045413, September 1977.

21. G.L. Moss, private communication cited by Walter, 1979.

22. National Materials Advisory Board, "Material Response to Ultra-High Loading Rates", PB80-15352, 1980.

23. J. Osborn, private communication, 1978.

24. R.P. Papirno, J.F. Mescall, and A.M. Hanson, "Beyond the Taylor Test to Fracture", in Proceedings of Army Symposium on Solid Mechanics, AD-A090684, September 1980.

25. M.W. Perra, "Mechanisms of Ductile Fracture", LBL-4901, 1976.

26. A.M. Rajendron and I.M. Fyfe, "A Void Growth Criterion Applied to Dynamically and Statically Loaded Thin Rings", Univ. of Wash. Rept. 80-10, submitted to Army Research Office, June 1980. (See also J. Mech. Phys. Solids, Vol. 28).

27. L. Seaman, T.W. Barbee, and D.R. Curran, AFWL-TR-71-156, February 1972.

28. Shockey, D.A., et al., "A Computational Model for Fragmentation of Armor Under Ballistic Impact", ADB004672, April 1975.

29. J.W. Taylor, "Stress Wave Profiles in Several Metals", Dislocation Dynamics, McGraw Hill, 573-589, 1968.

30. F.R. Tuler and B.M. Butcher, "A Criterion for the Time Dependence of Dynamic Fracture", Int. J. Fracture Mech., 4, 431-437, 1968.

31. J. Zukas "Impact Dynamics", Emerging Technologies in Aerospace Structures, Structural Dynamics and Materials, ed. J.R. Vinson, ASME, 1980.

A-1. S.J. Bless "Impact Facilities at the University of Dayton Research Institute, UDR-TR-80-04, May 1981.

B-1. L.M. Barker and R.E. Hollenbach, "Shock Wave Study of the α-ε Phase Transition in Iron", J. Appl. Phys. 45, 4872-7887, 1974.

B-2. F. Birch, Elasticity and Constitution of the Earth's Interior, J. Geophys. Res., 57, 227-286, 1952.

B-3. M. Guinan and D.N. Beshers, "Pressure Derivations of the Elastic Constants of α-Iron to 10 kbars", J. Phys. Chem. Solids, 29, 541-548, 1968.

C-1. L.M. Barker and R.E. Hollenbach, J. Appl. Phys., 41, 4208, 1970.

☆U.S.Government Printing Office: 1982 — 559-006/5057